ENTANGLED QUANTUM DYNAMICS VIA MACROSCOPIC QUANTUM TUNNELING OF BRIGHT SOLITONS IN BOSE-EINSTEIN CONDENSATES

by

Joseph A. Glick III

A thesis submitted to the Faculty and the Board of Trustees of the Colorado School of Mines in partial fulfillment of the requirements for the degree of Master of Science (Applied Physics).

Golden, Colorado

Date _____

Signed: _____
Joseph A. Glick III

Approved: _____
Dr. Lincoln Carr
Associate Professor of Physics
Thesis Advisor

Golden, Colorado

Date _____

_____
Dr. Thomas Furtak
Professor and Head,
Department of Physics

ABSTRACT

We study the quantum tunneling dynamics of many-body entangled solitons composed of ultracold bosonic gases in one-dimensional optical lattices. A bright soliton, confined by a potential barrier, is allowed to tunnel out of confinement by reducing the barrier width and for varying strengths of attractive particle-particle interactions. Simulation of the Bose Hubbard Hamiltonian is performed with time-evolving block decimation. We find the characteristic $1/e$ time for the escape of the soliton, substantially different from the mean field prediction, and address how many-body effects like quantum fluctuations, entanglement, and nonlocal correlations affect macroscopic quantum tunneling; number fluctuations and second order correlations are suggested as experimental signatures. We find that while the escape time scales exponentially in the interactions, the time at which both the von Neumann entanglement entropy and the slope of number fluctuations is maximized scale only linearly.

TABLE OF CONTENTS

LIST OF FIGURES

ACKNOWLEDGMENTS

I owe the deepest gratitude to my advisor Lincoln Carr, not only for his assistance and support throughout this project, but for helping me to become a better scientist. I sense that in the years to come I will look back on my experience here only to perceive more clearly the significance of the invaluable opportunity he gave me to be a part of his research group. His enthusiasm, insight, and patient guidance have contributed greatly to my educational development.

I thank the faculty of the Physics Department at the Colorado School of Mines for their tireless efforts and dedication to students like myself. In particular, I want to thank Professors David Wood, Mark Lusk, and Alex Flournoy for their excellence as teachers, who taught some of the most challenging and eye-opening courses I took here at Mines. I am grateful to both David Wood and Mark Lusk for serving on my thesis defense committee and for providing many valuable discussions and comments on this work. In addition, I thank Michael Wall, a Ph.D. student in our research group, for his valuable insight and helpful assistance with the time-evolving block decimation code.

Most importantly, I am grateful for and would not be here without my family. My parents have continually encouraged and supported me throughout all the trials and travails I have had here at Mines. I would not be where I am today if not for their sacrifice and hard work. Finally, I thank my fiancée Jen for keeping me happy and sane, for enduring the stresses associated with graduate school, and for her help planning our wedding in the midst of me writing my thesis. I love her dearly.

I do not know what I may appear to the world, but to myself I seem to have been only like a boy playing on the sea-shore, and diverting myself in now and then finding a smoother pebble or a prettier shell than ordinary, whilst the great ocean of truth lay all undiscovered before me.

-Isaac Newton

Chapter 1

HISTORY, FORMALISM, AND FUNDAMENTAL CONCEPTS

In this chapter, we introduce macroscopic quantum tunneling in the context of Bose-Einstein condensates (BECs), while also providing a brief historical overview. We will develop the basic formalism, and discuss the foundational concepts of BEC, both of which are necessary tools for understanding the quantum properties of our system.

1.1 Historical Perspective

In 1928 quantum tunneling was first proposed by George Gamow, and independently by Ronald Gurney and Edward Condon, as the mechanism responsible for α decay, and was recognized thereafter by Max Born as a general feature of quantum mechanics.[1] Its success as a theory may be considered one of the triumphs of quantum mechanics, explaining a wide range of physical phenomena in contexts as diverse as biophysics [2], astrophysics, and the tunneling between vacuum states in quantum cosmology and chromodynamics [3, 4, 5]. Furthermore, the theory has been instrumental in the development of technological innovations such as the scanning tunneling microscope (STM), tunneling diodes, Josephson junctions, and many more. As such, tunneling remains a vibrant and illuminative area of research, especially with regard to many-body systems, where one can attempt to answer the fundamental question of how microscopic quantum behavior begets macroscopic phenomena.

Macroscopic quantum tunneling (MQT) is the aggregate tunneling behavior of a many-body wavefunction, where we refer to "macroscopic" throughout this thesis as a system with a large number of dynamical microscopic degrees of freedom. The

[1] An interesting historical account is given by L. Rosenfeld [1].

remarkable manifestation of distinct nonclassical behavior in MQT is particularly befitting for Bose-Einstein condensates, where quantum phenomena are regularly observed on macroscopic length scales. For example, predictions for MQT in BECs range from cold atom Josephson rings [6] to collapsing BECs [7], and MQT has been observed in double well potentials [8, 9, 10]. MQT has mainly been treated under semiclassical approximations such as JWKB and instanton methods, while more recently significant progress has been made towards a more general many-body picture via multi-configurational Hartree-Fock theory [11]. In this thesis, we present the first fully many-body entangled dynamical study of the quantum tunneling escape problem.

The concept of Bose-Einstein condensation was first motivated by Indian physicist Satyendra Nath Bose in a 1924 seminal paper on the quantum statistical nature of light, where he derived Planck's distribution law from first principles. On this basis, in 1925, Albert Einstein, who had translated Bose's paper into German and assisted in its publishing, extended the theory to include massive bosons. Einstein predicted that noninteracting bosons will undergo a phase transition when cooled below a critical temperature, in which the bosons macroscopically occupy the lowest-lying single particle quantum state. The effect occurs at low temperatures when the de Broglie wavelength of the particles, which scales inversely with the square root of the temperature, becomes comparable to the mean separation of the particles. At the critical temperature, the individual particle wavefunctions become sufficiently overlapped with one another to the point where the system macroscopically occupies a single state.

Today this state of matter is called Bose-Einstein condensation, and in 1995 it was first achieved experimentally in dilute atomic gases by Eric Cornell, Carl Wieman, Wolfgang Ketterle, and Randy Hulet. The first set of experiments was performed with ultracold gases of rubidium [12], sodium [13], and lithium [14, 15]. These achievements were made possible by several pioneering experimental innovations. Magneto-optical traps, a technique developed in the 1980's, gave experimentalists the ability to con-

fine neutral atoms with laser light [16, 17, 18]. Then, using a combination of laser and evaporative cooling methods, dilute alkali gases were finally brought to the temperature regimes necessary for achieving BEC. Bose-Einstein condensation in alkali gases has since provided researchers with a new theoretical and experimental setting in which to explore quantum mechanical phenomena over macroscopic length scales.

We will begin by explaining BECs in the context of the one-body density matrix, which is qualitatively different for a BEC in comparison to the density matrix for an ordinary state of matter. This will allow us to develop some formalism and to introduce the essential concepts of off-diagonal long-range order and the order parameter.

1.2 The One-Body Density Matrix and Long-Range Order

Consider an arbitrary many-body system, which is prepared in a pure state, that is, it can be completely described by a single N-body wavefunction $\Psi_N(\boldsymbol{r}_1, \boldsymbol{r}_2, ..., \boldsymbol{r}_N)$. The density matrix for such a system[2] is defined, by the rules of quantum mechanics, to be

$$\rho = \Psi_N^*(\boldsymbol{r}_1, \boldsymbol{r}_2, ..., \boldsymbol{r}_N)\ \Psi_N(\boldsymbol{r}_1, \boldsymbol{r}_2, ..., \boldsymbol{r}_N). \tag{1.1}$$

If we take $\Psi_N(\boldsymbol{r}_1, \boldsymbol{r}_2, ..., \boldsymbol{r}_N)$ to be normalized to 1, then we can define the one-body density matrix by integrating out the $N-1$ coordinates $(\boldsymbol{r}_2, \boldsymbol{r}_3, ..., \boldsymbol{r}_N)$, that is

$$\rho^{(1)}(\boldsymbol{r}, \boldsymbol{r}') = N \int d\boldsymbol{r}_2\ ...\ d\boldsymbol{r}_N\ \Psi_N^*(\boldsymbol{r}, \boldsymbol{r}_2, ..., \boldsymbol{r}_N)\Psi_N(\boldsymbol{r}', \boldsymbol{r}_2, ..., \boldsymbol{r}_N). \tag{1.2}$$

Equation (1.2), can be more usefully expressed using field operators.[3] Consider the field operators $\hat{\Psi}^\dagger(\boldsymbol{r})$ and $\hat{\Psi}(\boldsymbol{r}')$, which respectively create a particle at $\boldsymbol{r}$ and

[2]Note that we are neglecting additional internal degrees of freedom, such as hyperfine degrees of freedom which can be added to the arguments of the wavefunction if necessary. Also, a dependence on time is necessary for systems out of equilibrium.

[3]See Chapter 1.4 for further elaboration.

destroy a particle at $\boldsymbol{r}'$. We define the one-body density matrix to be [19],

$$\rho^{(1)}(\boldsymbol{r},\boldsymbol{r}') = \big\langle m, N\big|\hat{\Psi}^\dagger(\boldsymbol{r})\hat{\Psi}(\boldsymbol{r}')\big|m, N\big\rangle = \big\langle\hat{\Psi}^\dagger(\boldsymbol{r})\hat{\Psi}(\boldsymbol{r}')\big\rangle. \tag{1.3}$$

The one-body density matrix can be used to describe any general system, which in our case is a system of N identical bosons. For now, let the average in (1.3) be taken over an arbitrary state $\big|m, N\big\rangle$, where m is a general state label, often denoting the ground state, and N is the number of particles.

Equation (1.3) is a Hermitian quantity and harbors critical information about physical observables for our system. Namely, if we look at the diagonal elements by taking $\boldsymbol{r} = \boldsymbol{r}'$, we can define the total number of particles N to be,

$$N = \int d\boldsymbol{r}\ \rho^{(1)}(\boldsymbol{r},\boldsymbol{r}) = \int d\boldsymbol{r}\ \big\langle\hat{\Psi}^\dagger(\boldsymbol{r})\hat{\Psi}(\boldsymbol{r})\big\rangle. \tag{1.4}$$

Since the one-body density matrix (1.3) is a Hermitian matrix, it can be diagonalized to take the form

$$\rho^{(1)}(\boldsymbol{r},\boldsymbol{r}') = \sum_i \rho_i\ \chi_i^*(\boldsymbol{r})\chi_i(\boldsymbol{r}'), \tag{1.5}$$

where χ_i are eigenfunctions of $\rho^{(1)}$ and ρ_i are eigenvalues of $\rho^{(1)}$ in the sense that they obey the relationship,

$$\int d\boldsymbol{r}'\ \rho^{(1)}(\boldsymbol{r},\boldsymbol{r}')\ \chi_i(\boldsymbol{r}') = \rho_i\ \chi_i(\boldsymbol{r}). \tag{1.6}$$

The functions χ_i correspond to single-particle states and form a complete orthogonal set, that is,

$$\int d\boldsymbol{r}\ \chi_i^*(\boldsymbol{r})\chi_j(\boldsymbol{r}) = \delta_{ij}. \tag{1.7}$$

The eigenvalues ρ_i correspond to single-particle occupation numbers and are normalized to the number of particles,

$$\sum_i \rho_i = N. \tag{1.8}$$

Moving forward, the one-body density matrix will prove to be a very useful concept, and will play a central part in the description of Bose-Einstein condensation.

1.2.1 Bose-Einstein Condensation and Off-Diagonal Long Range Order

Bose-Einstein condensation occurs when a many-body system exhibits a macroscopic occupation of a single particle state. Looking at Eq. (1.5), this means that one of the eigenvalues of the one-body density matrix will dominate in comparison to the others, that is there will be an eigenvalue $\rho_{i=0} = N_0$ which is on the order of the number of particles N, while all the other eigenvalues are of order 1. The N_0 particles, each occupying the single particle state $\chi_0(\boldsymbol{r})$, are said to be *Bose-condensed*. In an ideal Bose gas at temperature $T = 0$ all the particles are Bose-condensed; for a non-ideal system only a number N_0 of the particles will be Bose-condensed, as expressed by the condensate fraction

$$N_0/N \leq 1. \tag{1.9}$$

One may already anticipate that the function $\chi_0(\boldsymbol{r})$ is closely related to the wave-function of the condensate.

The macroscopic occupation of a single particle state implies that a Bose-Einstein condensate has a one-body density matrix whose dominant eigenvalue remains finite and non-zero in the limit where $\tilde{\boldsymbol{r}} = (\boldsymbol{r} - \boldsymbol{r}') \to \infty$. This property is better understood by looking at the momentum representation of the one-body density matrix, as derived in reference [20]. First write the field operators in the momentum representation using the Fourier transform

$$\hat{\Psi}(\boldsymbol{p}) = (2\pi\hbar)^{-3/2} \int d\tilde{\boldsymbol{r}} \ \exp(i\boldsymbol{p}\cdot\tilde{\boldsymbol{r}}/\hbar)\hat{\Psi}(\tilde{\boldsymbol{r}}), \tag{1.10}$$

and take the momentum distribution to be defined as

$$\rho^{(1)}(\boldsymbol{p}) = \left\langle \hat{\Psi}^\dagger(\boldsymbol{p})\hat{\Psi}(\boldsymbol{p}) \right\rangle. \tag{1.11}$$

In the momentum distribution of (1.11), the N_0 particles all occupying the single particle state having momentum $\boldsymbol{p}'$ will take the form of a delta function, while the other $N - N_0$ particles will take some other functional form $f(\boldsymbol{p})$:

$$\rho^{(1)}(\boldsymbol{p}) = N_0 \ \delta(\boldsymbol{p} - \boldsymbol{p}') + f(\boldsymbol{p}) \tag{1.12}$$

The Fourier transform of the momentum distribution (1.11) is,

$$\rho^{(1)}(\tilde{\boldsymbol{r}}) = \frac{1}{V} \int d\boldsymbol{p} \ \exp(-i\boldsymbol{p} \cdot \tilde{\boldsymbol{r}}/\hbar)\rho^{(1)}(\boldsymbol{p}). \tag{1.13}$$

Inserting Eq. (1.12) for $\rho^{(1)}(\boldsymbol{p})$ and taking the limit as $\tilde{\boldsymbol{r}} \to \infty$, we find that at large distances the singular delta function term will collapse the integral to a nonzero scalar value

$$\rho^{(1)}(\tilde{\boldsymbol{r}} \to \infty) = \frac{N_0}{V}. \tag{1.14}$$

This property is known as off-diagonal long range order.

Off-diagonal long range order was first mentioned by Landau and Lifshitz in 1951 [19] and then later by Penrose and Onsager in 1956. Off-diagonal long-range order is a distinguishing symmetry property of Bose-Einstein condensates. Ordinary liquids do not possess this property; they always have $\rho^{(1)}(\tilde{\boldsymbol{r}} \to \infty) = 0$. Off-diagonal long range order becomes very evident in the experimental realization of BECs: during the cooling process when $T > T_c$, $\rho^{(1)}(\tilde{\boldsymbol{r}} \to \infty) = 0$, then after the phase transition, when $T < T_c$, $\rho^{(1)}(\tilde{\boldsymbol{r}} \to \infty) = N_0/V$.

We should attempt to make sense of this in a qualitative way. Why does off-diagonal long range order appear when we make the phase transition to Bose-Einstein condensation? For ordinary matter, the wavefunctions of each individual particle are all very different. On average one may expect it improbable to be allowed to move a particle a long way from $\boldsymbol{r}$ to $\boldsymbol{r}'$. A Bose-Einstein condensate on the other hand is more like a coherent gas: throughout the condensate the atomic wavefunctions all overlap one another, and each occupies the same state. From this viewpoint, moving

a particle from $\boldsymbol{r}$ to $\boldsymbol{r}'$ is more likely.

Note that for an ideal Bose gas at $T = 0$ all of the atoms are Bose-condensed and the condensate fraction, Eq. (1.9), is $N_0/N = 1$. However, when there are interactions between the particles, even at $T = 0$ we have $N_0/N < 1$. The effect of interactions between particles play a crucial role in ultracold quantum gases and will be discussed in more detail starting in Chapter 2.

1.3 Second Quantization

Since the field operators $\hat{\Psi}(\boldsymbol{r})$ which compose the one-body density matrix have only been sparsely mentioned, we endeavor to describe them here in more detail, starting from their origins in second quantization. The field operators $\hat{\Psi}(\boldsymbol{r})$ hold information on the full quantum many-body behavior of the system. The field operator concept appears in the second quantization formalism of quantum mechanics,[4] for which there are many good references [21, 22, 23].

One approach to the second quantization formalism is to focus on many-body basis functions which specify the state, $\chi_i(\alpha)$, that each individual particle occupies. The states are enumerated by the index i; the quantity α can stand for any independent variable necessary to characterize the system, for example, the coordinates, the spin, or other degrees of freedom. The set of the basis functions, $\chi_1(\alpha)$, $\chi_2(\alpha), \ldots$, form a complete set of normalized and orthonormal functions. Using a combination of basis states, a full many-body wavefunction can be constructed, in principle, for any system of interest. Additional features may be required, for example, when dealing with a system of N identical bosons, the rules of Bose statistics demand that the full many-body wavefunction remain completely symmetric under the exchange of any two particles.

For Bose-Einstein condensates, our systems have, by definition, many particles occupying the same single-particle state. Therefore, it is often convenient to use a

[4] In 1927 P. A. M. Dirac first used the second quantization method to describe a system of photons. In 1928 fermions were later added by E. Wigner and P. Jordan.

basis of occupation numbers, $n_1, n_2, \ldots$, which tell how many particles occupy each of the available states, $\chi_1(\alpha)$, $\chi_2(\alpha), \ldots$. The occupation numbers are positive integers less than or equal to N and play the role of quantum numbers describing the state. For example, the occupation state $\big|n_i\big\rangle$ describes a situation in which n_i particles occupy the single particle state χ_i.

The full many-body state can then be represented as, $\big|n_1, n_2, \ldots, n_i, \ldots\big\rangle$, which in general is a tensor product of the individual states $\big|n_i\big\rangle$, that is,

$$\big|n_1, n_2, \ldots, n_i, \ldots\big\rangle = \prod_i \big|n_i\big\rangle. \tag{1.15}$$

In second quantization, operators change the number of particles that occupy a given state. The creation operator, $\hat{b}_i^\dagger$, adds a particle to state i, while the destruction operator, $\hat{b}_i$, destroys a particle in state i. The creation and destruction operators change the many-body state in the following way:

$$\hat{b}_i^\dagger\big|n_1, n_2, \ldots, n_i, \ldots\big\rangle = \sqrt{n_i + 1}\big|n_1, n_2, \ldots, n_i + 1, \ldots\big\rangle, \tag{1.16}$$

$$\hat{b}_i\big|n_1, n_2, \ldots, n_i, \ldots\big\rangle = \sqrt{n_i}\big|n_1, n_2, \ldots, n_i - 1, \ldots\big\rangle, \tag{1.17}$$

and obey the commutation rules,

$$[\hat{b}_i, \hat{b}_j] = [\hat{b}_i^\dagger, \hat{b}_j^\dagger] = 0, \quad [\hat{b}_i, \hat{b}_j^\dagger] = \delta_{ij}. \tag{1.18}$$

Note that if the destruction operator acts on a vacuum state with no particles, the vacuum state is unchanged.

The second quantization formalism will be used throughout this thesis to describe field operators, many-body wavefunctions, and for many other purposes. For example, we will be able to conveniently express the governing Hamiltonian of our many-body system, the so–called Bose Hubbard Hamiltonian, in terms of the creation and destruction operators defined above.

1.4 Field Operators and the Order Parameter

The field operators can be expressed in terms of a combination of the single particle wavefunctions, $\chi_i(\boldsymbol{r})$,[5] and the creation $\hat{b}_i^\dagger$ and annihilation $\hat{b}_i$ operators, such that

$$\hat{\Psi}(\boldsymbol{r}) = \sum_i \hat{b}_i \; \chi_i(\boldsymbol{r}). \tag{1.19}$$

Following in part from Eq. 1.18, the field operators $\hat{\Psi}(\boldsymbol{r})$ satisfy the following useful commutation relations:

$$\left[\hat{\Psi}(\boldsymbol{r}), \hat{\Psi}^\dagger(\boldsymbol{r}')\right] = \delta(\boldsymbol{r} - \boldsymbol{r}'), \quad \left[\hat{\Psi}(\boldsymbol{r}), \hat{\Psi}(\boldsymbol{r}')\right] = 0, \quad \left[\hat{\Psi}^\dagger(\boldsymbol{r}), \hat{\Psi}^\dagger(\boldsymbol{r}')\right] = 0. \tag{1.20}$$

As discussed in Section 1.2, BEC occurs when there is a macroscopic occupation of a single particle state, $\chi_0(\boldsymbol{r})$. Separating out this term in Eq. (1.19) the condensate term can be clearly distinguished from the others,

$$\hat{\Psi}(\boldsymbol{r}) = \hat{b}_0 \; \chi_0(\boldsymbol{r}) + \sum_{i \neq 0} \hat{b}_i \; \chi_i(\boldsymbol{r}). \tag{1.21}$$

In mean field theory, the main quantity describing the single-particle state that the system Bose-condenses to is the *order parameter*, or the wavefunction of the condensate. The order parameter can be obtained from Eq. (1.21) using what is known as the Bogoliubov approximation. The critical step in this approximation is to ignore the non-commutativity between the operators $\hat{b}$ and $\hat{b}^\dagger$ and treat them as complex scalars, called "c-numbers," equal to $\sqrt{N_0}\;\hat{\mathbb{I}}$, where $\hat{\mathbb{I}}$ is the identity operator [19, 20, 24]. This is equivalent to breaking the bosonic field operator into a condensate mean field term, $\Psi_0 = \sqrt{N_0}\chi_0(\boldsymbol{r})$, and a fluctuation term, $\hat{\zeta}(\boldsymbol{r}) = \sum_{i \neq 0} \hat{b}_i \chi_i(\boldsymbol{r})$, to obtain,

$$\hat{\Psi}(\boldsymbol{r}) = \Psi_0(\boldsymbol{r})\hat{\mathbb{I}} + \hat{\zeta}(\boldsymbol{r}), \tag{1.22}$$

[5] Note we have taken α to simply be the coordinates $\boldsymbol{r}$.

where $\Psi_0(\boldsymbol{r})$ is the order parameter, or the mean field wavefunction of the condensate, and $\hat{\zeta}(\boldsymbol{r})$ represents the quantum fluctuations around the mean field. If we neglect the quantum fluctuations $\hat{\zeta}(\boldsymbol{r})$, we obtain $\Psi_0(\boldsymbol{r}) = \langle \hat{\Psi}(\boldsymbol{r}) \rangle$, and likewise $\Psi_0^*(\boldsymbol{r}) = \langle \hat{\Psi}^\dagger(\boldsymbol{r}) \rangle$.

The seemingly ad hoc substitution of $\hat{b}_0 = \hat{b}_0^\dagger = \sqrt{N_0}\hat{\mathbb{I}}$ in the Bogoliubov approximation will be explained more clearly in Chapter 2, but for now consider the following: in a BEC there is a macroscopic number of particles $N_0 \gg 1$, thus, adding or removing one particle from the system will not drastically affect the physical properties of the system.[6] From this line of reasoning it may seem plausible that the creation and destruction operators can be replaced by a scalar. Since the order parameter can be expressed as the expectation value of the full many-body wavefunction, $\Psi_0(\boldsymbol{r}) = \langle \hat{\Psi}(\boldsymbol{r}) \rangle$, if we compute the average using stationary states and follow the $e^{iEt/\hbar}$ law, we can define a time-dependent order parameter, which takes the form,

$$\Psi_0(\boldsymbol{r}, t) = \Psi_0(\boldsymbol{r}) e^{-i\mu t/\hbar}, \tag{1.23}$$

where $\mu = \partial E/\partial N$ is the chemical potential [20]. Equation (1.23) will play an important role for us in the future. For example, in Chapter 3, we will look for stationary states of the equations of motion governing the order parameter to find solitons in BECs. Rather than depending explicitly on the energy of the system, note that the time-dependent order parameter directly depends on the chemical potential.

[6] Provided that we add or remove atoms slowly, so as to avoid excitations in $\hat{\zeta}(\boldsymbol{r})$.

Chapter 2

BOSE-EINSTEIN CONDENSATION AND OPTICAL LATTICES

In this chapter we review some of the fundamental principles of BEC and optical lattices. First, we describe weakly-interacting Bose gases from a mean field perspective, as prescribed by the Gross-Pitaevskii equation. Mean field theory provides a useful first approximation of the behavior of our system, in terms of a physically intuitive set of parameters. Next, we will discuss the theory of optical lattices. Optical lattices provide a remarkable means of control and manipulation of atoms, allowing us to investigate previously intractable many-body phenomena, such as macroscopic quantum tunneling. Within the context of optical lattices, we then derive the quantum many-body Hamiltonian for our system, the Bose Hubbard Hamiltonian, and discuss its properties. Finally, we will extend the mean field theory to include optical lattices, as encapsulated in the discrete nonlinear Schrödinger equation.

2.1 Weakly-Interacting Bose Gases: Bogoliubov Theory

Consider a Bose gas at zero temperature with a fixed density, $n = N/V$, that is composed of N particles and comprises a volume V. The many-body Hamiltonian for such a system can be described in terms of the field operators $\hat{\Psi}^\dagger(\boldsymbol{r})$ and $\hat{\Psi}(\boldsymbol{r})$, which, using the notation of second quantization, may be written as

$$\begin{aligned}\hat{H} = &\int d\boldsymbol{r}\hat{\Psi}^\dagger(\boldsymbol{r})\left[-\frac{\hbar^2}{2m}\nabla^2 + V(\boldsymbol{r})\right]\hat{\Psi}(\boldsymbol{r}) \\ &+ \frac{1}{2}\int d\boldsymbol{r}\int d\boldsymbol{r}'\hat{\Psi}^\dagger(\boldsymbol{r})\hat{\Psi}^\dagger(\boldsymbol{r}')V_{\text{int}}(\boldsymbol{r}-\boldsymbol{r}')\hat{\Psi}(\boldsymbol{r})\hat{\Psi}(\boldsymbol{r}'). \qquad (2.1)\end{aligned}$$

In Eq. (2.1), $\hat{\Psi}^\dagger(\boldsymbol{r})$ and $\hat{\Psi}(\boldsymbol{r}')$ are field operators which respectively create a particle at $\boldsymbol{r}$ or destroy a particle at $\boldsymbol{r}'$. The operator $V(\boldsymbol{r})$ encapsulates any external potentials, for example, the potential of an underlying optical lattice or an external potential

barrier used for tunneling. The operator $V_{\rm int}$ is the potential associated with the interactions between particles.

The s-wave scattering length, a, is an experimentally measurable parameter which can be used to determine the strength and the sign of the particle interactions of a Bose gas. For attractive interactions $a < 0$ and for repulsive interactions $a > 0$. In the vicinity of a magnetically induced Feshbach resonance, it is well known that a is extremely sensitive to changes in the magnitude of a magnetic field, hence permitting the atomic interactions of the condensate to be tuned to any value, over a range of seven orders of magnitude [25, 26, 27, 28, 29]. Using this now well-established method, it is possible to realize small negative scattering lengths experimentally, which are the primary focus of this thesis.

The actual interatomic potential, $V_{\rm int}$, between atoms in the Bose gas may be quite complex. However, for a sufficiently dilute, weakly-interacting Bose gas at low temperatures, the energy of scattering events is extremely low, and the atoms rarely get close enough to one another to see the complicated nature of the interatomic potential. By dilute and weakly-interacting, we mean that the range of the interatomic interactions is typically much smaller than the average distance between the particles,

$$|a| \ll d = n^{-1/3}. \tag{2.2}$$

The assumption of Eq. (2.2) allows for some progress to be made in simplifying the integrals within the Hamiltonian.

In order to work out the many-body theory in the simplest way, the usual approach is to replace the actual interatomic two-body potential, $V_{\rm int}$, with a contact potential, $V_{\rm eff}$, provided that $V_{\rm eff}$ gives the same s-wave scattering length. This approach has been proven to be correct via renormalization theory [24]. To very good approximation, we will assume that only binary contact collisions are relevant in the

interatomic potential, i.e. the interatomic potential takes the form of a delta function,

$$V_{\text{int}}(\boldsymbol{r}-\boldsymbol{r}') \approx V_{\text{eff}}(\boldsymbol{r}-\boldsymbol{r}') = g\ \delta(\boldsymbol{r}-\boldsymbol{r}'), \tag{2.3}$$

scaled by a parameter, g, which is proportional to the s-wave scattering length via,

$$g \equiv \int d\boldsymbol{r}\ V_{\text{int}}(\boldsymbol{r}) = \frac{4\pi\hbar^2 a}{m}. \tag{2.4}$$

In this approximation, the exclusion of three-body and higher collisions in the interatomic potential is very reasonable. When making BECs experimentally, one works at very low densities to prevent three-body recombination, in which two atoms will combine to form a diatomic molecule, while the third takes away the excess energy, kicking both out of the trap.

Although, the approximation made in Eq. (2.3) is a good one, it is easy to forget how crucial atomic losses are to experiments. Atomic BECs only survive on the order of one to a hundred seconds before losses destroy the condensate. Three-body losses can be a problem for experimentalists, because when molecules form, the trap will be unable to hold those with a magnetic moment. Additionally, BECs composed of alkali atoms are fundamentally metastable, having a ground state which is a solid. The formation of molecules provides the gas something to nucleate around,[1] which can prevent the gas from reaching the condensed phase [30]. There is also a possibility for losses to occur when individual atoms are ejected from the condensate because of external agents, such as collisions with background atoms from the imperfect vacuum surrounding the BEC. In principle, the losses from external effects can be mitigated, for instance, by decreasing the atmospheric pressure in the vacuum system, whereas for the more intrinsic three-body losses, the only hope is to work at low densities.

[1] Much in the same way that when cooling water vapor, ice crystals or droplets start to form around dust and impurities in the air.

2.2 Mean Field Theory: The Gross-Pitaevskii Equation

A common inroad to achieving quantitative predictions about the general behavior of a BEC system, while sidestepping the complications of the full many-body problem, is to use a mean field approach. The formulation of a mean field description for dilute Bose gases was first worked out by Bogoliubov in 1947,[2] and is documented extensively throughout the literature [20, 24, 31].

As evident from Section 1.4, the aim of mean field theory is to describe the behavior of the order parameter, and to do so we need an equation to govern the dynamics. To obtain an equation of motion for the order parameter we turn to the Heisenberg picture of quantum mechanics, where $\hat{\Psi}(\boldsymbol{r},t)$ satisfies the relation

$$i\hbar\frac{\partial\hat{\Psi}(\boldsymbol{r},t)}{\partial t} = \left[\hat{\Psi}(\boldsymbol{r},t),\hat{H}\right]. \tag{2.5}$$

Using Eq. (2.1) for the Hamiltonian, $\hat{H}$, and simplifying with the commutation relations listed in Eq. (1.20) we obtain [20]

$$\begin{aligned} i\hbar\frac{\partial\hat{\Psi}(\boldsymbol{r},t)}{\partial t} =& \Bigg[-\frac{\hbar^2}{2m}\nabla^2 + V(\boldsymbol{r},t) \\ &+ \int d\boldsymbol{r}'\hat{\Psi}^\dagger(\boldsymbol{r}',t)V(\boldsymbol{r}'-\boldsymbol{r})\hat{\Psi}(\boldsymbol{r}',t)\Bigg]\hat{\Psi}(\boldsymbol{r},t). \end{aligned} \tag{2.6}$$

The mean field approximation is now manifested through the replacement of the field operator $\hat{\Psi}(\boldsymbol{r},t)$ with the order parameter $\Psi_0(\boldsymbol{r},t)$ in Eq. (2.6). Looking back to Eq. (1.22), this is only justifiable when quantum fluctuations around the mean field, $\hat{\zeta}(\boldsymbol{r})$, are negligible. This is the case for low-energy cold dilute Bose gases, in which only binary contact collisions are relevant in the interatomic potential, i.e. when Eqs. (2.3) and (2.4) are valid. Substituting Eq. (2.3) into Eq. (2.6) we obtain [31]

$$i\hbar\frac{\partial\Psi_0(\boldsymbol{r},t)}{\partial t} = \left[-\frac{\hbar^2}{2m}\nabla^2 + V(\boldsymbol{r},t) + g|\Psi_0(\boldsymbol{r},t)|^2\right]\Psi_0(\boldsymbol{r},t). \tag{2.7}$$

[2] Originally as an attempt to study superfluid ^{4}He.

Equation (2.7) is known as the Gross-Pitaevskii equation and was written down independently by Gross and Pitaevskii in 1961. The Gross-Pitaevskii equation is the equation of motion for the order parameter, and describes the macroscopic properties of a dilute weakly-interacting Bose gas at low temperature. Notice that when we average over the interaction term in the many-body Hamiltonian, one finds an effective nonlinearity, the last term of Eq. (2.7). This nonlinearity will play a crucial role in Chapter 3 when we discuss the formation of solitons. While there are several different conventions for normalization, throughout this thesis we choose to normalize the wavefunction of the condensate to the total number of atoms, $N = \int d\boldsymbol{r}\, |\Psi_0(\boldsymbol{r})|^2$. The Gross-Pitaevskii equation has proven to be very successful in quantitatively describing the properties of Bose-Einstein condensates, including interference effects, vorticies, and collective modes.

It is important to remember the assumptions which must be satisfied for Eq. (2.7) to be valid. First, the s-wave scattering length must be much smaller than the average distance between two atoms in the condensate. Second, to assume binary contact collisions the sample must satisfy the diluteness condition, Eq. (2.2), and be at a sufficiently low temperature. Finally, the number of atoms in the condensate must be much greater than 1, otherwise the concept of Bose-Einstein condensation is not applicable.

From the onset we have assumed a three-dimensional (3D) mean field picture. A quasi one-dimensional (1D) condensate can be formed experimentally by modifying the external trapping potential, which is a part of $V(\boldsymbol{r})$, such that the transverse dimensions of the BEC are on the order of the healing length, and are much smaller than the longitudinal dimension. The healing length, ξ, is a quantity which defines the distance over which the condensate wavefunction tends to its bulk value if subject to a localized perturbation, and can be estimated from Eq. (2.7).

2.2.1 Gross-Pitaevskii Equation: Reduction to One-Dimension

In this section we will derive a nondimensionalized version of the Gross-Pitaevskii equation in 1D. The derivation is reproduced along the same lines as documented in references [32, 33], where additional detail can be found. We assume that our external trapping potential, which is a part of the term $V(\boldsymbol{r})$, is a box of dimensions $L_x \times L_y \times L_z$. The quasi 1D limit is obtained when L_y and L_z obey the following

$$L_y,\ L_z \approx \xi, \qquad L_y,\ L_z \ll L_x \tag{2.8}$$

where $\xi \equiv (8\pi n|a|)^{-1/2}$ is the healing length, $n = N/V \equiv N/(L_x L_y L_z)$ is the mean particle density of the condensate, and N is the total number of atoms.

We would like to separate out the longitudinal dimension x from the small transverse dimensions y and z, so that we can integrate out the transverse coordinates. Following Eq. (1.23), we assume a stationary state and write the order parameter as

$$\Psi_0(\boldsymbol{r}, t) = \sqrt{\frac{N}{L_x L_y L_z}} u(x)\ v(y, z) e^{-i\mu t/\hbar} \tag{2.9}$$

where $u(x)$ and $v(y, z)$ are dimensionless quantities containing the longitudinal and transverse spatial dependence. Substitution of Eq. (2.9) into the Gross-Pitaevskii equation Eq. (2.7) gives

$$\mu\ u(x)\ v(y, z) = \left[-\frac{\hbar^2}{2m}\nabla^2 + \frac{gN|u(x)\ v(y, z)|^2}{L_x L_y L_z} + V(\boldsymbol{r}, t)\right] u(x)\ v(y, z). \tag{2.10}$$

We can project this equation onto the ground state, v_{gs}, of $v(y, z)$, which for a dilute, weakly-interacting system is the particle-in-a-box solution [32] given by

$$v_{gs} = v_0\ \sin(\pi y/L_y)\sin(\pi z/L_z), \tag{2.11}$$

where $v_0 = 2$. To satisfy the normalization condition, the solution must satisfy

$\int_0^{L_y} dy \int_0^{L_z} dz\ |v_{gs}|^2 = 1$. Then we integrate over the transverse directions y and z to obtain,

$$0 = \int_0^{L_y} dy \int_0^{L_z} dz\ v_{gs}^*(y,z)\Big[-\mu - \frac{\hbar^2}{2m}\nabla^2 + \frac{gN|u(x)\ v(y,z)|^2}{L_x L_y L_z} + V(x,y,z,t)\Big] u(x)\ v(y,z). \tag{2.12}$$

We can say that $v(y,z)$ approaches $v_{gs}(y,z)$ in the limit of Eq. (2.8), so by the normalization condition for v_{gs} the integral becomes

$$\left[-\mu - \frac{\hbar^2}{2m}\left(\frac{\partial^2}{\partial x^2} - \frac{\pi^2}{L_y^2} - \frac{\pi^2}{L_z^2}\right) + \frac{9}{4}\frac{gN}{L_x L_y L_z}|u(x)|^2 + V(x,y,z,t)\right] u(x) = 0, \tag{2.13}$$

where $V(x,y,z,t)$ is assumed to be a constant or piecewise constant function in y and z. Multiplying through by a factor of $2m\xi^2/\hbar^2$ and using the definition of ξ and g we find

$$\left[-\bar{\mu} - \xi^2\frac{\partial^2}{\partial x^2} + \frac{\pi^2\xi^2}{L_y^2} + \frac{\pi^2\xi^2}{L_z^2} + \frac{9}{4}|u(x)|^2 + \bar{V}(x,y,z,t)\right] u(x) = 0, \tag{2.14}$$

where $\bar{\mu} = (2m\xi^2/\hbar^2)\mu$ and $\bar{V} = (2m\xi^2/\hbar^2)V$. To nondimensionalize the equation above consider a change of variables, taking $\tilde{x} \equiv x/L_x$. Using the quasi 1D limit, L_x and L_z can be approximated by the healing length, ξ. Thus, dividing through by a factor of $9/4$ we obtain

$$\tilde{\mu}\ u(\tilde{x}) = \left[-\tilde{J}\frac{\partial}{\partial \tilde{x}} + |u(\tilde{x})|^2 + \tilde{V}(x,y,z,t)\right] u(\tilde{x}), \tag{2.15}$$

where $\tilde{\mu} \equiv 4/9\bar{\mu} - 8/9\pi^2$, $\tilde{J} \equiv 4/9(\xi/L_x)^2$, and $\tilde{V} \equiv 4/9\bar{V}$. The normalization condition for $u(\tilde{x})$ is $\int_0^1 d\tilde{x}\ |u(\tilde{x})|^2 = 1$. Equation (2.15) is the quasi 1D nondimensionalized Gross-Pitaevskii equation. The solutions for $u(\tilde{x})$ can be written in terms of Jacobi elliptic functions.

2.3 Optical Lattices and Ultracold Atoms

Optical potentials formed by the interference of counter-propagating laser beams are the basic tool for creating ultracold lattice gases and provide an unprecedented level of control over the relevant experimental parameters. In this section we describe how atoms are trapped in optical lattices via the AC Stark shift.

Consider an atom in the electronic ground state $|g\rangle$, which may be coupled to an internal excited state $|e\rangle$ by a single-mode laser with frequency ω_L. The energy difference between $|g\rangle$ and $|e\rangle$ is $\hbar\omega_{eg}$. The oscillating electric field, $\boldsymbol{E}(\boldsymbol{r},t)$, of the laser will impart electrons in the atom with a time-dependent dipole moment $\boldsymbol{d}$. If w_L is far from the frequencies required to make transitions to any state besides $|e\rangle$, then the induced dipole moment will follow the oscillations of the laser such that [34],

$$d_i = \sum_{j=x,y,z} \alpha_{ij}(\omega_L) E_j(\boldsymbol{r},t), \tag{2.16}$$

where d_i is the corresponding component of $\boldsymbol{d}(i = x,y,z)$ and $\alpha_{ij}(\omega_L)$ are the matrix elements of the electric polarizability tensor, which is dependent on the laser frequency. The electric polarizability tensor is inversely proportional to the detuning of the laser from resonance $\delta = \omega_L - \omega_{eg}$, when the excited state $|e\rangle$ is much closer to resonance than any of the other excited states.

In this situation there is an energy shift δE due to the quadratic[3] AC Stark effect that is proportional to the intensity of the laser beam $I(\boldsymbol{r})$,

$$\delta E(\boldsymbol{r}) = \sum_{i,j=x,y,z} \alpha_{ij}(\omega_L) \langle E_j^2(\boldsymbol{r},t)\rangle \propto I(\boldsymbol{r})/\delta. \tag{2.17}$$

The Stark shift in Eq. (2.17) is of great consequence because it causes the atom to feel an optical potential $V_{\text{lat}}(\boldsymbol{r}) \equiv \delta E(\boldsymbol{r}) \propto I(\boldsymbol{r})/\delta$ conforming to the spatial orientation of the light field. Note that the sign and strength of the optical potential may be

[3]Second order in perturbation theory.

modified by controlling the detuning from resonance δ. If the lattice is blue-detuned

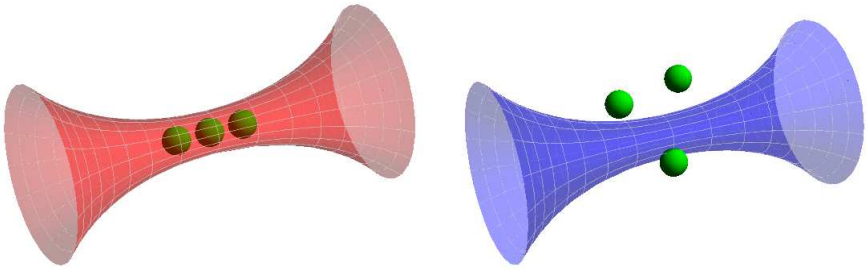

Figure 2.1: *A Gaussian Laser Focus and a Red- and Blue-Detuned Trap.* A schematic drawing of a Gaussian laser focus for red- and blue-detuned optical lattices. A red-detuned lattice attracts atoms to points of maximum intensity (left), while a blue-detuned lattice attracts atoms to points of zero intensity (right).

($\delta > 0$) then atoms are attracted to points of zero light intensity, where the optical potential is minimized. In a red-detuned lattice ($\delta < 0$), due to the sign change, atoms are attracted to points of maximum light intensity, where the potential is most negative. Figure 2.1 shows a Gaussian laser focus and a red- and blue-detuned lattice.

A critical factor in the design of optical lattices is to reduce the effective rate of spontaneous emissions Γ_{eff}, a quantum jump made by the emission of a photon accompanied by a transition from $|e\rangle \rightarrow |g\rangle$. Spontaneous emission, in practice, is one of the largest sources of decoherence, shifting the atomic dynamics from obeying a Schrödinger equation with an optical lattice potential to a stochastic Schrödinger equation [35]. Consequently, it is often preferable for experiments to be performed on time scales smaller than $1/\Gamma_{eff}$, which is generally on the order of minutes.

Two cross-propagating lasers beams of the same frequency and polarization can be arranged to form a standing wave, thus creating a spatially oscillating potential for the atoms. If three pairs of cross-propagating laser beams are oriented perpendicular to one another, the interference pattern results in a 3D cubic lattice. A quasi 1D optical lattice can be formed from a 3D cubic lattice by increasing the intensity of the standing waves in the transverse dimensions such that the probability of hopping in those directions tends to zero. For low enough temperatures, any radial motion

is completely frozen out. Using an arrangement of counter-propagating laser beams, practically any lattice geometry can be attained through optical potentials. These potentials are the primary basis for the optical manipulation and trapping of ultracold atoms.

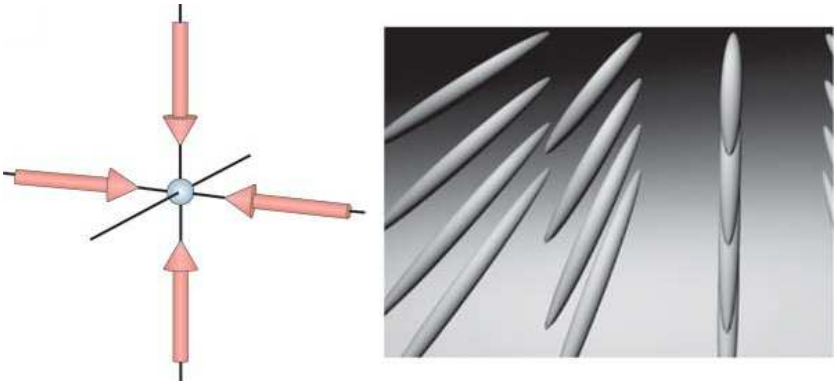

Figure 2.2: *A network of 1D optical lattices.* A schematic drawing of 1D optical lattices, where atoms are arranged in a network of tightly confined 1D potential tubes. The lattice is formed by two orthogonal standing waves. Figure from I. Bloch [36].

The resulting arrangement of trapped atoms behaves analogously to electrons in a crystal lattice. Instead of interacting with a Coulomb potential created by ionized atoms, the ultracold atoms are susceptible to the potential created by the laser light through the AC Stark effect. Unlike their solid state counterparts, optical lattice systems have several distinct advantages. The periodic potentials formed by optical lattices are ideal, that is, they are defect and impurity free. The lattice sites are also rigid, in that they are devoid of the phonon excitations, which are normally present in naturally-occurring crystals.

Optical lattices offer an immense level of control over the atoms and the underlying lattice, thus allowing for the exploration of many phenomena analogous to electrons in crystals. Indeed, optical lattices have been used to produce elegant studies of band structure [37, 38, 39], Bloch oscillations [40], and interferometry with coherent matter waves [41, 42].

2.4 Bose Hubbard Hamiltonian

Under the proper conditions, ultracold atoms loaded in an optical lattice are a nearly perfect realization of the Bose Hubbard Hamiltonian (BHH), a model first proposed by M. P. A Fisher *et al.* in 1989 to describe short-range interacting bosons on a lattice. The BHH is analogous to the well-known Hubbard Hamiltonian, introduced by J. Hubbard in 1963, and solved analytically in 1D by J. Wu in 1968, which can describe ultracold fermions in an optical lattice. The focus in this section is to derive the BHH from first principles and explain its properties.

Due to the periodic nature of the optical lattice, we should expect that the system will exhibit two features common to solid state physics: first, that the energy eigenstates for single atoms in the condensate are Bloch functions, and second, that the system possesses an energy band-like structure. The bands will be well separated energetically, i.e. the band-gaps are large, for a sufficiently strong lattice potential. Particles in the lowest bands, with energy less than the height of the lattice potential, will be in bound states, while particles in higher bands will be in free particle states.

In the ultracold temperature regimes typically associated with Bose-Einstein condensates, it is easy to arrange the system so that the particles only occupy the lowest Bloch band. In order to make such a restriction, the gaps between the bands must be sufficiently large in comparison to the other energy scales of the system. Thus, the energies associated with temperature $k_B T$, the tunneling J, and the interactions U, must all be smaller than the spacing between the bands, $\hbar\omega$. In general, this is a very good assumption when working at typical experimental temperatures and when the lattice height is greater than or equal to the recoil energy of the atoms. The recoil energy for an atom in a quasi 1D optical lattice is given by $\hbar^2 k_\perp^2/2m$, where $k_\perp \equiv k_y = k_z$ is the wavevector in the transverse dimension.

We begin with the full quantum many-body Hamiltonian from Eq. (2.1), separating the underlying optical lattice potential from the other external potentials,

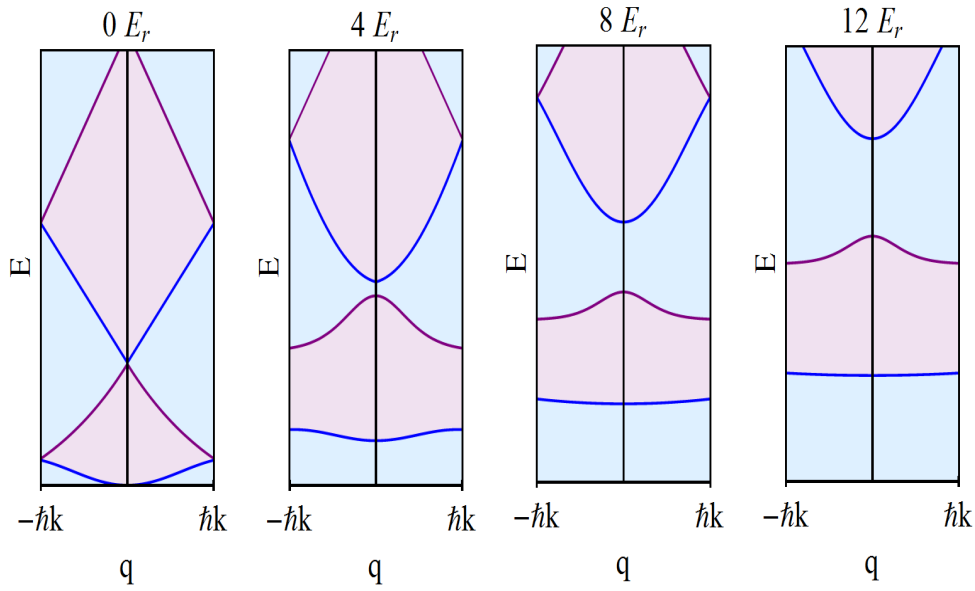

Figure 2.3: *Band Structure in an Optical Lattice.* A schematic diagram of Bloch state energy versus the quasi momentum q in the first Brillouin zone. The band structure is plotted for different lattice depths between 0 and $12E_r$. Colors are simply meant to guide the eye. When the lattice becomes deep the lowest band becomes flat.

$V(\boldsymbol{r}) = V_{\text{lat}}(\boldsymbol{r}) + V_{\text{ext}}(\boldsymbol{r})$, to obtain

$$\hat{H} = \int d\boldsymbol{r}\hat{\Psi}^\dagger(\boldsymbol{r}) \left[-\frac{\hbar^2}{2m}\nabla^2 + V_{\text{lat}}(\boldsymbol{r}) + V_{\text{ext}}(\boldsymbol{r})\right] \hat{\Psi}(\boldsymbol{r}) + \frac{1}{2}g \int d\boldsymbol{r}\hat{\Psi}^\dagger(\boldsymbol{r})\hat{\Psi}^\dagger(\boldsymbol{r})\hat{\Psi}(\boldsymbol{r})\hat{\Psi}(\boldsymbol{r}). \tag{2.18}$$

As in Eq. (2.3), only two-body contact interactions are assumed to participate, thus the interaction potential is set to $V_{\text{int}}(\boldsymbol{r}) = g * \delta(\boldsymbol{r})$. Let the lattice potential be a sinusoidal potential of the form,

$$V_{\text{lat}}(\boldsymbol{r}) = V_{0x}\sin^2(k_x x) + V_{0y}\sin^2(k_y y) + V_{0z}\sin^2(k_z z), \tag{2.19}$$

where V_{0i} and k_i are the lattice height and the wavevector respectively, in the $i = x, y, z$ direction.

The Bloch functions of the lowest band can be more conveniently represented in a basis of Wannier functions that are localized to the individual lattice sites. The advan-

tage gained in changing to a site-localized basis is the simplification when describing on-site interactions between particles. The Wannier functions are not eigenstates of the single particle Hamiltonian, but form a complete set of orthogonal basis functions. In the same vein as Eq. (1.19) we expand the field operators in the Wannier basis such that,

$$\hat{\Psi}(\boldsymbol{r}) = \sum_{i;\,m} \hat{b}_i^{(m)} w^{(m)}(\boldsymbol{r} - \boldsymbol{r}_i), \tag{2.20}$$

where $\hat{b}_i^{(m)}$ destroys a particle from the m^{th} Bloch band in the Wannier state $w^{(m)}(\boldsymbol{r} - \boldsymbol{r}_i)$. Such a particle has primitive translation vectors $\boldsymbol{r}_i$ of the lattice and is localized at site i. The band index is indicated by the superscript indices in parentheses, while the site index is indicated by the subscript indices. Inserting Eq. (2.20) into Eq. (2.18), the Hamiltonian takes the form

$$\hat{H} = -\sum_{i,j;\,m,n} J_{ij}^{mn} \hat{b}_i^{(m)\dagger} \hat{b}_j^{(n)} + \frac{1}{2} \sum_{i,j,k,l;\,m,n,p,q} U_{ijkl}^{mnpq} \hat{b}_i^{(m)\dagger} \hat{b}_j^{(n)\dagger} \hat{b}_k^{(p)} \hat{b}_l^{(q)} + \sum_{i,j;\,m,n} \epsilon_{ij}^{mn} \hat{b}_i^{(m)\dagger} \hat{b}_j^{(n)}, \tag{2.21}$$

where,

$$J_{ij}^{mn} \equiv -\int d\boldsymbol{r}\; w^{(m)^*}(\boldsymbol{r} - \boldsymbol{r}_i) \left[-\frac{\hbar^2}{2m} \nabla^2 + V_{\text{lat}}(\boldsymbol{r}) \right] w^{(n)}(\boldsymbol{r} - \boldsymbol{r}_j), \tag{2.22}$$

$$U_{ijkl}^{mnpq} \equiv g \int d\boldsymbol{r}\; w^{(m)^*}(\boldsymbol{r} - \boldsymbol{r}_i) w^{(n)^*}(\boldsymbol{r} - \boldsymbol{r}_j) w^{(p)}(\boldsymbol{r} - \boldsymbol{r}_k) w^{(q)}(\boldsymbol{r} - \boldsymbol{r}_l), \tag{2.23}$$

$$\epsilon_{ij}^{mn} \equiv \int d\boldsymbol{r}\; w^{(m)^*}(\boldsymbol{r} - \boldsymbol{r}_i) V_{\text{ext}}(\boldsymbol{r}) w^{(n)}(\boldsymbol{r} - \boldsymbol{r}_j). \tag{2.24}$$

Now we apply the tight binding approximation to Eq. (2.21), requiring that only nearest-neighbor tunneling ($j = i \pm 1$ for the first term) and on-site interactions ($j = i$ for the second and third terms) contribute to the energy. We truncate the sum in Eq. (2.21) by neglecting contributions from bands higher than the first, setting $m, n, p, q = 0$. Simplifying leads to the Bose Hubbard Hamiltonian,

$$\hat{H} = -J \sum_{\langle i,j \rangle} \hat{b}_i^\dagger \hat{b}_j + \frac{U}{2} \sum_i \hat{b}_i^\dagger \hat{b}_i^\dagger \hat{b}_i \hat{b}_i + \sum_i \epsilon_i \hat{b}_i^\dagger \hat{b}_i, \tag{2.25}$$

where $\hat{b}_i \equiv \hat{b}_i^{(0)}$ annihilates a boson in the lowest vibrational Wannier state of the i^{th} lattice site and $\langle i, j \rangle$ denotes a summation over only nearest neighbor sites. The coefficient $J \equiv J^{00}_{i(i\pm1)}$ sets the strength of the hopping, $U \equiv U^{0000}_{iiii}$ controls the strength of the on-site interactions, and $\epsilon \equiv \epsilon^{00}_{ii}$ describes any external potentials, such as the barrier potential we will use in our studies of macroscopic quantum tunneling.

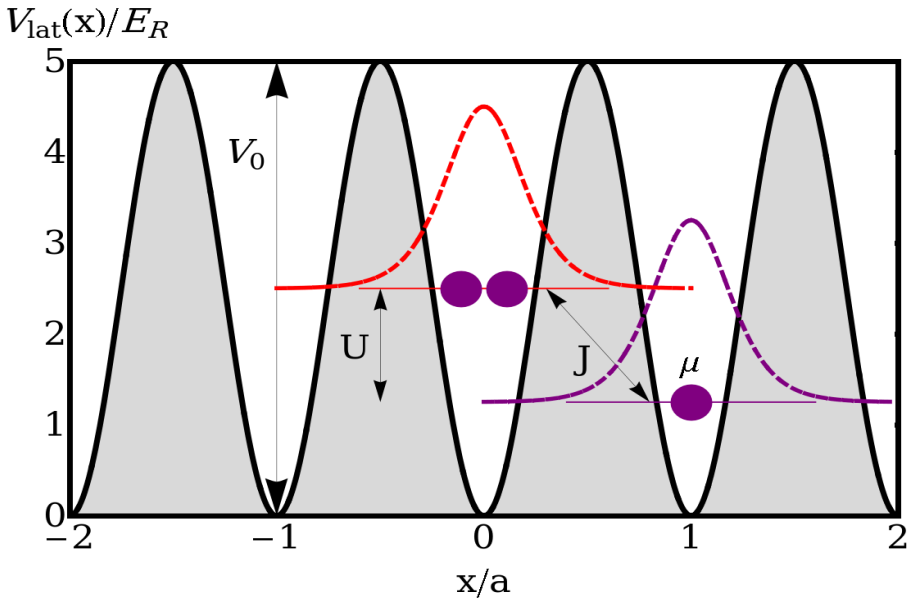

Figure 2.4: *Bose Hubbard model in 1D.* A schematic diagram of the Bose Hubbard model showing the main terms of the Hamiltonian due to hopping J, interatomic interactions U, and the chemical potential μ.

2.4.1 Bose Hubbard Hamiltonian: Reduction to One-Dimension

As discussed previously, a 3D lattice system can be reduced to a 1D system by ramping up the lattice strength in the transverse directions, and thereby greatly reducing the probability of tunneling in those directions. For a 1D lattice in the x-direction we set $V_{0x} \ll V_{0y}, V_{0z}$. Applying this condition to Eq. (2.25) we obtain the 1D Bose Hubbard Hamiltonian, assuming box boundary conditions for L sites,

$$\hat{H} = -J \sum_{i=1}^{L-1} (\hat{b}_i^\dagger \hat{b}_{i+1} + \hat{b}_i \hat{b}_{i+1}^\dagger) + \frac{U}{2} \sum_{i=1}^{L} \hat{n}_i (\hat{n}_i - I) + \sum_i \epsilon_i \hat{n}_i. \tag{2.26}$$

Here $\hat{b}_i^\dagger$ ($\hat{b}_i$) are creation (annihilation) operators and $\hat{n}_i \equiv \hat{b}_i^\dagger \hat{b}_i$ is the number operator, which counts the number of bosons at site i. In the 1D limit, for a lattice spacing $a_L = \pi/k$, the coefficients in Eqs. (2.22)-(2.24) involve overlap integrals of Wannier functions of the lowest band and the potentials:

$$J \equiv -\int_{-\infty}^{\infty} dx\ w^{(0)*}(x) \left[\frac{-\hbar^2}{2m}\frac{d^2}{dx^2} + V_{\text{lat}}(x)\right] w^{(0)}(x - a_L), \tag{2.27}$$

$$U \equiv g^{(1)} \int_{-\infty}^{\infty} dx\ |w^{(0)}(x)|^4, \tag{2.28}$$

$$\epsilon_i \equiv \int_{-\infty}^{\infty} dx\ |w^{(0)}(x - x_i)|^2 \approx V_{\text{ext}}(x_i). \tag{2.29}$$

Equation (2.26) is the Hamiltonian that will be used throughout this thesis for the quantum many-body description of bosons in 1D optical lattices. Having derived the governing Hamiltonian of our system, it is important to review the circumstances under which Eq. (2.26) is an accurate physical description of our system:

1. The interatomic potential V_{int} is restricted to include only two-body contact interactions. Three-body and higher order collisions can be safely neglected when working at the low-densities typical of experiment.

2. The system must satisfy the tight binding approximation, that is, we can safely neglect interactions and tunneling that extend beyond nearest-neighbors.

3. Contributions from bands higher than the first are neglected. This assumption is valid when the energies associated with temperature, interactions, and tunneling, are all less than or equal to the band spacing $\hbar\omega$. Such conditions can be achieved when $V_0 \geq E_R$, where V_0 is the lattice depth and E_R is the recoil energy of the particles.

4. The strength of the particle-particle interactions cannot be excessively large, so as to distort the single-particle wavefunctions, that is $(N/L)^2 U \leq \hbar\omega$.

2.5 Comparison to Experimental Parameters

The coefficients J and U in this model can be compared to experimental parameters like the lattice height, V_0, and the recoil energy, E_R. For a 1D system, if we approximate the Wannier functions to be the ground state of the simple harmonic oscillator and evaluate the integrals and simplify we obtain

$$\frac{J}{E_R} \approx \frac{V_0}{2E_R} \exp\left(\frac{-\pi^2}{4}\sqrt{\frac{V_0}{E_R}}\right)\left[\frac{\pi^2-2}{2} - \sqrt{\frac{E_R}{V_0}} - \exp\left(-\sqrt{\frac{E_R}{V_0}}\right)\right], \tag{2.30}$$

$$\frac{U}{E_R} \approx 4\sqrt{2\pi}\left(\frac{a_L}{\lambda}\right)\left(\frac{V_{0\perp}}{E_R}\right)^{1/2}\left(\frac{V_0}{E_R}\right)^{1/4}, \tag{2.31}$$

where $\lambda = 2a_L$ is the laser wavelength used to create the lattice. Another way to find U and J is to use the Fourier transform of Mathieu functions [43, 44]. These are exact solutions of the single-particle Schrödinger equation for a sinusoidal potential. By calculating the integrals and performing a numerical fit to the data we obtain

$$\frac{J}{E_R} \approx A\left(\frac{V_0}{E_R}\right)^B \exp\left(-C\sqrt{\frac{V_0}{E_R}}\right), \tag{2.32}$$

where $A \equiv 1.397$, $B \equiv 1.051$, and $C \equiv 2.121$.

2.6 Discrete Nonlinear Schrödinger Equation

The mean field theory encapsulated in the Gross-Pitaevskii equation can be extended to describe a system of ultracold atoms loaded into an optical lattice. This will recast the mean field methods discussed previously in the same optical lattice language as the BHH. In turn, we will then be able to make a direct comparison between mean field and full quantum many-body calculations. The procedure amounts to discretization of the continuous Gross-Pitaevskii equation in order to obtain the so-called discrete nonlinear Schrödinger equation (DNLS). Later, we will perform a much more physically intuitive derivation of the DNLS, through a semiclassical ap-

proximation of the BHH.

First, working in the lowest Bloch band of the lattice, we expand the condensate wavefunction $\mathbf{\Psi}_0$ in a basis of localized wave functions $\phi_i(\boldsymbol{r}-\boldsymbol{r}_i,t)$ such that,

$$\mathbf{\Psi}_0(\boldsymbol{r},t)=\sum_i \phi_i(t)\psi_0(\boldsymbol{r}-\boldsymbol{r}_i). \tag{2.33}$$

In Eq. (2.33) the terms, $\phi_i(t)\equiv\sqrt{\rho_i(t)}e^{i\theta_i(t)}$, are dimensionless c-numbers weighting the localized wave functions at sites i. The quantity, ρ_i, is the average particle number occupation and θ_i is the phase on the i^{th} site. By phase we mean the phase associated with the dominant mode of the single-particle density matrix, that is, the BEC. By combining Eq. (2.33) with the Gross-Pitaevskii equation we obtain

$$i\hbar\frac{\partial\phi_k}{\partial t}=-J\sum_{j\in\Omega_k}(\phi_{k+1}+\phi_{k-1})+U|\phi_k|^2\phi_k+\epsilon_k\phi_k, \tag{2.34}$$

where Ω_k denotes site k's nearest-neighbor sites and the coefficients are defined by the integrals

$$J\equiv-\int d\boldsymbol{r}\ \phi^*(\boldsymbol{r})\left[\frac{-\hbar^2}{2m}\frac{d^2}{dx^2}+V_{\text{int}}(\boldsymbol{r})\right]\phi(\boldsymbol{r}-\boldsymbol{a}), \tag{2.35}$$

$$U\equiv g\int d\boldsymbol{r}\ |\phi(\boldsymbol{r})|^4, \tag{2.36}$$

$$\epsilon_k\equiv\int d\boldsymbol{r}\ V_{\text{ext}}(\boldsymbol{r})|\phi(\boldsymbol{r}-\boldsymbol{r}_k)|^2\approx V_{\text{ext}}(\boldsymbol{r}_k), \tag{2.37}$$

where $\boldsymbol{a}\equiv\boldsymbol{r}_{k+1}-\boldsymbol{r}_k$ is a primitive translation vector for a cubic optical lattice. We invoke the tight binding approximation, thus assuring that $\phi(\boldsymbol{r}-\boldsymbol{r}_i)$ are localized to only a single site. This collapses Eq. (2.34) into the final form of the DNLS, given by

$$i\hbar\frac{\partial\phi_k}{\partial t}=-J(\phi_{k+1}+\phi_{k-1})+U|\phi_k|^2\phi_k+\epsilon_k\phi_k, \tag{2.38}$$

where the coefficients J, U, and ϵ_k, are the same as Eqs. (2.35)- (2.37) with $\boldsymbol{r}$ replaced by x, for a 1D lattice of L sites, with site index $k\in(1,2,\ldots,L)$.

An alternate method of deriving the DNLS can be found by taking a mean field approximation of the Bhh, assuming that the many-body state is in the form of a product of Glauber coherent states. First, we evolve the destruction operator forward in time using the Heisenberg picture of quantum mechanics,

$$i\hbar\frac{d}{dt}\hat{b}_k = [\hat{b}_k, \hat{H}]. \tag{2.39}$$

Using the commutation relations,

$$[\hat{b}_i, \hat{b}_j] = [\hat{b}_i^\dagger, \hat{b}_j^\dagger] = 0 \;\text{ and }\; [\hat{b}_i, \hat{b}_j^\dagger] = \delta_{i,j}, \tag{2.40}$$

we find that,

$$i\hbar\frac{d}{dt}\hat{b}_k = -J(\hat{b}_{k+1} + \hat{b}_{k-1}) + U\hat{b}_k\hat{b}_k^\dagger\hat{b}_k + \epsilon_k\hat{b}_k. \tag{2.41}$$

Taking the expectation value, we obtain an equation of motion for the order parameter $\langle\hat{b}_k\rangle \equiv \phi_k$. If the expectation value is taken with respect to a product of atom-number Glauber coherent states of the form,

$$|\Psi\rangle = \bigotimes_{k-1}^{L}|\phi_k\rangle, \quad \text{where} \quad |\phi_k\rangle \equiv \exp\left(-\frac{|\phi_k|^2}{2}\sum_{n=0}^{\infty}\frac{(\phi_k)^n}{\sqrt{n!}}|n\rangle\right), \tag{2.42}$$

we recover the DNLS exactly:

$$i\hbar\frac{d\phi_k}{dt} = -J(\phi_{k+1} + \phi_{k-1}) + U|\phi_k|^2\phi_k + \epsilon_k\phi_k. \tag{2.43}$$

The Glauber coherent states in Eq. (2.42) well describe the ground state of the BHH in the limit $J \gg U$ for an infinite system with a fixed filling $\nu \equiv N/L$.

Chapter 3

SOLITONS AND QUANTUM TUNNELING

In this chapter, we discuss solitons in Bose-Einstein condensates, an emergent phenomena which is observed even in the context of mean field theory. Then, we will discuss the fundamental principles of macroscopic quantum tunneling in the context of matter-wave solitons, and give an overview of several semiclassical methods used to determine tunneling rates. Finally, we will discuss several experimental applications for solitons in BECs.

Solitons have a long, storied history, beginning in 1834, when John Scott Russel, a Scottish naval engineer, discovered solitons quite unexpectedly while conducting experiments to improve the design for canal boats. In his own words:

> "I was observing the motion of a boat which was rapidly drawn along a narrow channel by a pair of horses, when the boat suddenly stopped–not so the mass of water in the channel which it had put in motion; it accumulated round the prow of the vessel in a state of violent agitation, then suddenly leaving it behind, rolled forward with great velocity, assuming the form of a large solitary elevation, a rounded, smooth and well-defined heap of water, which continued its course along the channel apparently without change of form or diminution of speed. I followed it on horseback, and overtook it still rolling on at a rate of some eight or nine miles an hour, preserving its original figure some thirty feet long and a foot to a foot and a half in height. Its height gradually diminished, and after a chase of one or two miles I lost it in the windings of the channel. Such, in the month of August 1834, was my first chance interview with that singular and beautiful phenomenon which I have called the Wave of Translation."
>
> -J. S. Russell [45]

A theoretical explanation of the phenomenon was given by Korteweg and de Vries in the nineteenth century; however, it was not until after 1965, when Zabusky and Kruskal proved, with numerical simulations, that these solitary waves retain their shape in collisions [46, 47]. It is because of this unique property, that they are now referred to as *solitons*.

In BECs solitons are special solutions of the time-dependent Gross-Pitaevskii equation, Eq. (2.7), which correspond to localized, robust waves propagating over long distances without changing shape or attenuating. These unique properties stem from the binary interactions between atoms, the sign and magnitude of which are determined by the s-wave scattering length, a, for the low-energy collisions in ultracold quantum gases. Averaging over the interaction term in the many-body Hamiltonian, one finds an effective nonlinearity. The nonlinearity, in turn, exactly counteracts the dispersive tendencies of the wave packet. Solitons regularly appear in a diverse set of contexts outside of ultracold atoms, because many systems are well-described by nonlinear wave equations. Solitons find applications in media such as water waves, photonic crystals, molecular biology, astrophysics, and for long distance communication over fiber optic cables [48, 49, 50].

3.1 Matter-Wave Solitons via Mean Field Theory: Bright Solitons

To find matter-wave solitons in BECs, we begin by looking for stationary states of the Gross-Pitaevskii equation, Eq. (2.7), in the spirit of Eq. (1.23). Such states may be formed by assuming an exponential time dependence for the order parameter, that is

$$\Psi_0(\boldsymbol{r}, t) = \Psi_0(\boldsymbol{r}) e^{-i\mu t/\hbar}, \tag{3.1}$$

where $\mu = \partial E/\partial N$. If we assume that the external potential V_{ext} is independent of time, then substitution reduces the Gross-Pitaevskii equation to

$$\left[-\frac{\hbar^2}{2m}\nabla^2 + V_{\text{ext}}(\boldsymbol{r}) - \mu + g|\Psi_0(\boldsymbol{r})|^2 \right] \Psi_0(\boldsymbol{r}) = 0. \tag{3.2}$$

Note that the chemical potential μ is set by the normalization of the order parameter $N = \int d\boldsymbol{r}\ |\Psi_0(\boldsymbol{r})|^2$. In seeking solutions for Ψ_0 we will see that the Gross-Pitaevskii equation can support several different types of solitons.

If the atomic interactions are attractive, that is when $a, g < 0$, then Eq. (3.2) admits solitonic solutions known as *bright solitons*, which are characterized as a localized density maxima in the condensate, i.e. a non-dispersive matter wavepacket. These solutions are given by the wavefunction,

$$\Psi_0(z) = \Psi_0(0)\frac{1}{\cosh(z/\sqrt{2}\gamma)}, \tag{3.3}$$

which can be easily checked by substitution into Eq. (3.2), where $\gamma = \hbar/\sqrt{2m|g|n_0}$ and $n_0 = |\Psi_0(0)|^2$ is the peak density. Note that the solution corresponds to a negative chemical potential, $\mu = -\frac{1}{2}|g|n_0$. Bright solitons form when the inherent tendency of a wavepacket to disperse is exactly balanced by the attractive atomic interactions, and they represent the ground state of the system. One example of a bright soliton can be seen in Fig. 3.1.

Bright solitons have been realized in cold atom systems for a wide range of experiments. In 3D, bright solitons are often unstable, however in tightly confined 1D systems, the mechanism of destabilization can be reduced. Bright solitons have been created in 1D attractive condensates composed of ^{7}Li atoms both singly [26] and in trains [27]. An exception to the instability of bright solitons in 3D trap geometries, has been observed during the collapse of attractive Bose-Einstein condensates composed of ^{85}Rb [51]. In this experiment, 3D bright solitons emerged from the violent collapse created by the sudden transition from repulsive to attractive interactions. Such 3D bright solitons were stable when the interatomic interactions were smaller than a critical value.

While the general consensus on the mathematical definition of a soliton varies with context, strictly speaking, solitons are considered to be localized solutions of a continuous integrable partial differential equation. When working with the DNLS,

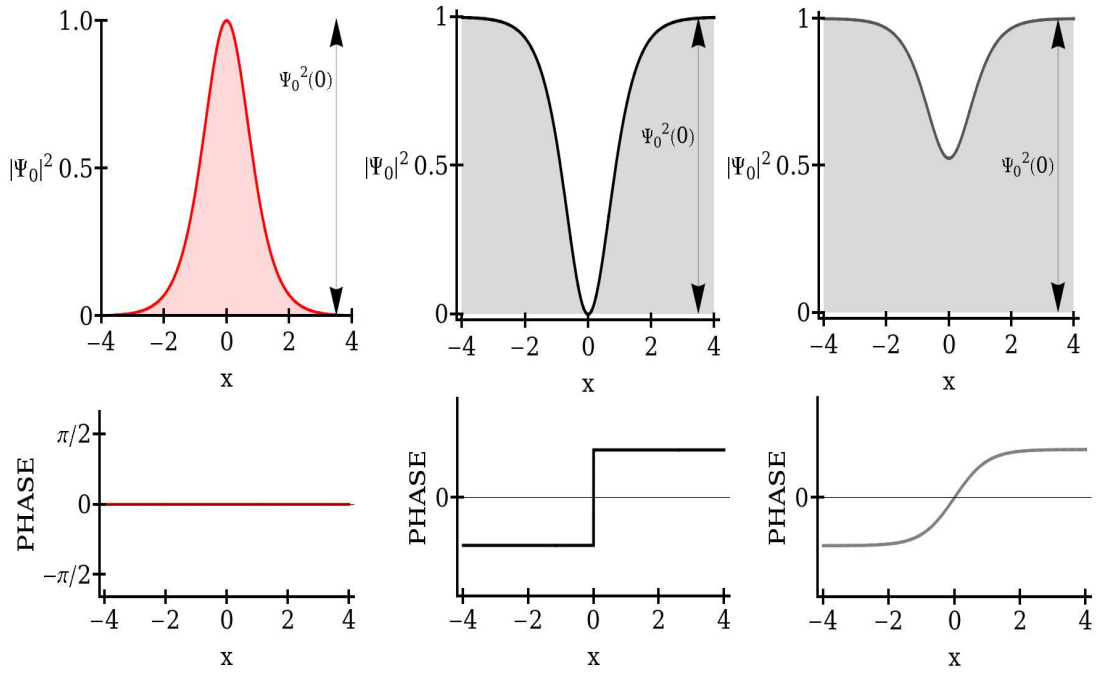

Figure 3.1: *Bright, Black, and Gray Solitons.* Three types of solitons, bright (left), black (middle), and gray (right) and their associated phase.

or later, when we consider the full quantum many-body theory to create solitons, the imposed discretization may break the integrability of the system. Regardless, we consider such solutions as quantum analogs of solitons in BECs.

3.2 Dark and Gray Solitons

When atomic interactions are repulsive, that is, when $a, g > 0$, then Eq. (3.2) admits stationary solutions which correspond to a localized density notch in the condensate, as shown in Fig. 3.1. Such objects are known as *dark solitons*, and have several characteristic properties. First, dark solitons have a discontinuous phase jump of π across the density notch. A dark soliton's width is proportional to the healing length of the condensate, ξ, and increases as the velocity of the soliton approaches the speed of sound in the condensate, $c_s = \sqrt{n_0 g/2m}$, where n_0 is the peak density of the condensate. Finally, unlike bright solitons, dark solitons are excited states, having energies greater than the underlying ground state of the BEC. In the mean field limit,

dark solitons are well-described by Eq. (2.7), provided that quantum depletion out of the condensed mode is negligible.

Experimentally, dark solitons were first realized in repulsive ^{87}Rb condensates in a few pioneering experiments [52] and [53], which sparked a sudden intense interest in nonlinear waves in BECs. Later, in repulsive ^{87}Rb condensates confined to a periodic potential, gap solitons were observed by specifying a preferable anomalous dispersion [54].

The particle-like nature of both bright and dark solitons was revealed by looking at soliton oscillations [55]. In addition, mean field calculations have predicted that solitons participate in undamped oscillations, comparable to those of a single particle.

In weakly interacting systems, quantum fluctuations can be calculated with the Bogoliubov–de Gennes equations, as in reference [56], where the authors demonstrated that quantum depletion accounts for much less than 1% of the system's ground state.

While BEC soliton experiments are typically performed in regimes where quantum fluctuations are small, soliton instabilities are known to be caused by dynamical, thermodynamical and collisional effects. In the strongly interacting limit, finite temperature and quantum fluctuations are known to affect the stability of dark solitons, causing them to fill in. When a dark soliton's density notch becomes partially filled in, as shown in Fig. 3.1, it is called a *gray soliton*.

Though solitons can be disturbed by quantum fluctuations, in the right parameter regimes they are still surprisingly robust to external perturbations, and are well-described by mean field theory. One of the aims of this thesis is to quantitatively determine the regimes in which mean field theory gives an accurate description of the system and the regimes in which it does not.

3.3 Macroscopic Quantum Tunneling and Semiclassical Treatments

Macroscopic quantum tunneling is the tunneling of a many-body wavefunction through a potential barrier. Recent studies of MQT in Bose-Einstein condensates have

been conducted in cold atom Josephson rings [6] and tilted two-well potentials [10], among others. Our interest is the MQT of bright solitons under a classically impassible rectangular potential barrier. Using mean field theory as an initial exploration of this problem, in Chapter 4 we will numerically evolve the DNLS to obtain real time dynamics of bright solitons in BECs. Ultimately, in Chapter 7, a full quantum many-body approach will be undertaken. Beforehand, in this section, it is appropriate to describe a couple semiclassical methods that are often used for calculating tunneling rates: the JWKB approximation and the instanton method.

3.3.1 JWKB Approximation

The Jeffreys-Wentzel-Kramers-Brillouin (JWKB) approximation, named after the physicists who developed it in the 1920's, is a commonly used semiclassical method for calculating tunneling rates of a quantum mechanical particle through a barrier. In 1926 G. Wentzel [57], H. A. Kramers [58] and L. Brillouin [59] all applied the method to the Schrödinger equation. However, three years prior, H. Jeffreys, who is often neglected credit, first developed the method in a mathematical context [60].

When the JWKB approximation is applied to the Schrödinger equation for a single particle, the wavefunction is assumed to be an exponential function, whose amplitude and phase vary slowly in comparison to the de Broglie wavelength, and then expanded semiclassically. Note that any external potentials, if present, must also vary slowly as compared to the de Broglie wavelength, because the wavevector of a plane wave solution to the Schrödinger depends on the external potentials. The wavefunction is expanded semiclassically, in powers of $\hbar$, neglecting terms of $\hbar^2$ and higher. It is in this sense that we say the JWKB approximation effectively replaces the Schrödinger equation with it's semiclassical limit. The JWKB approximation breaks down at classical turning points, where the energy of the system approaches the strength of the external potentials. In these cases, connection formulae can be applied on either side of the classical turning point to tie the two regions together [61].

The JWKB approximation has many practical limitations when solving quan-

tum many-body problems. First, like any other semiclassical or mean field method, it neglects quantum many-body effects, such as quantum fluctuations. Second, by definition, the JWKB approximation can only be applied to a single wavefunction. If a mean field perspective is assumed, then the JWKB approximation can be applied to the order parameter, allowing one to calculate the rate at which the mean field of the condensate tunnels under a potential barrier. This method of approach has been done before, for example, the tunneling of solitons in BECs has been calculated using the JWKB approximation and variational techniques in reference [62], where the authors found that MQT occurs on time scales of 10 ms to 10 s. Third, the JWKB approximation can only be used to calculate specific parameters, such as the tunneling rate of the mean field, or the lifetime of the condensate. In this thesis, rather than using the JWKB approximation to calculate properties of the mean field, we numerically evolve the DNLS to obtain explicit real time dynamics of the order parameter.

3.3.2 Instanton Methods

Instanton methods are another means by which to calculate the transition probability of a quantum mechanical particle to tunnel through a potential barrier. Instanton methods can be used to describe MQT through a semiclassical approximation akin to the JWKB approximation, but within the path integral formalism of quantum mechanics [63]. By semiclassical approximation, we mean that path integral variables are expanded about the classical solutions of the problem of interest. The term "instanton" arises from the interpretation of certain solutions of the classical equations of motion in imaginary time, which have the form of an instantaneous kink that makes a large contribution to the action [63].

The instanton method can be used to calculate MQT in simple cases, such as for the quantum rotor model, a double well, or a 1D ring lattice, but becomes quite complicated as the number of degrees of freedom in the system increases. For the MQT of BECs, we draw specific attention to the work of Ippei Danshita and Anatoli

Pokolnikov in reference [64], who use the instanton method to study the tunneling of boson supercurrents in a 1D ring lattice. In reference [64] the authors compare instanton methods to exact time-evolving block decimation simulations, the same quantum many-body method implemented in this thesis. In addition, Ueda *et al.* applied the instanton method to the Gross-Pitaevskii energy functional to show that MQT can be a dominant mechanism for the decay of a condensate with attractive interactions [7].

Experimentally, solitons in BECs are comprised of many particles and lattice sites, so applying the instanton method to the problem presented in this thesis would be an extremely complicated task. Also, instanton methods are rendered inaccurate for larger interaction strengths [64], whereas our quantum many body method time-evolving block decimation, described in Chapter 7, suffers from no such limitations. Like the JWKB approximation, the instanton method would not be able to provide a calculation of the real time dynamics, so for our mean field study we instead elect to numerically simulate the DNLS. If implemented, the instanton method could be used as another independent comparison to our calculation of tunneling rates with the DNLS, presented in Chapter 4, and with time-evolving block decimation.

3.4 Solitons and Macroscopic Quantum Tunneling: Applications

In regards to technological applications, what are the possible advantages of working with matter-wave solitons in BECs, versus individual particles such as photons or atoms? Solitons in BECs are macroscopic phenomena that behave entirely different in regard to measurements, acting similarly to atomic ensembles. In addition, BECs possess unique coherence properties which have led to many proposed applications including atom optics and atom interferometry. Matter-wave solitons in BECs are coherent spatially localized phenomena, and are unique for their non-dispersive properties. As a motivation for the study of MQT of solitons in BECs, in this section we outline several promising applications.

3.4.1 The Atomic Soliton Laser

Coherent matter-waves in Bose-Einstein condensates are analogous to coherent waves of light. Experimentally, it is well-known that a BEC can release an intense coherent beam of matter when it is outcoupled from the magneto-optical trap. Such an "atom laser," as it is now known, has been demonstrated in several experiments using repulsive condensates [65, 66, 67]. Solitons are of great interest, because they would allow for the free propagation of a virtually non-divergent atom laser.

In attractive condensates, it has been shown both numerically and analytically that an axially confined BEC can be made into a pulsed atomic soliton laser [68]. One method for achieving this is to take an initially repulsive BEC and tune the scattering length to be small and negative via a magnetically induced Feshbach resonance, meanwhile, changing the axial potential from attractive to repulsive. The sudden change makes the condensate modulationally unstable, and by the self-interference of the order parameter, solitons begin to form from the center of the BEC outward. One thus produces a "soliton train of non-phase-locked self-coherent pulses" that is analogous to the output of a light-wave laser [68].

Atom lasers are one of the applications which would greatly benefit from a better understanding of quantum many-body effects and MQT. MQT, for example, is one of the fundamental principles in the atom laser experiments performed in references [65, 66, 67], and in other systems involving optical lattices.

3.4.2 Atom Interferometry

Because BECs have a macroscopic coherence length [69] and offer the experimentalist a nearly unprecedented level of control over the amplitude and phase of the condensate, they have long been considered the most ideal media in which to study matter-wave interferometry. Many schemes for atom interferometers have been suggested in the last ten years, for example Bloch oscillation interferometers and bright soliton interferometers [66, 70, 71]. The performance of atomic interferometers in

BECs is crucially hindered by particle-particle interactions, which add phase shifts and decoherence into the system [71]. [1] Interactions and many-body effects are the primary reason why, so far, the above implementations have failed, and are one of the motivating factors for the study in this thesis.

In addition, the demonstration of spatially ultra-narrow solitons in lithium BECs [27, 26] has led to other proposed applications for frequency stabilization [72]. There are many other proposals for atom interferometry experiments with BECs, but perhaps the strongest motivating factor lies in the promising applications they have in making precision measurements.

3.4.3 Precision Measurement With Solitons

Since BECs are highly sensitive to outside factors, they are ideal candidates for probing and measuring various physical quantities with extremely high precision, such as, acceleration, angular rotation, gravitational fields, and electromagnetic fields.

Using a soliton interferometer, generated by the overlapping of two bright solitons which are accelerated toward one another, for example, in a parabolic external magnetic field, as discussed in reference [73], can be used to make precise measurements of a magnetic field gradient to orders of 10^{-2}pT/cm.

A soliton interferometer can also be used to make accurate measurements of angular rotation. Configured in a magnetic waveguide ring, solitons can be accelerated by gravity and collide at the lower point of the ring. This creates an interference pattern and allowing for precise measurements of the angular rotation [73].

[1] Decoherence and many other quantum many-body phenomena will be discussed in Chapter 5.

Chapter 4

MEAN FIELD SIMULATIONS OF MANY-BODY TUNNELING

4.1 Mean Field Numerical Methods

In this chapter, we discuss the numerical methods used to generate mean field simulations of macroscopic quantum tunneling of bright solitons in Bose-Einstein condensates. Mean field theory serves as a useful first attempt to obtain a rough, yet physically intuitive idea of the dynamics of MQT, without the burden of heavy numerical computation. Dynamics are thus obtained via numerical simulation of the discrete nonlinear Schrödinger equation, previously discussed in Eq. (2.38). The DNLS can be broken into a coupled set of ordinary differential equations which can be solved with finite difference methods, in particular, the fourth-order Runge-Kutta method, and the pseudo-spectral method, both of which are discussed here.

In assuming a mean field perspective, for now we are sidestepping the more challenging aspects inherent to a full quantum many-body description of MQT, which we will return to in Chapter 5. The quantum many-body escape problem has already been studied in the context of mean field theory, where it has been found to have quite different features from single-particle quantum tunneling, including a tunneling time which is not simply the inverse of the JWKB tunneling rate [62]. The tunneling rate is dependent on the number of particles remaining behind the barrier, and as such, the decay time must be calculated by an integral over each time step. Furthermore, it has been shown that a non-smooth dynamical behavior referred to as "blips," in which particles escape through the barrier in bursts, can be found via mean field theory [74].

Mean field simulations are valuable in that they provide a useful comparison to our later exact quantum many-body simulations. Once we analyze the full quantum

many-body simulations in Chapter 7, we can return to the findings of this chapter and quantitatively answer the question: how accurately does mean field theory describe MQT? Consequently, we will then reveal the regimes in which mean field is inadequate, and illustrate the necessity for a full quantum many-body description.

4.1.1 Discrete Nonlinear Schrödinger Equation in Matrix-Vector Form

The 1D DNLS equation can be solved by replacing the partial differential equation in Eq. (2.38) with a coupled set of ordinary differential equations, in what is commonly known as the *method of lines*. In this method we discretize the spatial components and leave time continuous, allowing us to recast the problem in matrix-vector form as,

$$i\hbar\frac{\partial\vec{\psi}(t)}{\partial t} = H[\vec{\psi}(t),t]\vec{\psi}(t), \tag{4.1}$$

where $\vec{\psi}(t)$ is an L-dimensional vector with elements, $[\vec{\psi}(t)]_k \equiv \vec{\psi}_k(t)$. The Hamiltonian, $H[\vec{\psi}(t),t]$, is an $L\times L$ matrix of the form,

$$H = \begin{pmatrix} U|\psi_1|^2+\epsilon_1 & -J & 0 & \dots & 0 \\ -J & U|\psi_2|^2+\epsilon_2 & -J & \vdots & \dots \\ 0 & -J & \ddots & \ddots & 0 \\ \vdots & \ddots & \ddots & \ddots & -J \\ 0 & \dots & 0 & -J & U|\psi_L|^2+\epsilon_L \end{pmatrix}. \tag{4.2}$$

Box boundary conditions are imposed on the system such that, $\psi_0 = \psi_{L+1} \equiv 0$. By recasting the problem into matrix-vector form, the coupled set of ordinary differential equations in Eq. (4.1) can be easily propagated forward in time using finite difference methods, such as Crank-Nicholson, Runge-Kutta or pseudo-spectral methods.

4.1.2 Runge-Kutta

The Runge-Kutta method for numerically integrating ordinary differential equations may be readily applied to Eq. (4.1). The general idea of the scheme is to advance

the solution from $\vec{\psi}(t)$ to $\vec{\psi}(t+\delta t)$ by taking a series of trial steps within a given time interval in order to cancel out the lower order error terms [75]. In the fourth-order Runge-Kutta method the wavefunction is propagated forward in time according to the approximation

$$\vec{\psi}(t+\delta t) = \vec{\psi}(t) + \frac{\delta t}{6}\left[\vec{k}_1(t) + 2\vec{k}_2(t) + 2\vec{k}_3(t) + \vec{k}_4(t)\right] + O(\delta t^5), \tag{4.3}$$

where,

$$\begin{aligned}
\vec{k}_1(t) &= H[\vec{\psi}(t), t]\vec{\psi}(t)/i\hbar, \\
\vec{k}_2(t) &= H[\vec{\psi}(t), t]\{\vec{\psi}(t) + \frac{\delta t}{2}\vec{k}_1(t)\}/i\hbar, \\
\vec{k}_3(t) &= H[\vec{\psi}(t), t]\{\vec{\psi}(t) + \frac{\delta t}{2}\vec{k}_2(t)\}/i\hbar, \\
\vec{k}_4(t) &= H[\vec{\psi}(t), t]\{\vec{\psi}(t) + \delta t\vec{k}_3(t)\}/i\hbar.
\end{aligned} \tag{4.4}$$

When using the fourth-order Runge-Kutta method, time steps of $\delta t = 0.001\hbar/J$, are used to obtain converged results.

4.1.3 Pseudo-Spectral Methods

An equation of the form

$$i\hbar\frac{\partial\vec{\psi}(r,t)}{\partial t} = H[\vec{\psi}(r,t), t]\vec{\psi}(r,t), \tag{4.5}$$

resembles the linear ordinary differential equation, $\alpha f(t) = \frac{d}{dt}f(t)$ with $\alpha = H/i\hbar$ and $f(t) = \psi(r,t)$. Using the theory of linear operators, the general solution to the Schrödinger equation is

$$\psi(r,t) = e^{-iHt/\hbar}\psi(r,0), \tag{4.6}$$

where the exponentiation of operators is defined in the usual way through a power series. The Hamiltonian is separated into a kinetic term and a potential term such

that, $H = T + V$, where $T = p^2/2m = -\hbar^2\nabla^2/2m$. If the potential term depends only on position, $V = V(r)$, and we can write the solution in configuration space as

$$\psi(r,t) = e^{-i(T+V(r))t/\hbar}\psi(r,0). \tag{4.7}$$

To good approximation for small values of t, we can use a symmetric decomposition to express the solution as

$$\psi(r,t) \approx e^{-iV(r)t/2\hbar}e^{-iTt/\hbar}e^{-iV(r)t/2\hbar}\psi(r,0). \tag{4.8}$$

The pseudo-spectral method is to iteratively propagate the expression above in time, that is, for a given $\psi(r,t)$, we find $\psi(r,t+\Delta t)$ using small time steps Δt obtain the solution at any arbitrary value of t. In 1D, this process begins by calculating intermediate values starting from the rightmost operator,

$$\begin{aligned}\psi(r,t+\Delta t) &\approx e^{-iV(r)\Delta t/2\hbar}e^{-iT\Delta t/\hbar}e^{-iV(r)\Delta t/2\hbar}\psi(r,t)\\ &= e^{-iV(r)\Delta t/2\hbar}e^{-iT\Delta t/\hbar}\phi_1(r,t)\\ &= e^{-iV(r)\Delta t/2\hbar}\phi_2(r,t),\end{aligned} \tag{4.9}$$

where,

$$\phi_1(r,t) = e^{-iV(r)\Delta t/2\hbar}\psi(r,t), \tag{4.10}$$

$$\phi_2(r,t) = e^{-iT\Delta t/\hbar}\phi_1(r,t). \tag{4.11}$$

Notice that applying the middle operator, ϕ_2, is an infeasible calculation in configuration space. However, in momentum space the calculation is simplified greatly. Thus we write the expansion in momentum space using the Fourier transform, denoted by $\mathcal{F}$, where, $\Phi_1(k) = \mathcal{F}[\phi_1(r,t)]$ and $\Phi_2(k) = e^{-i\hbar k^2\Delta t/2m}\Phi_1(k)$, which requires only pointwise multiplication. This is very convenient numerically, because we can employ fast Fourier transform techniques. Therefore the pseudo-spectral method is

summarized as,

$$\psi(r,t+\Delta t) \approx e^{-iV(r)\Delta t/2\hbar}\mathcal{F}^{-1}\left[e^{-i\hbar k^2\Delta t/2m}\mathcal{F}\left[e^{-iV(r)\Delta t/2\hbar}\psi(r,t)\right]\right]. \tag{4.12}$$

There are many efficient and accurate fast Fourier transform packages that are freely available. In this thesis, we use the pseudo-spectral method to simulate the DNLS equation.

4.2 Imaginary Time Propagation

We often wish to start from the system's ground state, which may be complicated or unknown, and evolve it forward in time. An easy, reliable method for obtaining the ground state of a particular Hamiltonian, when the ground state is unknown, is *imaginary time propagation*. Imaginary time is a mathematical trick to convert an arbitrary starting state into a ground state without assuming details about its functional form. This is achieved by taking $\tau \equiv it$ and evolving with respect to τ, using either the Runge-Kutta or pseudo-spectral method. Under imaginary time, a Schrödinger-type equation cleverly becomes a diffusion equation in which the highest energy eigenstates decay most quickly. After sufficient propagation in imaginary time, the system converges to its ground state.[1] For the imaginary time method to work properly, one must choose an initial state in which all Fourier components have a nonzero weight, otherwise the ground state obtained from imaginary time propagation could be biased. For finding bright solitons, a Gaussian initial state is a convenient choice because it weights all Fourier components and closely resembles the sech^2 function of the bright soliton, thus reducing the amount of imaginary time necessary to achieve the ground state. The number of steps in imaginary time required to reach the ground state can be determined by convergence criteria, satisfied when the difference between two states in imaginary time is a minimum value. Throughout our

[1] Imaginary time propagation can also be used to find long-lived metastable states.

mean field simulations we use imaginary time steps of $\Delta t = 0.001\hbar/J$ for converged results.

4.3 Bright Solitons: Mean Field Simulations

In this section we demonstrate that the fundamental bright soliton solution, discussed in Chapter 3, may be obtained by evolving the DNLS in imaginary time using the pseudo-spectral method, as described Eq. (4.12). To achieve bright solitons, we work with attractive condensates, with $U \leq 0$, and a negative chemical potential, $\mu \leq 0$. For a system of N bosons loaded into a 1D optical lattice of L sites and box boundary conditions, the DNLS takes the form

$$i\hbar\frac{\partial\phi_k}{\partial t} = -J(\phi_{k+1} + \phi_{k-1}) + U|\phi_k|^2\phi_k + \mu\phi_k. \tag{4.13}$$

Before imaginary time propagation, the system is initialized as a Gaussian shaped number density, centered at the midpoint of the lattice. Propagation in imaginary time causes the Gaussian profile to quickly converge to a bright soliton, as shown in Fig. 4.1, where the number density on each lattice site is plotted over time. The bright soliton obtained from imaginary time is then used as the initial condition for real time propagation. The real time dynamics of the fundamental bright soliton are shown in Fig. 4.1, where the bright soliton preserves its shape over time.

4.4 Confining Solitons With External Potential Barriers

Using a rectangular external potential barrier V_{ext}, a bright soliton can be confined between the barrier and one of the box boundary walls of the system. If a rectangular potential barrier term, V_{ext}, is inserted into the DNLS it takes the form

$$i\hbar\frac{\partial\phi_k}{\partial t} = -J(\phi_{k+1} + \phi_{k-1}) + U|\phi_k|^2\phi_k + \mu\phi_k + V_{\text{ext},k}\phi_k. \tag{4.14}$$

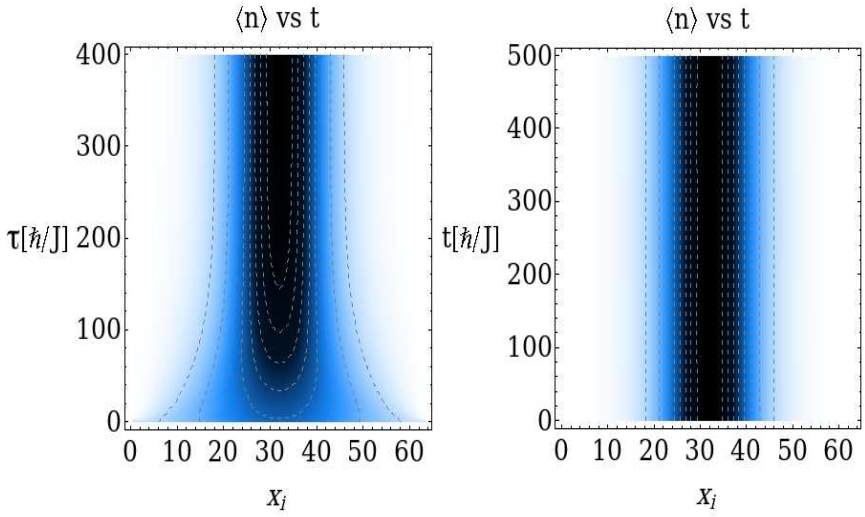

Figure 4.1: *Imaginary and Real Time Propagation.* A bright soliton is formed from an initial Gaussian profile in imaginary time (left), and is then propagated in real time (right) and shown to preserve its shape. This simulation shows the case for $NU/J = -0.5$ over $L = 64$ sites.

Like other potentials in optical lattice systems, as discussed in Section 2.3, rectangular potential barriers are easily realized experimentally. Before imaginary time

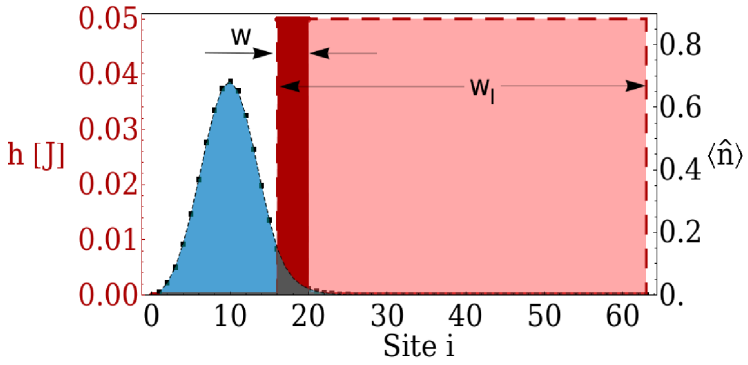

Figure 4.2: *Initial State.* Bright soliton formed by relaxation in imaginary time with a barrier of height h and initial width w_I (dashed line). Before real time propagation the barrier is reduced to width w (solid red line) so the soliton can commence macroscopic quantum tunneling. This plot shows a system with: $N = 6$, $L = 64$, $J = 1$, $U = -0.05$, $\mu = -1$.

propagation, we set V_{ext} to a height, $h = 0.05$, and a width, w_I, effectively reducing the system size as shown in Fig. 4.2. We initialize the many-body wavefunction as a Gaussian profile, centered in the middle of the potential well created by V_{ext}, and

then use imaginary time relaxation form a bright soliton behind the potential barrier. One example of a bright soliton state after imaginary time propagation is shown in Fig. 4.2. Notice that a small portion of the soliton tail extends under the barrier due to its finite height.

At $t = 0$, in real time, the barrier is decreased to width w, typically one to five sites, such that the soliton can escape confinement on a reasonable time scale. By reasonable, we mean on a time scale within the window of the given simulation and less than the time in which reflections return to the barrier from the far box boundary. Attractive interactions $U < 0 < h$ ensure that tunneling is always quantum, not classical. Note that the barrier height must remain constant when transitioning between imaginary time and real time, otherwise, in real time the soliton will oscillate within the potential well.

The soliton escapes from behind the barrier on a timescale which increases with w. A characteristic *escape time*, $t_{\rm esc}$, is quantified by the time at which the number density remaining behind the barrier falls to $1/e$ of its initial value. We choose L large enough so that reflections from the box boundary at the far right do not return to the barrier in times $t < t_{\rm esc}$. Evolving in real time, we first make a coarse observation of the dynamics of MQT in Fig. 4.3 by plotting the average particle number in different regions, in order to determine $t_{\rm esc}$.

For fixed NU/J, w, and h, the DNLS gives the same result independent of N and U, i.e N and U may change, provided NU/J remains constant. We denote the 1/e mean field escape time as $t_{\rm esc}^{\rm MF}$. In Fig. 4.4 we show the exponential dependence of the escape time on the barrier area and the interatomic interactions, U, for fixed L and J. In Chapter 7 we will show the stark contrast between this mean field data and the full quantum many-body simulations using time-evolving block decimation.

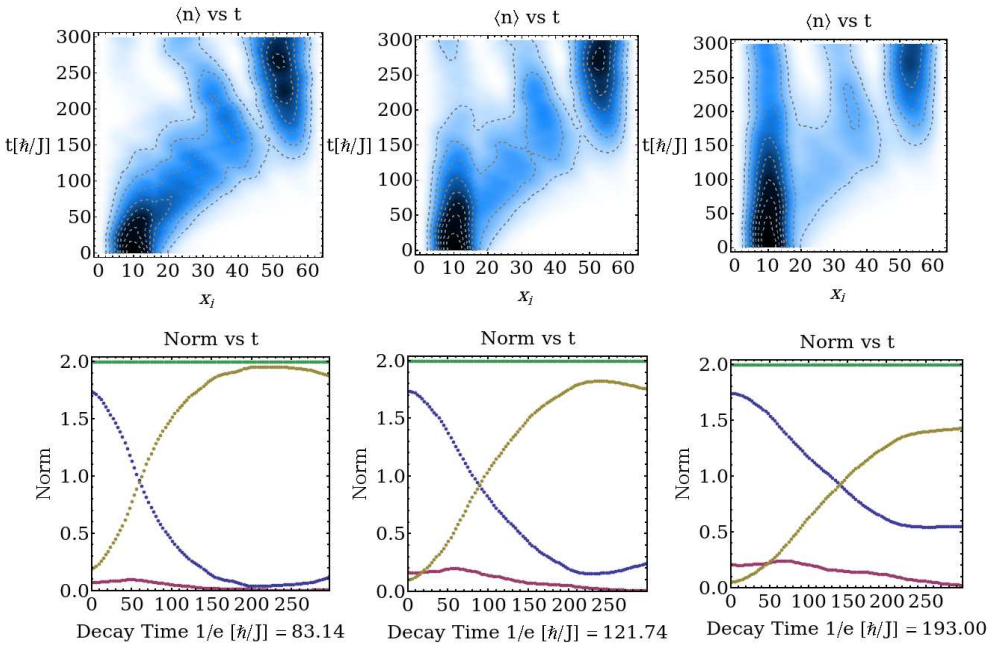

Figure 4.3: *Macroscopic Quantum Tunneling of a Mean Field Bright Soliton With Weak Interactions.* A bright soliton tunnels under a barrier in real time. The barrier begins at site 16 with a thickness of 1 (left), 3 (middle), and 5 (right) sites. In the lower panels the decay time is calculated to be the time when the norm inside the barrier drops to 1/e of its initial value. This simulation shows the case for $NU/J = -0.01$ over $L = 64$ sites.

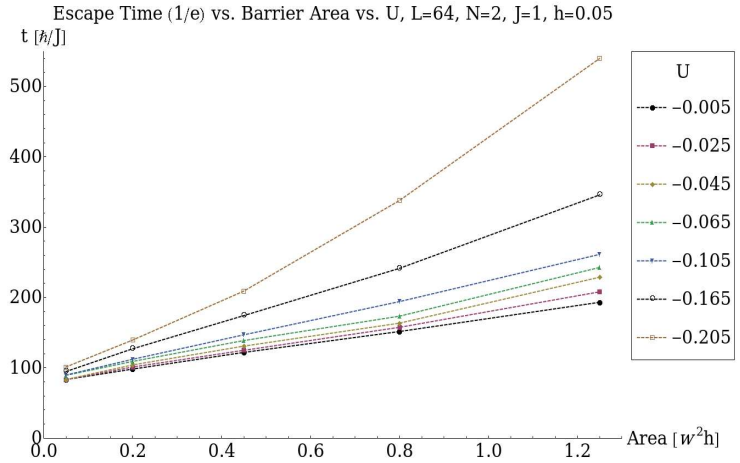

Figure 4.4: *Effect of the Strength of the Interatomic Interactions on the Soliton Escape Time.* This simulation shows the case for $NU/J = -0.01$ over $L = 64$ sites.

Chapter 5

QUANTUM ASPECTS OF SOLITONS IN BOSE-EINSTEIN CONDENSATES

In BECs, solitons are manifestations of entangled many-body quantum mechanics over macroscopic length scales. The mean field theory of the previous two chapters offered a simplified perspective by tacitly avoiding several troublesome, yet critical features which can drastically affect the condensate, and thus the behavior of solitons within it.

An ideal BEC is one in which all the particles occupy the same single particle state, $\chi_0(\boldsymbol{r})$. So far, atomic BEC has made great strides towards this ideal experimentally, however, it is important to keep in mind the imperfections in such systems. As discussed in discussed in Section 2.1, three-body and other losses, such as those due to collisions with the background gas in vaccuum, significantly restrict the lifetime of a condensate. *Quantum depletion*, arising from particle-particle interactions, and *thermal depletion*, arising from thermal fluctuations, both cause atoms to become depleted from $\chi_0(\boldsymbol{r})$ [56]. Additionally, quantum entanglement, nonlocal correlations induced by the interactions between particles, contribute to the behavior of solitons in BECs. These type of quantum and many-body effects, not captured in mean field theory, have proved to significantly alter the dynamics and the lifetime of solitons in BECs [76, 77].

5.1 Quantum and Thermal Depletion

Quantum depletion is a measure of the occupation of noncondensate modes in the system. Depletion from the condensate mode is defined to be

$$D \equiv 1 - N_0/N_{\text{avg}}, \tag{5.1}$$

where N_0 is the occupation of condensate wavefunction and $N_{\text{avg}} \equiv \sum_{k-1}^{L} \langle \hat{n}_k \rangle$ is the average number. For typical ground state BEC experiments performed in harmonic traps the quantum depletion is usually on the order of 0.01 to 0.001 percent [31]. However, when working with excited states, such as solitons, and in optical lattice geometries, quantum depletion is no longer negligible.

Bright matter wave solitons have been observed during the collapse of attractive Bose-Einstein condensates composed of ^{85}Rb in a 3D trap geometry [51]. The instability causing quantum dark solitons to fill in has been shown to be caused by quantum fluctuations and particle-particle scattering, which deplete particles out of the condensate wavefunction and into modes having non-zero density on sites near the center of the soliton [76]. Mishmash *et al.* have successfully simulated dark solitons with TEBD, the numerical algorithm we employ in this thesis [76, 77], demonstrating how not only mean field theory, but also how the Bogoliubov de Gennes theory breaks down. They have shown that dark solitons will decay, even at zero-temperature, and have demonstrated that dark solitons under these conditions still participate in inelastic collisions.

Dziamarga *et al.* have shown that solitons will delocalize, but will not fill in for particular quantum realizations, even at zero temperature. The many-body character of quantum depletion is one of the motivating factors for us to utilize TEBD for our study of the macroscopic quantum tunneling of bright solitons in BECs. Additionally, many previous studies of matter-wave solitons have focused on classical and mean field methods, while only a few have used quantum many-body treatments.

Although in this thesis we are working under the assumption of zero temperature, it is worthwhile to make note of the effects of thermal fluctuations on solitons in BECs, because, especially for experimentalists, it is a vital contributor to depletion of the condensate. Finite temperature studies, performed in generalized mean field models, have shown that solitons will rapidly decay near the edge of the condensate [53, 78]. In addition, at lower temperatures, experimental results have shown

that the trajectory of solitons can follow an oscillatory pattern [55, 79, 80], which was previously predicted theoretically [81]. In addition, the dynamics of dark solitons in BECs at finite temperature has been studied using the stochastic Gross-Pitaevskii equation, which reveal spreading in individual soliton trajectories, that should be observable in experimental systems [82]. Additionally, Dziarmaga *et al.* have shown the effects of heating by atomic losses in BECs [56].

5.2 Quantum Entanglement

Quantum entanglement is a purely quantum mechanical nonlocal correlation between two or more quantum systems.[1] A general introduction to the topic can be found in Nielsen and Chuang [83]. The concept of nonlocality led A. Einstein to question the completeness of quantum theory, and in 1935, A. Einstein, B. Podolsky, and N. Rosen [84] formulated their now famous EPR paradox, a gedanken experiment which argued for the possibility of hidden variables not yet discovered in quantum theory. The paradox prevailed until 1964, when J. Bell introduced a set of inequalities allowing one to experimentally test for the possibility of hidden variables [85]. Subsequent experimental results, in 1972 by S. Freedman and J. Clauser, showed violations of Bell's inequalities, thus supporting the validity of nonlocality and quantum entanglement [86]. The importance of quantum entanglement was noticed and defended by E. Schrödinger when he said [87],

> "[Entanglement] is not one but rather the characteristic trait of quantum mechanics, the one that enforces its entire departure from classical lines of thought."

In BEC, emergent phenomena like solitons appear when many interacting particles are brought together. The interactions induce quantum entanglement in the system, and thus the interplay between interactions and quantum entanglement are crucial

[1] Note that while quantum entanglement is a nonlocal effect, it is generated by local interactions within the system.

to determining the emergent behavior of the system.

It has been shown that solitons may become entangled as a result of colliding with one another. Collision-induced entanglement between fast moving matter-wave solitons has been studied in BECs with attractive interactions using the Born approximation. As such, this study was limited to being only a first approximation in perturbation theory [88]. The author's suggest that Bell's inequalities could possibly be tested on the entangled solitons to determine measurements over different macroscopic length scales or level of errors than previously tested.

5.2.1 Pure States and Entanglement

Many-body quantum entanglement is still an open problem in quantum mechanics. A general consensus still needs to be reached on how to properly quantify multipartite entanglement, however the procedure, given by the von Neumann entropy, is well-understood for bipartite systems. Depending on whether the system of interest is in either a pure or a mixed state, bipartite entanglement is calculated differently. In this and the following section we endeavor to explain that difference.

A system consisting of two subsystems A and B is said to be in a *pure state* if it is represented by the products,

$$|\psi\rangle = \sum_{jk} a_{jk} |\epsilon_j\rangle_A |\epsilon_k\rangle_B. \tag{5.2}$$

Unentangled pure states, also known as *product states*, can be identified if the state is decomposed such that,

$$|\psi\rangle = |\phi_A\rangle_A |\phi_B\rangle_B. \tag{5.3}$$

Product states do not violate any of Bell's inequalities, however, entangled pure states have been shown to violate them in certain circumstances. The Schmidt decomposition, a central idea to TEBD, discussed at length in the following chapter, can be used to see if an arbitrary state can be decomposed into a product state.

For pure states the (bipartite) entanglement of the system is quantified by the von Neumann entropy (the entropy of entanglement),

$$S(\rho_i) = -\mathrm{Tr}[\rho_i \log_2 \rho_i], \tag{5.4}$$

where ρ_i stands for the reduced density matrix of system A or B and Tr denotes the trace. In fact, it easily shown that $\rho_A = \rho_B$.

5.2.2 Particle and Spatial Entanglement

In mean field theory, particle entanglement is overlooked because of the assumption that each particle occupies the same single particle wavefunction, given by the order parameter. From this viewpoint each individual particle is a pure state, and thus the entanglement between it and every other particle in the system is zero. In the full quantum many-body problem, we take into account that there is, in general, a nonzero amount of entanglement between a given particle and each of the other $N-1$ particles in the system, which we refer to as *particle entanglement*. In addition to entanglement between particles, we can have entanglement between the system's individual Wannier modes. In general, entanglement between modes can be thought of as entanglement between one Wannier mode of the system with each of the other $L-1$ spatially distinct Wannier modes. We refer to this kind of entanglement as *spatial entanglement* [76]. We define the single-particle von Neumann entropy to be

$$S_{\mathrm{vN,particles}} \equiv -\mathrm{Tr}\left[\frac{\hat{\rho}^{(1)}}{N} \log_L \left(\frac{\hat{\rho}^{(1)}}{N}\right)\right] \in [0,1], \tag{5.5}$$

where $\hat{\rho}^{(1)}$ is the single-particle density matrix and Tr denotes the trace. We have to divide by factors of N, in order to normalize the sum of eigenvalues to unity, because $\mathrm{Tr}(\hat{\rho}^{(1)}) = N$. The single-particle von Neumann entropy characterizes the global behavior of the system because all particles in the condensate are assumed to be indistinguishable.

Similarly for spatial entanglement we define a localized von Neumann entropy of the form

$$S_{\mathrm{vN,k}} \equiv -\mathrm{Tr}\left[\hat{\rho}_k \log_d\left(\hat{\rho}_k\right)\right] \in [0,1], \tag{5.6}$$

where k denotes each Wannier mode (equivalently, each site index). In Eq. (5.6), $\hat{\rho}_k$ is the reduced density matrix for a single lattice site k, given by the partial trace over all lattice sites except one.[2] The base d logarithim ensures that $S_{\mathrm{vN,k}} \leq 1$. In a mean field treatment the spatial entanglement between Wannier modes is completely neglected, and thus the local von Neumann entropy is a useful measure for quantifying deviations from semiclassical behavior.

The density matrix $\hat{\rho}$ can be used to determine the *purity* of a quantum state. The purity is defined as $\mathrm{Tr}\left(\hat{\rho}^2\right)$, and can be used to determine the mixedness of a given state. A pure state, for example, has density matrix elements of $\left(\hat{\rho}\right)_{ij} = \delta_{i,j}\delta_{i,0}$, while a maximally mixed state has density matrix elements of $\left(\hat{\rho}\right)_{ij} = \delta_{i,j}/d$, where d is the dimension of the system's Hilbert space. The purity of any given system will lie between the range $[1/d, 1]$. One usefull quantum measure is to define an *average local impurity* defined to be [76, 77],

$$Q_{\mathrm{modes}} \equiv \frac{d}{d-1}\left[1 - \frac{1}{L}\sum_{k=1}^{L}\mathrm{Tr}\left(\hat{\rho}_k^2\right)\right], \tag{5.7}$$

where $\hat{\rho}_k$ is the reduced density matrix for a single lattice site k, given by the partial trace over all lattice sites except one. Equation (5.7) has a factor of $d/(d-1)$ to scale Q_{modes} to be less than or equal to one. Thus, Q_{modes} is a value ranging from $[0,1]$ and is maximized when each site is maximally mixed and minimized when each site is in a pure state.

[2]Note that $\hat{\rho}_k$ is different than the single-particle density matrix, $\hat{\rho}^{(1)}$, the latter is a partial trace over all particles except one.

5.3 Decoherence

Studies in emergent quantum phenomena have spurred an increasing interest in decoherence– the mechanism by which a quantum system recovers classical behavior from a quantum system. When a quantum system interacts in a thermodynamically irreversible way with its environment, the two can become "entangled" such that the quantum coherence of the system is distributed over so many degrees of freedom that it is rendered unobservable. In this view, decoherence can be thought of as the loss of information from a system to its environment.[3] Decoherence theory has been complemented by experiments using matter waves coupled to external photons or molecules, and by investigations using coherent photon states, trapped ions and electron interferometers. Decoherence of matter-wave solitons can not only arise from quantum fluctuations in the spatial location or the phase of the soliton, but also due to the excitation of the many-body degrees of freedom of the condensate (like Bogoliubov de Gennes modes). Decoherence may explain why some macroscopic systems, such as matter-wave solitons, seem to possess classical properties.

[3]It may be more apt to say that decoherence is a disturbance (or change of state) of the environment by the system.

Chapter 6

QUANTUM MANY-BODY SIMULATIONS USING TIME-EVOLVING BLOCK DECIMATION

In this chapter, we provide a detailed description of the theoretical and computational aspects of time-evolving block decimation, an algorithm for simulating the 1D Bose Hubbard Hamiltonian, Eq. (2.26), which uses a Schmidt decomposition to truncate the Hilbert space. In the process, we will confront the challenges behind solving the quantum many-body problem and explain the methods for alleviating such difficulties.

6.1 Time-Dependent Calculations of Many-Body Systems

Efficient numerical simulation of quantum many-body systems is an ongoing challenge. A standard diagonalization of the BHH for large systems is computationally infeasible due to the exponential increase of the Hilbert space dimension with the number of particles and lattice sites. For a system of N particles and L sites the dimension of the Hilbert space is,

$$D(N, L) = \frac{(N + L - 1)!}{N!(L - 1)!}. \tag{6.1}$$

Even for the simple situation of a system, passing through a quantum phase transition in the thermodynamic limit, in which $L = N$, the difficulties of exact diagonalization become readily apparent: for $N = 8, 12, 16$ the dimension of the associated Hilbert space burgeons to $D(8, 8) = 6\,435$, $D(12, 12) = 1\,352\,078$, and $D(16, 16) = 300\,540\,195$. Using a computer with 1Gb of memory and adopting sparse-matrix methods, one may face problems for $N = L > 10$. In a more quantitative

sense, the observation that

$$\lim_{N \gg 1} \frac{D(N+1, N+1)}{D(N, N)} \approx 4, \tag{6.2}$$

shows the rapid growth of the Hilbert space with the system size. Experimental setups are typically comprised of particles and lattice sites numbering in the hundreds; thus, it is unlikely for standard diagonalization methods to overcome their severe limitations, even with extensive computational improvements.

To surmount the difficulties presented by an extremely large Hilbert space, we simulate the dynamics of the 1D BHH with a method called *time-evolving block decimation* (TEBD), commonly referred to as *Vidal's algorithm*. TEBD adaptively performs a partial trace over a particular bipartite splitting of our 1D lattice, and keeps the largest χ eigenvalues of the resulting reduced density matrix. Such a truncation is motivated by the fact that real, physical quantum many-body systems, particularly materials whose particles are lowly-entangled, typically only involve a small fraction of the total Hilbert space. Unlike exact diagonalization methods, TEBD scales linearly with the system size, thus allowing for the study of rather large systems.

TEBD, and its origins, are linked to the density matrix renormalization group (DMRG) method and the matrix product states ansatz. DMRG techniques, first developed by S. White in 1992, were similarly designed to find the ground state of a large 1D system through a systematic truncation of the Hilbert space. In the likeness of a numerical renormalization group (NRG) routine, in which the lowest energy states are retained, DMRG retains a small set of states in the truncation, corresponding to the most probable eigenstates of a reduced density matrix. Today, DMRG methods have gained interpretation as matrix product state routines. In this view, DMRG is an algorithm for optimizing a variational wavefunction with the structure of a matrix product state.

Before G. Vidal initially developed TEBD, several attempts were made to generalize DMRG methods to time-dependent simulations. The idea was to use standard

DMRG calculations to find the ground state of a system, and from this information ascertain a proper truncation of the Hilbert space for time evolution. The critical step was made by Vidal in 2003 [89, 90] when he discovered an optimal way to adaptively modify the truncation at each time step. This method generates a quasi-exact solution of the time-dependent many-body Schrödinger equation in 1D, provided that the Hamiltonian only links at most nearest-neighboring sites and that the state can always be represented by a sufficiently small number of retained basis states. The latter criterion requires that the amount of entanglement in the system be small, since the number of basis states necessary to effectively represent a quantum state, for a given bipartitate splitting, is a measure of the entanglement.

6.2 Vidal's Time-Evolving Block Decimation Algorithm

Assume that our system is a set of atoms in a 1D optical lattice, with L sites, that is well described by the BHH. To apply Vidal's algorithm, any pure state, $|\psi\rangle$, in the system's Hilbert space must be composed of a series of tensor products of local Hilbert spaces of dimension d, that is,

$$|\psi\rangle = \sum_{i_1,i_2,\ldots,i_L=1}^{d} C_{i_1 i_2 \ldots i_L} |i_1\rangle |i_2\rangle \ldots |i_L\rangle, \tag{6.3}$$

where $\{|i_l\rangle\}$ $(l = 1, 2, \ldots L)$ are the basis states in the local Hilbert space at site i. The ansatz in Eq. (6.3) is a general representation of a state in such a Hilbert space, and when $d = N$, it is an *exact* representation of the state. The essence of the TEBD algorithm is to decompose the coefficients $C_{i_1 i_2 \ldots i_L}$ of Eq. (6.3) into a favorable series of tensors using the Schmidt decomposition procedure.

6.2.1 Schmidt Decomposition

Let us split our 1D system into two blocks, block A and block B, with local subspace dimensions d_A and d_B, such that the pure state in Eq. (6.3) lives in the

Hilbert space $\mathcal{H}_A \otimes \mathcal{H}_B$. For this, or any other finite-dimensional bipartite splitting, there exists a decomposition of the form,

$$|\psi\rangle = \sum_{\alpha=1}^{\chi_S} \lambda_\alpha |\phi_\alpha^{[A]}\rangle \, |\phi_\alpha^{[B]}\rangle, \tag{6.4}$$

known as a Schmidt decomposition [91]. The states $|\phi_\alpha^{[A]}\rangle$ form an orthonormal basis for block A and the states $|\phi_\alpha^{[B]}\rangle$ form an orthonormal basis for block B. The Schmidt coefficients λ_α are unique real values, arranged in decreasing order $\lambda_1 \geq \lambda_2 \geq \ldots \geq \lambda_{\chi_S} \geq 0$, which satisfy the relationship $\sum_\alpha |\lambda_\alpha|^2 = 1$.

The number of Schmidt coefficients used in the expansion (Eq. (6.4)) is the Schmidt rank, χ_S, which is bounded by the dimension of the smaller subspace in the bipartite splitting, that is, $1 \leq \chi_S \leq min(d_A, d_B)$. The Schmidt rank indicates the level of entanglement for pure states. When $\chi_S = 1$ the system is in a product state, i.e. systems A and B are not entangled, while larger values of χ_S correspond to more highly entangled subsystems. This inequality demonstrates that the number of degrees of freedom which can be entangled between blocks A and B is restricted by the number of degrees of freedom inherent to the smaller subsystem.

6.2.2 Singular Value Decomposition

The Schmidt decomposition can be expressed through the language of the singular value decomposition theorem (SVD) from linear algebra. Consider a state for the bipartite system written in terms of two arbitrary orthogonal bases, $|i_A\rangle$ for block A and $|j_B\rangle$ for block B such that,

$$|\psi\rangle = \sum_{i,j} C_{i,j} \, |i_A\rangle \, |j_B\rangle. \tag{6.5}$$

where block A and B have dimensionalities m and n, and $C_{i,j}$ is $m \times n$ matrix of coefficients.

The SVD theorem says that there always exists two unitary matrices $\Gamma^{[A]}$ and

$\Gamma^{[B]^T}$ (where T denotes the transpose) and a diagonal matrix λ, such that the matrix C satisfies the relation, $C = \Gamma^{[A]}\,\lambda\,\Gamma^{[B]^T}$. Applying the SVD theorem to the state $|\psi\rangle$, we obtain the Schmidt decomposition in Eq. (6.4):

$$\begin{aligned}|\psi\rangle &= \sum_{i,j} C_{i,j}\,|i_A\rangle\,|j_B\rangle = \sum_{\alpha}\left(\sum_{i}\Gamma^{[A]}_{i,\alpha}\,|i_A\rangle\right)\lambda_{\alpha,\alpha}\left(\sum_{j}\Gamma^{[B]^T}_{\alpha,j}\,|j_B\rangle\right)\\ &= \sum_{\alpha}\lambda_{\alpha}|\phi^{[A]}_{\alpha}\rangle|\phi^{[B]}_{\alpha}\rangle,\end{aligned} \tag{6.6}$$

where we have defined,

$$|\phi^{[A]}_{\alpha}\rangle \equiv \sum_{i}\Gamma^{[A]}_{i,\alpha}\,|i_A\rangle, \quad |\phi^{[B]}_{\alpha}\rangle \equiv \sum_{j}\Gamma^{[B]^T}_{\alpha,j}\,|j_B\rangle, \quad \lambda_{\alpha} \equiv \lambda_{\alpha,\alpha}. \tag{6.7}$$

As we will see in the next section, the superscript in brackets $[l]$ denotes the site index, and the superscript without brackets i_l indicates that the system is in the local state $|i_l\rangle$; the α subscripts are the Schmidt indices from the Schmidt decomposition. Since Γ^A and Γ^B are unitary, it guarantees that $\{|\phi^{[A]}_{\alpha}\rangle\}$ and $\{|\phi^{[B]}_{\alpha}\rangle\}$ are orthonormal.

6.2.3 Vidal Representation Using Singular Value Decomposition

The key to the TEBD algorithm is to use the Schmidt decomposition to conveniently express the coefficients in Eq. (6.3),

$$|\psi\rangle = \sum_{i_1,i_2,\ldots,i_L=1}^{d} C_{i_1 i_2 \ldots i_L}|i_1\rangle|i_2\rangle\ldots|i_L\rangle,$$

as a series of local tensors $\Gamma^{[l]}$ and local vectors $\lambda^{[l]}$, at sites l. To see how this is possible, first let's apply the Schmidt decomposition to our 1D system, with the bipartite splitting occurring between sites 1 and 2. In such a case, block A is composed of a single site while block B is composed of the remaining $L-1$ sites. The state is then expressed as,

$$|\psi\rangle = \sum_{\alpha_1=1}^{\chi_S}\lambda^{[1]}_{\alpha_1}|\phi^{[1]}_{\alpha_1}\rangle\,|\phi^{[2\ldots L]}_{\alpha_1}\rangle, \tag{6.8}$$

where we have chosen to label the block (super scripts) by the site number. Now, rewriting the state $|\phi^{[1]}_{\alpha_1}\rangle$ in the local basis for site 1, as defined in Eq. (6.7), we obtain,

$$|\psi\rangle = \sum_{\alpha_1;i_1}^{\chi_S} \Gamma^{[1]i_1}_{\alpha_1} \lambda^{[1]}_{\alpha_1} |i_1\rangle |\phi^{[2\ldots L]}_{\alpha_1}\rangle, \tag{6.9}$$

where we have shifted all the i indices to be superscripts and α indices to be subscripts. The superscript in brackets $[l]$ denotes the site index, and the superscript without brackets i_l indicates that the system is in the local state $|i_l\rangle$; the α subscripts are the Schmidt indices from the Schmidt decomposition.

We perform a similar expansion for the state $|\phi^{[2\ldots L]}_{\alpha_1}\rangle$ in the local basis for site 2 $|i_2\rangle$ in terms of the orthonormal basis for sites $3 \ldots L$:

$$|\phi^{[2\ldots L]}_{\alpha_1}\rangle = \sum_{\alpha_2;i_2} |i_2\rangle \Gamma^{[2]i_2}_{\alpha_1,\alpha_2} \lambda^{[2]}_{\alpha_2} |\phi^{[3\ldots L]}_{\alpha_2}\rangle. \tag{6.10}$$

Notice that the Γ tensor corresponding to the first site depended on only one α index, since there is only one adjacent block, while the Γ tensor for site 2 depends on two indices, α_1 and α_2, since there are two adjacent blocks next to site 2. Substituting Eq. (6.10) into Eq. (6.9) we obtain,

$$|\psi\rangle = \sum_{\alpha_1,\alpha_2;i_1,i_2}^{\chi_S} \Gamma^{[1]i_1}_{\alpha_1} \lambda^{[1]}_{\alpha_1} \Gamma^{[2]i_2}_{\alpha_1,\alpha_2} \lambda^{[2]}_{\alpha_2} |i_1\rangle |i_2\rangle |\phi^{[3\ldots L]}_{\alpha_2}\rangle. \tag{6.11}$$

We can repeat the process for the state $|\phi^{[3\ldots L]}_{\alpha_2}\rangle$ in the local basis for site 3 $|i_3\rangle$, and iteratively repeat for each subsequent state, until we reach site L, in order to form the Vidal decomposition

$$|\psi\rangle = \sum_{i_1,i_2,\ldots,i_L=1}^{d} C_{i_1 i_2 \ldots i_L} |i_1\rangle |i_2\rangle \ldots |i_L\rangle,$$

$$C_{i_1 i_2 \ldots i_L} = \sum_{\alpha_1,\ldots,\alpha_{L-1}}^{\chi_S} \Gamma^{[1]i_1}_{\alpha_1} \lambda^{[2]}_{\alpha_1} \Gamma^{[2]i_2}_{\alpha_1\alpha_2} \lambda^{[3]}_{\alpha_2} \Gamma^{[3]i_3}_{\alpha_2\alpha_3} \ldots \Gamma^{[L]i_L}_{\alpha_{L-1}}, \tag{6.12}$$

for open boundary conditions.[1] A pictorial way of seeing this is shown in Fig. 6.1; for purposes of interpretation it is useful to associate the Γs with sites and the λs with the links between sites. The lines represent the contractions over the Schmidt indices.

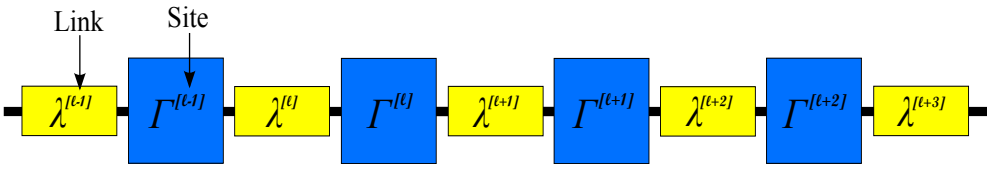

Figure 6.1: *Vidal Decomposition Schematic.* A pictorial way to view the Vidal decomposition is to associate the Γs with sites and the λs with the links between sites. The lines represent the contractions over the Schmidt indices.

One major reason why the TEBD algorithm is successful is because the coefficients of the Schmidt decomposition decay exponentially, $\lambda_\alpha^{[l]} \exp(-\alpha)$, thus, with the removal of sufficiently small coefficients, the Hilbert space can be truncated to some degree of optimality, while still capturing the many-body physics.

Note that the TEBD algorithm is not restricted to splittings corresponding to physical sites in a lattice. In fact, the subsystems can be separated in whatever manner we may choose.

The Schmidt coefficients λ_α are intimately related to the reduced density matrices for the two blocks of the system via,

$$\rho_A = Tr_B(|\psi\rangle\langle\psi|) = \sum_{\alpha=1}^{\chi_S} \lambda_\alpha^2 |\phi_\alpha^{[A]}\rangle\langle\phi_\alpha^{[A]}|, \tag{6.13}$$

$$\rho_B = Tr_A(|\psi\rangle\langle\psi|) = \sum_{\alpha=1}^{\chi_S} \lambda_\alpha^2 |\phi_\alpha^{[B]}\rangle\langle\phi_\alpha^{[B]}|, \tag{6.14}$$

[1] Eq. (6.12) has a slightly different representation for periodic boundary conditions due to the difference in conditions for the first and last blocks. The extra indices incurred lead to a less favorable numerical scaling.

and obey the eigen-relations,

$$\rho_A|\phi_\alpha^{[A]}\rangle = |\lambda_\alpha|^2|\phi_\alpha^{[A]}\rangle \tag{6.15}$$

$$\rho_B|\phi_\alpha^{[B]}\rangle = |\lambda_\alpha|^2|\phi_\alpha^{[B]}\rangle. \tag{6.16}$$

This is critical to our descriptions of entanglement, due to the fact that the amount of information in a system and the entanglement between two subsystems can both be quantified by the von Neumann entropy, given by,

$$S(A) = -Tr[\rho_A \log_2 \rho_A] = -\sum_\alpha^\chi \lambda_\alpha^2 \log_2 \lambda_\alpha^2 \tag{6.17}$$

which is the same for subsystems A and B.

6.2.4 One-Site Operations

Applying the Vidal decomposition to a Hamiltonian like the BHH, requires that we be able to handle both one-site and two-site operators acting on a state in the 1D system. A one-site unitary operator,$\hat{U}$, acting on site l can be represented as

$$\hat{U} = \sum_{i_l, i_l'} U_{i_l, i_l'} |i_l\rangle\langle i_l'|. \tag{6.18}$$

In the Vidal state representation (6.12), the 1D chain is broken down into a series of Γs and λs. The effect of the operation $\hat{U}$ is to change the $\Gamma^{[l]i_l}$ tensor into a new $\tilde{\Gamma}$ tensor given by,

$$\tilde{\Gamma}^{[l]i_l}_{\alpha_{l-1}\alpha_l} = \sum_{i_l'} U_{i_l, i_l'} \Gamma^{[l]i_l'}_{\alpha_{l-1}\alpha_l}. \tag{6.19}$$

Since $\hat{U}$ is local to site l only the $\Gamma^{[l]i_l}$ tensor should be altered and not any of the other Γs or links λ.

Computationally, one-site operations only require updating $\Gamma^{[l]i_l} \rightarrow \tilde{\Gamma}^{[l]i_l}$, a procedure which scales as $O(d\chi^2)$. As we will see in the next section, two-site operations

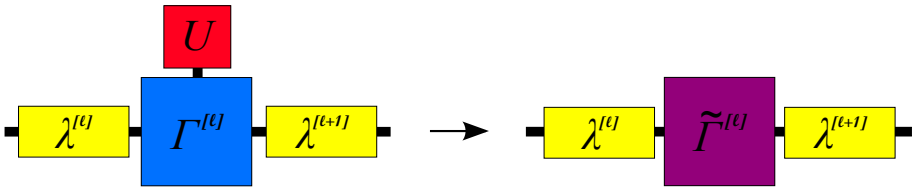

Figure 6.2: *One-site Operation Schematic.* A pictorial way to view the one-site operation. The operator $\hat{U}$ changes the $\Gamma^{[l]}$ tensor into a new $\tilde{\Gamma}^{[l]}$ tensor.

are much more costly.

6.2.5 Two-Site Operations

Now consider a two-site unitary operator $\hat{V}$ acting on sites l and $l+1$ in our 1D system. Such an operator can be represented by,

$$\hat{V} = \sum_{i_l, i_{l+1}; i_l^{'}, i_{l+1}^{'}} V_{i_l^{'} i_{l+1}^{'}}^{i_l i_{l+1}} |i_l i_{l+1}\rangle\langle i_l^{'} i_{l+1}^{'}|. \tag{6.20}$$

We write the state $|\psi\rangle$ as a bipartite splitting between l and $l+1$ in terms of the Schmidt vectors to the left of the two sites $[1 \ldots l-1]$ and to the right of the two sites $[l+2 \ldots L]$, as

$$\begin{aligned} |\psi\rangle &= \sum_{\alpha_{l-1}, \alpha_l, \alpha_{l+1}; i_l, i_{l+1}} \lambda_{\alpha_{l-1}}^{[l]} \Gamma_{\alpha_{l-1}\alpha_l}^{[l] i_l} \lambda_{\alpha_l}^{[l+1]} \Gamma_{\alpha_l \alpha_{l+1}}^{[l+1] i_{l+1}} \lambda_{\alpha_l+1}^{[l+2]} |\phi_{\alpha_{l-1}}^{[1 \ldots l-1]}\rangle \otimes |i_l i_{l+1}\rangle \otimes |\psi_{\alpha_{l+1}}^{[l+2 \ldots L]}\rangle \\ &= \sum_{\alpha_{l-1}, \alpha_l, \alpha_{l+1}; i_l, i_{l+1}} \Theta_{\alpha_{l-1}\alpha_{l+1}}^{i_l i_{l+1}} |\phi_{\alpha_{l-1}}^{[1 \ldots l-1]}\rangle \otimes |i_l i_{l+1}\rangle \otimes |\psi_{\alpha_{l+1}}^{[l+2 \ldots L]}\rangle \end{aligned} \tag{6.21}$$

where the object Θ is,

$$\Theta_{\alpha_{l-1}\alpha_{l+1}}^{i_l i_{l+1}} \equiv \lambda_{\alpha_{l-1}}^{[l-1]} \Gamma_{\alpha_{l-1}\alpha_l}^{[l] i_l} \lambda_{\alpha_l}^{[l]} \Gamma_{\alpha_l \alpha_{l+1}}^{[l+1] i_{l+1}} \lambda_{\alpha_l}^{[l+2]}. \tag{6.22}$$

Schematically, think about this two-site operation as consisting of two Γs and three λs, where the middle λ is replaced by an effective Γ. When the two-site operation $\hat{V}$ acts on the state $|\psi\rangle$, similar to the one-site operation, it changes the two Γs and the

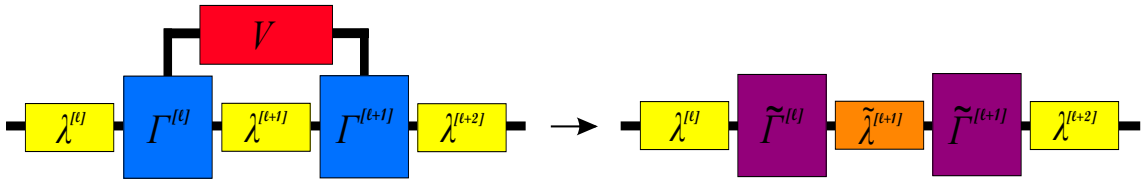

Figure 6.3: *Two-site Operation Schematic.* A pictorial way to view the two-site operation. The operator $\hat{V}$ changes both the $\Gamma^{[l]}$ tensor and the $\Gamma^{[l+1]}$ tensor into a new $\tilde{\Gamma}^{[l]}$ and $\tilde{\Gamma}^{[l+1]}$ tensor. The operator $\hat{V}$ also modifies the link $\lambda^{[l+1]}$ to a new $\tilde{\lambda}^{[l+1]}$

link λ in between. Thus, the Θ object becomes an effective $\tilde{\Theta}$ such that,

$$\hat{V}|\psi\rangle = \sum_{\alpha_{l-1},\alpha_l,\alpha_{l+1};i_l,i_{l+1}} \tilde{\Theta}^{i_l i_{l+1}}_{\alpha_{l-1}\alpha_{l+1}} |\phi^{[1\ldots l-1]}_{\alpha_{l-1}}\rangle \otimes |i_l i_{l+1}\rangle \otimes |\psi^{[l+2\ldots L]}_{\alpha_{l+1}}\rangle \tag{6.23}$$

where,

$$\tilde{\Theta}^{i_l i_{l+1}}_{\alpha_{l-1}\alpha_{l+1}} = \sum_{i_{l'},i_{l'+1}} V^{i_l i_{l+1}}_{i'_l i'_{l+1}} \Theta^{i'_l i'_{l+1}}_{\alpha_{l-1}\alpha_{l+1}} \tag{6.24}$$

$$= \sum_{\alpha_l} \lambda^{[l-1]}_{\alpha_{l-1}} \tilde{\Gamma}^{[l]i_l}_{\alpha_{l-1}\alpha_l} \tilde{\lambda}^{[l]}_{\alpha_l} \tilde{\Gamma}^{[l+1]i_{l+1}}_{\alpha_l\alpha_{l+1}} \lambda^{[l+2]}_{\alpha_l}. \tag{6.25}$$

The Schmidt coefficients are normalized in the fashion,

$$\sum_{\alpha_l}^{\chi_S} \left(\lambda^{[l+1]}_{\alpha_l}\right)^2 = 1. \tag{6.26}$$

Thus when we perform SVD on the matrix $\tilde{\Theta}$, and keep only the χ largest singular values $\tilde{\lambda}^{[l+1]}_{\alpha_l}$, the truncation error involved with such a procedure, called the Schmidt error, may be calculated, and is given by

$$\tau^S_l \equiv 1 - \sum_{\alpha_l}^{\chi} \left(\lambda^{[l+1]}_{\alpha_l}\right)^2. \tag{6.27}$$

For large enough χ the Schmidt error tends to zero. Since this error is dependent on the choice of χ, which is an indicator of the level of entanglement, we say that TEBD is best suited for lowly entangled systems. The entropy, at worst, scales as $\log(L)$

at critical points, and otherwise follows the area law so that it does not depend on system size [92].

6.3 Time Evolution and Suzuki-Trotter Decomposition

To perform time-dependent simulations of a Hamiltonian with TEBD, the *time evolution operator*, $\exp(-i\hat{H}\delta t/\hbar)$, which contains our Hamiltonian and hence one- and two-site unitary operations, must be expressed in the language introduced in Sections 6.2.4 and 6.2.5. A convenient means of decomposing the exponential is through a Suzuki-Trotter expansion.

The form of the time evolution operator is obtained from integration of the time-dependent Schrödinger equation, $\hat{H}|\psi(t)\rangle = i\hbar\frac{\partial}{\partial t}|\psi(t)\rangle$. Given an initial state $|\psi(0)\rangle$ and a time independent Hamiltonian, the state at a later time δt can be expressed as $|\psi(\delta t)\rangle = \exp(-i\hat{H}\delta t/\hbar)\,|\psi(0)\rangle$.

A Suzuki-Trotter expansion is a general way of writing exponential operators, and to first-order is given by

$$e^{(\hat{F}+\hat{G})} = \lim_{n\to\infty}\left(e^{\frac{\hat{F}}{n}}e^{\frac{\hat{G}}{n}}\right)^n \tag{6.28}$$

or, equivalently,

$$e^{(\hat{F}+\hat{G})\delta t} = \lim_{\delta t\to 0}\left[e^{\hat{F}\delta t}e^{\hat{G}\delta t} + O(\delta t^2)\right], \tag{6.29}$$

where $\hat{F}$ and $\hat{G}$ are, for now, arbitrary operators. The size of the correction term can be reduced with higher order expansions, for example, the trick to the second-order Suzuki-Trotter expansion relies on expressing the time evolution operator as:

$$e^{-i(\hat{F}+\hat{G})T} = \left[e^{-i(\hat{F}+\hat{G})\delta t}\right]^{T/\delta t} = \left[e^{\frac{\delta t}{2}F}e^{G\delta t}e^{\frac{\delta t}{2}F}\right]^n, \tag{6.30}$$

where $n = T/\delta t$ is called the Trotter number.

Defining the operators $\hat{F}$ and $\hat{G}$ in the context of our Hamiltonian is fairly

straightforward. If the Hamiltonian consists of only one- and two-site operations,[2] that act on the local Hilbert spaces for sites i and $i+1$, then we can break the total Hamiltonian into two sums

$$\hat{H} = \sum_{l \text{ odd}} \hat{H}_{l,l+1} + \sum_{l \text{ even}} \hat{H}_{l,l+1} = \hat{F} + \hat{G}, \tag{6.31}$$

where the one-site operations in $\hat{H}$ can be easily expressed as two-site operations by taking the tensor product with the identity operator. For example, in the BHH, the particle-particle interaction operator $\hat{U}$ (a one-site operator), can be written in terms of two-site operations with $\frac{1}{2}(\hat{U} \otimes \hat{1} + \hat{1} \otimes \hat{U})$. Notice that because $\hat{H}$ is composed of terms that couple only at most nearest-neighbor sites, i.e., $[\hat{H}_l, \hat{H}_{l+j}] = 0$ for $j \geq 2$, the terms within $\hat{F}$ and $\hat{G}$ commute (although $\hat{F}$ and $\hat{G}$ themselves do not commute). The time evolution operator for such a Hamiltonian is neatly decomposed, as in Eq. (6.30), by the second-order Suzuki-Trotter expansion:

$$e^{-i\hat{H}\delta t/\hbar} = e^{-i\hat{F}\delta t/2\hbar} e^{-i\hat{G}\delta t/\hbar} e^{-i\hat{F}\delta t/2\hbar} + O(\delta t^3), \tag{6.32}$$

where,

$$e^{-i\hat{F}\delta t/2\hbar} = \exp\left(-i \sum_{l \text{ odd}} \hat{H}_{l,l+1}\delta t/2\hbar\right) = \prod_{l \text{ odd}} e^{-i\hat{H}_{l,l+1}\delta t/2\hbar} \tag{6.33}$$

$$e^{-i\hat{G}\delta t/2\hbar} = \exp\left(-i \sum_{l \text{ even}} \hat{H}_{l,l+1}\delta t/2\hbar\right) = \prod_{l \text{ even}} e^{-i\hat{H}_{l,l+1}\delta t/2\hbar}. \tag{6.34}$$

This process involves on the order of $O(L)$ two-site operations per time step.

A fourth-order Suzuki-Trotter expansion of the time evolution operator can be obtained from the Forrest-Ruth formula, first discovered in 1990, and in most cases will reduce the error even further [93]. Using the same operators $\hat{F}$ and $\hat{G}$ from

[2] For example, the BHH.

Eqs. (6.33) and (6.34), the fourth-order Suzuki-Trotter expansion is given by

$$e^{-i\hat{H}\delta t/\hbar} = e^{-i\hat{F}\theta\delta t/2\hbar}e^{-i\hat{G}\theta\delta t/\hbar}e^{-i\hat{F}(1-\theta)\delta t/2\hbar} + e^{-i\hat{G}(1-2\theta)\delta t/\hbar} + e^{-i\hat{F}(1-\theta)\delta t/2\hbar} + e^{-i\hat{G}\theta\delta t/\hbar} + e^{-i\hat{F}\theta\delta t/2\hbar} + O(\delta t^5), \tag{6.35}$$

where $\theta \equiv 1/(2-2^{1/3})$ is called the Forrest-Ruth parameter.

Higher order Suzuki-Trotter expansions separate the time evolution operator into a larger number of factors, for example, two factors in the first-order, three in the second-order, and seven in the fourth-order, which increases the computation time. However, in situations where the Hamiltonian is not changing rapidly over short time scales, higher order expansions allow us to take substantially coarser time steps with the same level of accuracy, hence reducing our overall computation time and the total Schmidt error. The fourth-order decomposition is the most common method used in simulations throughout this thesis.

For p^{th}-order expansions, the Schmidt error is of order $O(\delta t^{p+1})$. After a time T the error is

$$\epsilon\frac{T}{\delta t}\delta t^{p+1} = T\delta t^{p}, \tag{6.36}$$

where $n = T/\delta t$. Notice that the Trotter error is independent of the dimension of the 1D chain.

6.4 Initializing States and Imaginary Time Propagation

If the initial state we wish to prepare for time evolution is a simple product state $|\psi_p\rangle$, initialization is simple. In the context of Eq. (6.12), we take

$$\lambda_{\alpha_l}^{[l+1]} = \delta_{\alpha,l} \tag{6.37}$$

where $\delta_{\alpha_l,l}$ is a Kronecker delta, thus reducing $C_{i_1,i_2,\ldots i_L}$ to a single term.

To find the system's ground state, which may be complicated or unknown one can

use the imaginary time propagation method, discussed in Section 4.2. It is straightforward to show that an initial product state $|\psi_p\rangle$ will converge to a value proportional to the system's ground state $|\psi_G\rangle$ in the limit $\tau \to \infty$, provided that the starting state and the ground state are not orthogonal, that is, $\langle\psi_p|\psi_G\rangle \neq 0$. Thus the procedure is: (1) choose a product state $|\psi_p\rangle$ that has some overlap to the desired ground state, (2) evolve in imaginary time to obtain the ground state $|\psi_G\rangle$, (3) with the ground state thus obtained, we can evolve it in real time using the methods described in Section 6.3. It is also common to take a perturbed form of the ground state as the starting point for real time evolution. For example, we will take bright solitons localized in the well behind the barrier as the initial states in our investigations of quantum many-body tunneling.

Imaginary time evolution is not unitary. Thus we have to renormalize and reorthogonalize the state, specifically the Θ tensor from Section 6.2.5, at each step in imaginary time. A fourth-order Suzuki-Trotter expansion is usually preferred, because taking larger time steps means a fewer number of times that we must renormalize and reorthogonalize the state.

Chapter 7

QUANTUM MANY-BODY TUNNELING OF BRIGHT SOLITONS

In this chapter, we investigate quantum many-body tunneling of bright solitons in Bose-Einstein condensates, and compare the simulations obtained from the time-evolving block decimation and mean field methods. Through such a comparison, in this chapter we will now be able to address the question: when is a full quantum many-body approach necessary for adequately describing our system? In turn, we will quantitatively determine the extent to which mean field theory fails to predict the escape time of a bright soliton from behind a potential barrier for large interaction strengths. Finally, the full quantum-many body method provides us with the added benefit of utilizing a wide arsenal of quantum measures to analyze macroscopic quantum tunneling. Thus, we use tools, such as the block entropy and density-density correlation functions to name a few, to probe the dynamics of MQT. Bright solitons in BECs have already been observed [26, 27], including in optical lattices [54], so that our predictions and ideas can be tested with present experimental apparatus. In particular, the small number of atoms we work with, from a few to 70, can be created in a 2D array of 1D systems [94].

7.1 Forming Bright Solitons With Imaginary Time Propagation

The governing Hamiltonian is the 1D BHH from Eq. (2.26), which when explicitly including the chemical potential is written as

$$\hat{H} = -J\sum_{i=1}^{L-1}(\hat{b}_i^\dagger \hat{b}_{i+1} + \hat{b}_i \hat{b}_{i+1}^\dagger) + \frac{U}{2}\sum_{i=1}^{L}\hat{n}_i(\hat{n}_i - I) + \mu\sum_i \hat{n}_i. \tag{7.1}$$

To attain bright solitons, we use condensates with attractive particle interactions, $U \leq 0$, and a negative chemical potential, $\mu \leq 0$. As in the mean field case, the

system consists of N bosons loaded into an optical lattice with L sites and box boundary conditions.

Imaginary time propagation, discussed in Section 6.4, is used to find the bright soliton many-body state. For imaginary time propagation, an initial state that is roughly Gaussian in structure will quickly converge to a bright soliton solution, due to the substantial overlap between the two states. For number conserving simulations, we initialize our system as a simple "wedding cake" product state– a structure designed to approximate a Gaussian number density in which all of the Γs are expressed in a basis of number eigenstates. The wedding cake consists of two tiers which differ in on-site number by one, and whose dimensions are specified by three integer parameters: *tops*, *center*, and *hole*, whose names originate from variable definitions in the TEBD code. The upper tier is "*tops*" sites long, with "*center*" being the on-site number in the upper tier, and $(center - 1)$ being the on-site number in the lower tier. "$Hole$" is the number of sites to the left of the upper tier without a particle. These three parameters are controlled by the filling, and whether the number of sites with the fewest amount of particles is even or odd. For integer filling, there is a uniform number of particles per site, thus there can be no hole, i.e. $hole = 0$. For non-integer filling, and an even number of sites with the fewest particles, the hole is given by $hole = \frac{1}{2}(L - MOD(N, L))$. If the number of sites with the fewest particles is odd, then $hole = \frac{1}{2}(L - MOD(N, L) + 1)$. In summary, the wedding cake procedure is:

$$\begin{aligned} tops &\equiv MOD(N-1, L) + 1, \\ center &\equiv [N/L - 10^{-8}] + 1, \end{aligned} \tag{7.2}$$

$$hole \equiv \begin{cases} 0 & \text{if, } MOD(N, L) = 0 \\ \frac{1}{2}(L - MOD(N, L)) & \text{if, } MOD(L - MOD(N, L), 2) = 0 \\ \frac{1}{2}(L - MOD(N, L) + 1) & \text{otherwise} \end{cases} \tag{7.3}$$

The procedure is made more clear by a picture of the wedding cake state, shown in Fig. 7.1.

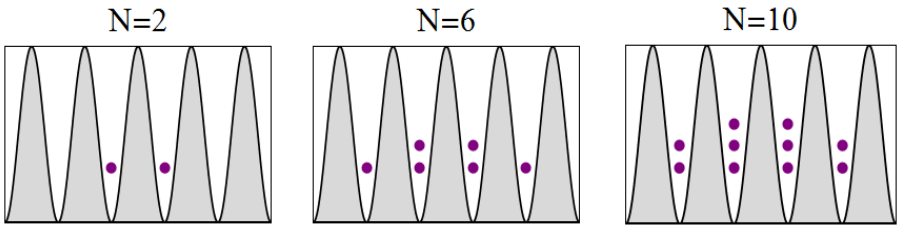

Figure 7.1: *Wedding Cake Initial State.* A wedding cake state is used as the initial setup for imaginary time evolution in order to form a bright soliton. The figure shows the configuration for a system with: $N = 2$, $N = 6$, and $N = 10$ particles. Other arrangements can be made with Eq. (7.2).

Due to the scaling of the computation time with χ, the number of basis states retained for every two-site operation in TEBD, we propagate in two iterations of imaginary time. First, we use a small, χ_{min}, to quickly shape the initial state, and then apply a larger, $\chi_{max} > \chi_{min}$, to refine the state into a bright soliton. Convergence for each iteration in imaginary time is defined by two convergence criteria, "$convCriterion1$" and "$convCriterion2$" respectively.[1] The first (second) iteration of imaginary time propagation is said to be converged if the difference between all $\lambda_\alpha^{[l]}$ at imaginary time τ and imaginary time $\tau + stepsForJudge * dtITP$ is less than $convCriterion1 = 10^{-7}$ ($convCriterion2 = 10^{-9}$). The number of imaginary time steps after which we check for convergence, $stepsForJudge$, is set to 500, with $dtITP$ as the time step. Once imaginary time is completed, the bright soliton state is be checked by fitting the profile to a sech^2 function. The height and width of the soliton is determined by the quantity NU/J and the system size L.

Using a rectangular external potential barrier V_{ext}, as in the mean field case, we can confine a bright soliton between the barrier and one of the system walls. A

[1] Terminology derives from variable definitions in our TEBD code.

rectangular potential barrier term is thus added to the BHH, yielding

$$\hat{H} = -J\sum_{i=1}^{L-1}(\hat{b}_i^\dagger\hat{b}_{i+1} + \hat{b}_i\hat{b}_{i+1}^\dagger) + \frac{U}{2}\sum_{i=1}^{L}\hat{n}_i(\hat{n}_i - I) + \mu\sum_i \hat{n}_i + \sum_i V_{ext,i}\,\hat{n}_i. \tag{7.4}$$

We initialize the many-body wavefunction as a wedding cake product state, and by way of imaginary time propagation, form a bright soliton behind the potential barrier. We use the same barrier setup as in the mean field case, shown in Fig. 4.2. That is, we set V_{ext} to a height $h = 0.05$ and an initial width w_I during imaginary time propagation. At $t = 0$, in real time, the barrier is decreased to width w, typically one to five sites, such that the soliton can escape confinement on a time scale within the window of the given simulation.

7.2 Real Time Soliton Dynamics

Evolving in real time, we first make a coarse observation of the dynamics of MQT in Fig. 7.2 by plotting the average particle number in different regions of the system. As opposed to the mean field case, where we plotted the number density, for the quantum many-body problem we must plot a number density which is averaged over many experimental runs. The average particle number is simply the expectation value of the number operator,

$$\langle\hat{n}\rangle = \sum_{n=0}^{d-1} n|n\rangle\langle n|, \tag{7.5}$$

where the expectation value is calculated via $\langle\hat{n}_i\rangle = \text{Tr}\,(\hat{\rho}_i\hat{n})$, using the reduced density matrix $\hat{\rho}_i$, at site i. An observable useful for determining the escape time of a bright soliton is the average number of particles to the left of site i, $\langle N_i\rangle$, where we typically set i to be the site at the outer edge of the barrier. The advantage of using $\langle N_i\rangle$, as opposed to the average particle number at a specific site, is that as a bright soliton tunnels through the barrier, $\langle N_i\rangle$ will normally exhibit a smooth decay, from which $t_{\text{esc}}^{\text{MB}}$, i.e., the time at which the average number of particles remaining behind

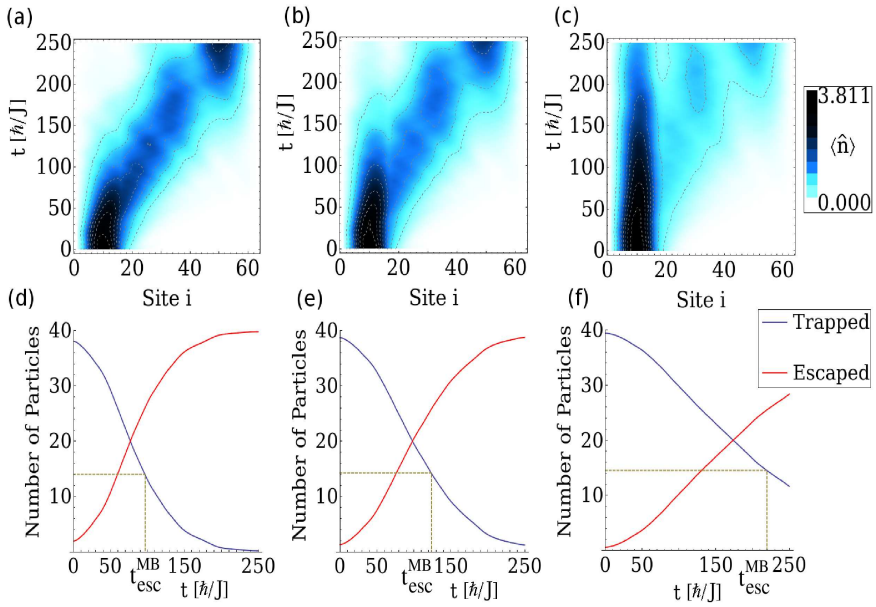

Figure 7.2: *Many-Body Tunneling, and Calculation of Decay Time.* Average particle number per site (top row) and number of trapped (blue) and escaped (red) particles (bottom row), for barrier widths $w = 1$ (left), $w = 2$ (middle), and $w = 4$ (right); the $1/e$ decay time is $t_{\rm esc}^{\rm MB} = 96.9$, 123.9, and 219.4, all ± 1.25, respectively. This example shows systems all of $N = 40$, $U = 0.0075$ and $J = 1$.

the barrier falls to $1/e$ of its initial value, can be easily calculated. In Fig. 7.2, we plot $\langle N_i \rangle$ to the left of the barrier, and the average number to the right of the barrier for three barrier widths, demonstrating that $t_{\rm esc}^{\rm MB}$ increases with w.

Absorbing boundary conditions have not been implemented with number conserving BHH simulations, so reflections occur off of the box boundaries, as shown in Fig. 7.2, for $t \geq 250$. Reflections from the far boundary will return to the barrier on time scales $t_{\rm ref} \geq t_J * 2w_I$, where t_J is the hopping time, the average time it takes for a particle to move one site. We may ignore reflections when calculating $t_{\rm esc}^{\rm MB}$ if we consider only $t < t_{\rm ref}$. If $t_{\rm esc}^{\rm MB} > t_{\rm ref}$, the escape time can be extrapolated by fitting the norm to an exponential.

Several parameters will control the dynamics of MQT: $\nu U/J$ sets the initial mean field, $\nu = N/L$ controls the initial average density, U/J serves as a ground state phase transition control parameter, and $w^2 h$ determines the barrier area. We define the barrier area as $w^2 h$ to make it unitless. Since the barrier height h has units

of energy, we divide by $\hbar^2/mw^2$ taking $\hbar, m \to 1$ to obtain w^2h. The dependence of the escape time on these parameters, using both the DNLS and the BHH, will be shown later in Fig. 7.4.

7.3 Comparison to Mean Field Theory

The BHH approaches the DNLS in the mean field limit $N \to \infty$, $U \to 0$, $NU/J = \text{const}$. We emphasize that both the BHH and the DNLS are single band models, valid when the soliton covers many sites; a continuum limit is possible for $\nu J = \text{const.}$, $\nu \equiv N/L \to 0$ and $J \to \infty$; however, a continuum limit would restrict us numerically to very small numbers of particles [95].

When the interaction strength is nonzero an appropriate mapping is required to compare BHH and DNLS simulations, due to the factor of 1/2 that appears in the interaction term of the BHH. The mapping, for fixed N and J, is to set $U = 2g$ while normalizing the mean field wavefunction to N. This scaling ensures that when one approaches the mean field the limit, for small but nonzero on-site interactions, the difference between the two methods becomes negligible.

When the interaction strength is sufficiently large, the DNLS simulations begin to deviate from the BHH simulations. For instance, the height and width of the bright soliton state, generated after imaginary time evolution, varies between the two methods. In Fig. 7.3, using both the BHH and the DNLS, we plot the average on-site number of the bright soliton state and the standard deviation of the difference between the two methods for various values of the interaction strength. When the interaction strength approaches zero, we find that the difference between the two methods is less than 10^{-5}. The difference in the initial states between the two methods is important to consider, since the height and width of the soliton largely determines the rate of macroscopic quantum tunneling.

Turning now to real time simulations, how do many body predictions compare to mean field ones? We define $t_{\text{esc}}^{\text{MF}}$ and $t_{\text{esc}}^{\text{MB}}$ as the mean field and many body escape

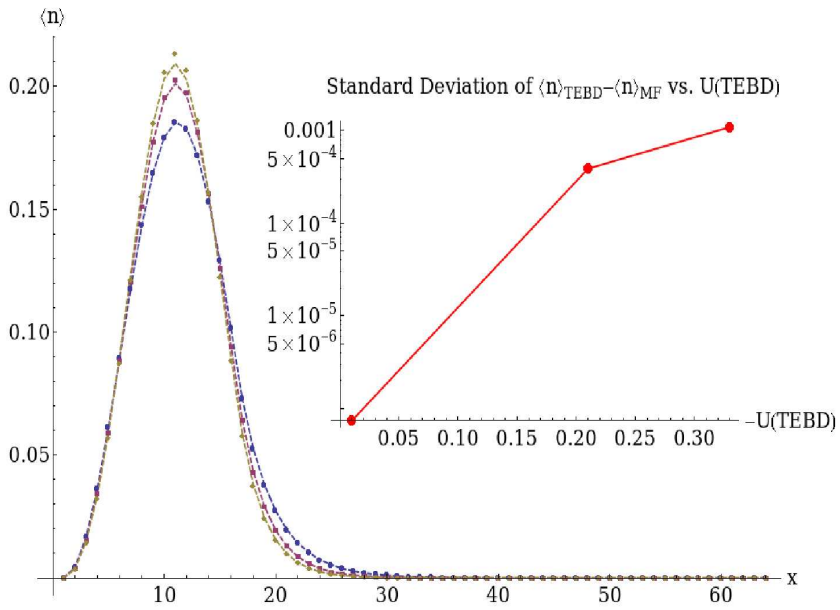

Figure 7.3: *Initial State vs. Interaction Strength Using the BHH and the DNLS.* The bright soliton state for the BHH (dashed lines) and the DNLS (dots) simulations is slightly different, due the the inaccuracy of mean field theory for large interaction strengths. In the noninteracting limit, the difference between the two methods is driven to zero. This example shows values of $|U| = 0.01$ (blue), 0.21 (red), and 0.33 (yellow), for $N = 2$ and $w = 3$.

times, respectively. For fixed NU/J, w, and h, the DNLS gives the same result independent of N and U; $t_{\rm esc}^{\rm MB} \to t_{\rm esc}^{\rm MF}$ only for $N \to \infty$ and $U \to 0$; and $w^2 h$ determines the barrier area. Figure 7.4 illustrates our exploration of this parameter space, where we plot the escape time, for different barrier areas calculated using both the DNLS and the BHH. Consistent with our previous simulations, we again set $J = 1$, $L = 64$, with the barrier starting at site 16, and plot the escape time for various values of N and U. In Fig. 7.4(a)-(d), we illustrate comparisons for $N = 1$ to $N = 40$, for systems of fixed $N|U|/J = 0.05$, 0.15, 0.3, and 0.5.

We find distinctive differences in the dynamics of MQT predicted by the DNLS and BHH. Generally, the DNLS grossly under predicts $t_{\rm esc}$ when $N|U|/J$ is sufficiently large, even for $N = 40$. Since our well width is 16 lattice sites, we expect the mean field limit will only be relevant for 70 or more particles, when the filling $\nu \gg 1$. Except for $N = 1$, the BHH predicts an increase in $t_{\rm esc}$ over the DNLS, approaching a

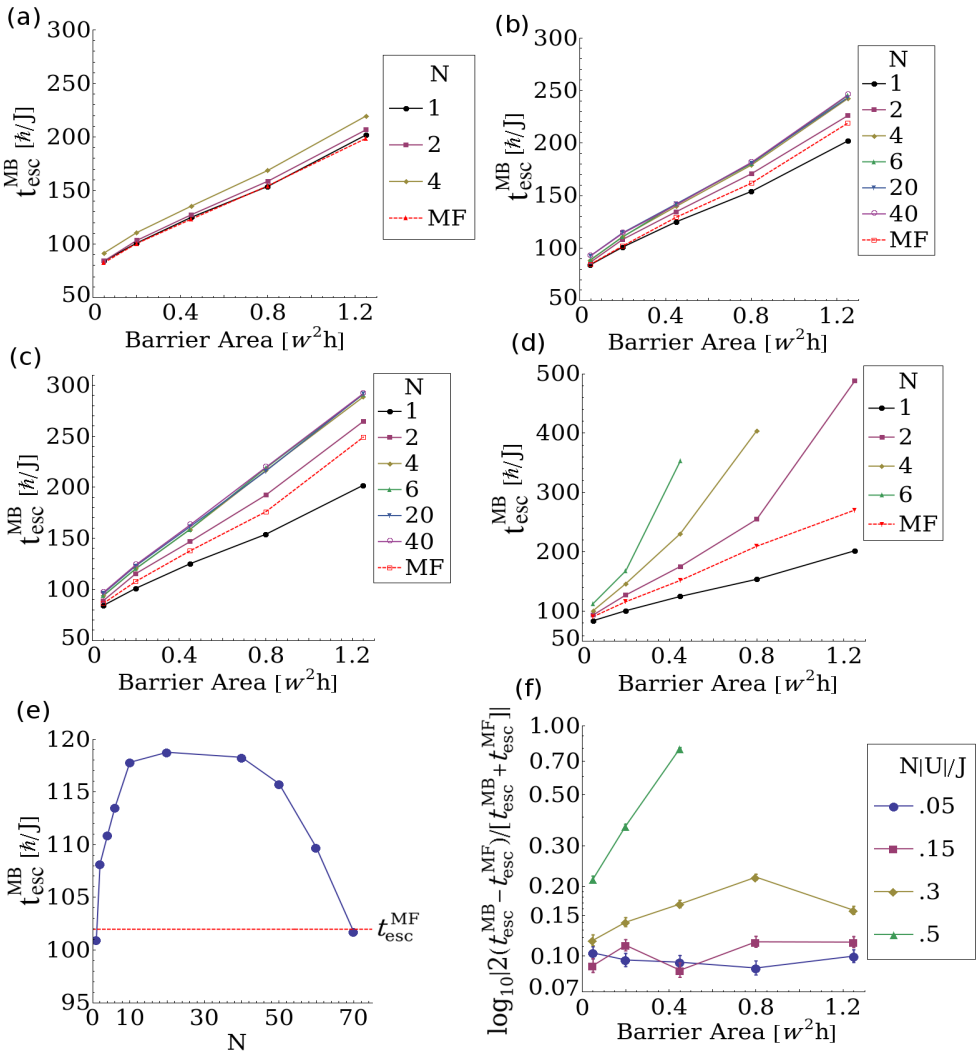

Figure 7.4: *Many Body vs. Mean Field Escape Time Predictions.* (a)-(d) Dependence of $t_{\rm esc}^{\rm MB}$ on barrier area and particle number for (a) $NU/J = -0.05$, (b) -0.15, (c) -0.3, and (d) -0.5. (e) $t_{\rm esc}^{\rm MB}$ plateaus for 10 to 40 particles and then decreases back down to $t_{\rm esc}^{\rm MF}$, shown for $NU/J = -0.15$. (f) In the plateau region of $N = 40$, $t_{\rm esc}^{\rm MB}$ significantly differs from $t_{\rm esc}^{\rm MF}$ for a range of barrier areas and interaction strengths. Curves are a guide to the eye, points represent actual data.

maximum value for $N = 40$. We have shown that $t_{\rm esc}^{\rm MB}$ will subsequently decrease back down to $t_{\rm esc}^{\rm MF}$ when $N > 70$. Figure 7.4(e) shows this scenario for fixed $NU/J = -0.15$, showing that $t_{\rm esc}$ plateaus at a maximal value for $N \geq 20$ up to $N = 40$ and then decreases back down to $t_{\rm esc}^{\rm MF}$ in the mean field limit. It is clear that in the plateau region $t_{\rm esc}^{\rm MB}$ is substantially different that the predicted mean field value.

The main point to take away from these comparisons is that when $N|U|/J$ or w

increases, the difference between $t_{\rm esc}^{\rm MF}$ and $t_{\rm esc}^{\rm MB}$ increases exponentially. Thus, we can quantitatively show the parameter regimes in which the DNLS fails to predict the correct escape time for MQT, and to what extent. It is especially remarkable to note that a weakly interacting system cannot be modeled accurately with mean field theory if the number of particles, N, is sufficiently large and the filling factor is sufficiently small. For example, for a very weakly interacting system with $U = -0.015J$ and $N = 20$, we have a value of $NU/J = -0.3$; in this case, mean field theory will under predict the escape time by over 10 percent. The disparity between the two methods is shown in Fig. 7.4(f), where in the plateau region we plot the percent difference in $t_{\rm esc}^{\rm MF}$ and $t_{\rm esc}^{\rm MB}$ over the average.

Systematic error in $t_{\rm esc}^{\rm MB}$ results from the Schmidt truncation used in TEBD [90], χ, the truncation in the on-site Hilbert space dimension, d, and the time resolution at which we write out data, δt. The hardest many-body measures to converge, such as the block entropy, at $\chi = 25$ have an error smaller than 10^{-3} for $N = 40$, and have been checked up through $\chi = 55$; due to very small interaction strengths much lower χ is required than usual in TEBD. A thorough discussion of convergence with respect to χ is presented in Appendix A.

Error bars in Fig. 7.4(d) are due solely to δt; there is additional error from our Suzuki-Trotter expansion, contributing an error of $O(\delta t^6)$ per time step, which is always smaller than our χ-induced error. For up to $N = 20$ we have not truncated d, but for larger N up to 60, we truncated to $d = 12$. A lower truncation results in decreased $t_{\rm esc}^{\rm MB}$, e.g. by 10% for $d = 5$, $NU/J = -0.1$, and $N = 10$, even though $\max(\langle \hat{n} \rangle) < 1$, since more weight is given to spread-out Fock states. Our use of TEBD for dynamics of the attractive BHH is the first, to our knowledge, and much higher d is required than in repulsive BHH simulations, since attractive interactions increase number fluctuations in high density regions. The BHH also has a number of sources of systematic error, the most important of which is virtual fluctuations to the second band; however, since we compare single-band DNLS to single-band BHH this does not effect our comparison.

7.4 Analyzing Real Time Dynamics With Quantum Measures

TEBD is a powerful tool that provides one with a wide array of quantum measures with which to study many-body systems. In this section we aim to give a brief overview of several useful quantum measures which will subsequently allow us to gain a better understanding of MQT.

In addition to the average particle number, real time dynamics can be observed from the number variance and the localized von Neumann entropy. The number variance characterizes the deviations of the average particle number away from the classical Poissonian limit, defined to be

$$\eta \equiv \langle (\Delta n)^2 \rangle \equiv \langle \hat{n}^2 \rangle - \langle \hat{n} \rangle^2. \tag{7.6}$$

The number variance is typically greatest on sites with large average number. Therefore, in our simulations with bright solitons, typically the number variance behaves similarly to the average on-site particle number. In Fig. 7.5, we plot the average on-site number alongside the number variance during MQT for a system of $N = 6$, $U = -0.066$, $J = 1$, and $w = 2$.

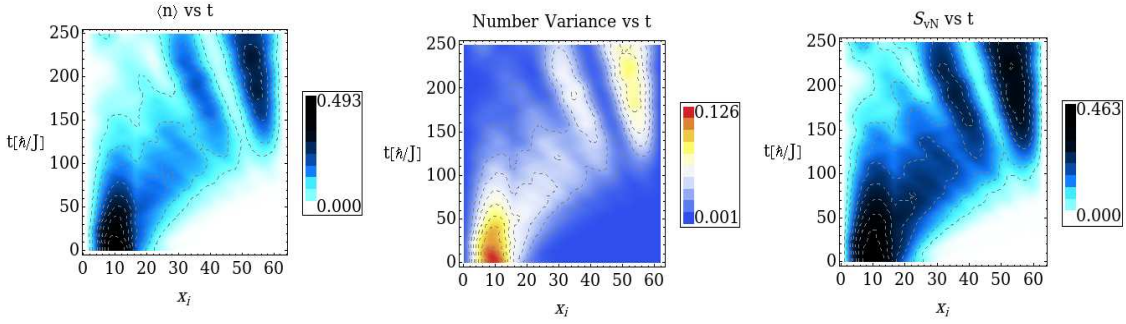

Figure 7.5: *Quantum Measures: Average Particle Number, Number Variance, and von Neumann Entropy.* The real time dynamics revealed by plotting the average particle number (left) are similar in character to the number variance (middle), and the localized von Neumann entropy (right), which assume their largest values when the average number of particles is large.

The localized von Neumann entropy, $S_{\mathrm{vN,k}}$, discussed previously in Eq. (5.6), is

another on-site observable useful for observing real time dynamics. $S_{\mathrm{vN,k}}$ quantifies the amount of information which is lost at a single site k, and can be used to classify deviations of the system away from the mean field limit. Since mean field calculations neglect any spatial entanglement in the system, the localized von Neumann entropy, calculated with TEBD, can show the regions during time-evolution where the mean field simulations will deviate most from the TEBD simulations. Naturally, the local von Neumann entropy is greatest in the regions where there are large collections of particles, as shown in Fig. 7.5, since many-body interactions play a strong role in those areas of the system.

To characterize the quantum nature of MQT, in Fig. 7.6(b), for the same system, we plot the fluctuations in the number of particles behind the barrier, defined as

$$f_l = \frac{\langle N_l^2 \rangle - \langle N_l \rangle^2}{\langle N_l \rangle}, \tag{7.7}$$

where N_l is the number of particles to the left of site l. This choice is indicative of the fact that number fluctuations will mainly reside at the barrier boundary. As shown in Fig. 7.6(b) fluctuations in the number of particles behind the barrier tend to increase over time, as more particles tunnel out of the well. Once MQT commences, f_l in time increases with $|U|$ because number densities just outside the barrier have more of an influence to "pull" additional particles through the barrier, and vice versa.

The quantum depletion $D \equiv 1 - N_0/N_{\mathrm{avg}}$, which in the low temperature limit describes quantum fluctuations due to particle-particle interactions in the system, is another useful quantum measure. As discussed in Section 5.1, quantum depletion is the proportion of particles that are not in the condensed mode; in TEBD we calculate the depletion via

$$D \equiv 1 - \left(\sum_{m=2}^{L} \lambda_m \right) \Big/ \left(\sum_{m=1}^{L} \lambda_m \right), \tag{7.8}$$

where $\{\lambda_m\}$ are the eigenvalues of the single particle density matrix, $\langle \hat{b}_i^\dagger \hat{b}_j \rangle$. During the time-evolution of the system, quantum depletion increases to values usually on

the order of ten percent or less, as shown in Fig. 7.6(c), but becomes large with strong interactions. When quantum depletion is higher than a few percent, we are working in a regime where DNLS simulations will tend to deviate from BHH simulations.

Of particular interest to MQT is the von Neumann block entropy characterizing entanglement between the remaining particles and the escaped particles, $S_l \equiv -\mathrm{Tr}(\hat{\rho}_l \log \hat{\rho}_l)$, where $\hat{\rho}_l$ is the reduced density matrix for the well plus barrier. In the language of TEBD we calculate the block entropy via,

$$S_l = -\sum_{a}^{\chi} \lambda_a^{[l]} \log_d(\lambda_a^{[l]}). \tag{7.9}$$

When plotted versus time for the tunneling bright soliton, S_l at the outside edge of the barrier increases to a maximum value as shown in Fig. 7.6(d), and then decreases as particles tunnel out of the well. The block entropy is maximal at the time when the system is in its most uniform probability distribution and is closely related to the slope of the average number fluctuations, df_l/dt, as we will investigate in the next section.

In addition, we can plot the localized von Neumann entropy at a given site, as shown in Fig. 7.6(e). At the site were the soliton peak is located, $S_{\mathrm{vN,mid}}$, the localized von Neumann entropy is very reminiscent of the average on-site number. Finally, as another quantum measure, we plot the average local impurity in Fig. 7.6(f), previously discussed in Eq. (5.7), which quantifies the amount of multiparticle entanglement in the system, in the sense that it calculates the bipartite entanglement between each site and every other site in the system. During the time-evolution of the system, the average local impurity usually does not change very significantly.

Additionally, we can plot the single-particle density matrix (SPDM), as shown in Fig. 7.7, and examine how off-diagonal long-range order, previously discussed in Section 1.2, changes during MQT. Similar to $g^{(2)}$, the SPDM should be symmetric with respect to the diagonal. Off-diagonal long-range order is a generalized measure of macroscopic quantum coherence in the system, and can be seen where there are

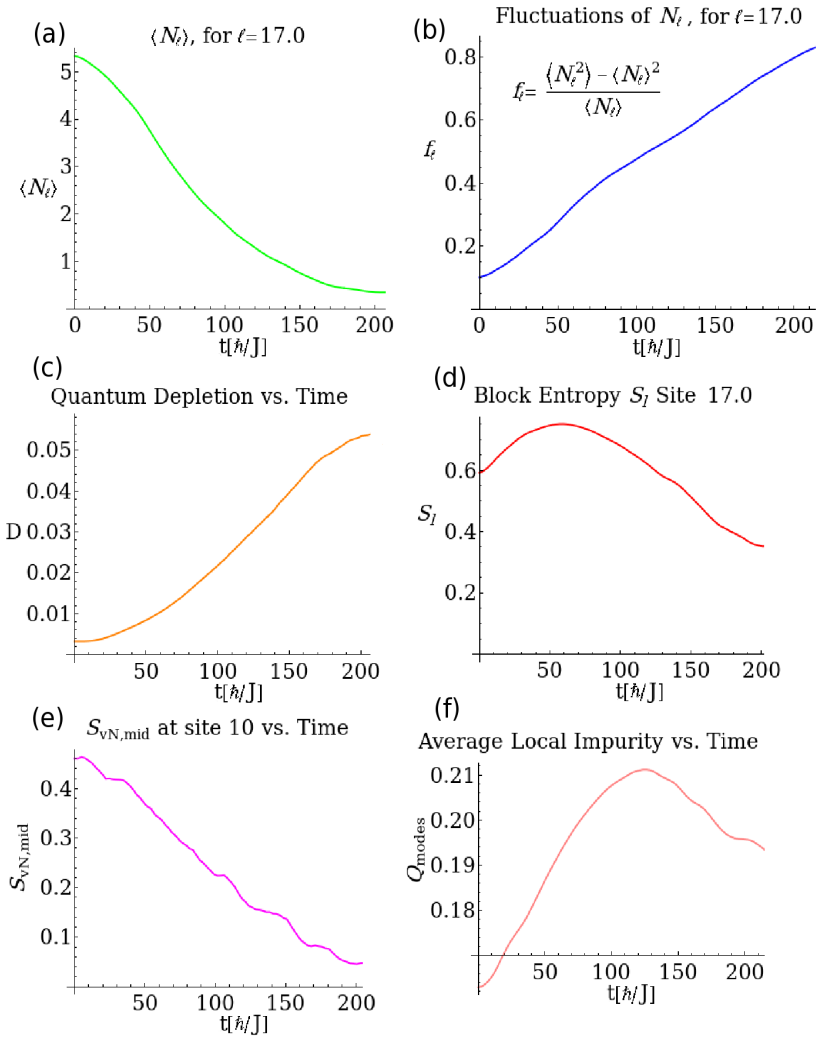

Figure 7.6: *Quantum Measures and Observables.* (a) The average number of particles to the left of the barrier is a smooth decaying function from which the escape time can be calculated. The fluctuations in the number of particles behind the barrier (b) and the quantum depletion (c) increase over time. The block entropy (d) peaks when the soliton is the most spread out over the system. The localized von Neumann entropy at the peak of the soliton (e) follows a similar trend as the average particle number. The average local impurity (f) changes only slightly. This example is for $N = 6$, $U = -0.066$, $J = 1$, and $w = 2$.

large[2] off-diagonal components of the SPDM.

Another quantum measure, useful for determining how the barrier alters nonlocal

[2]Dark spots in Fig. 7.7.

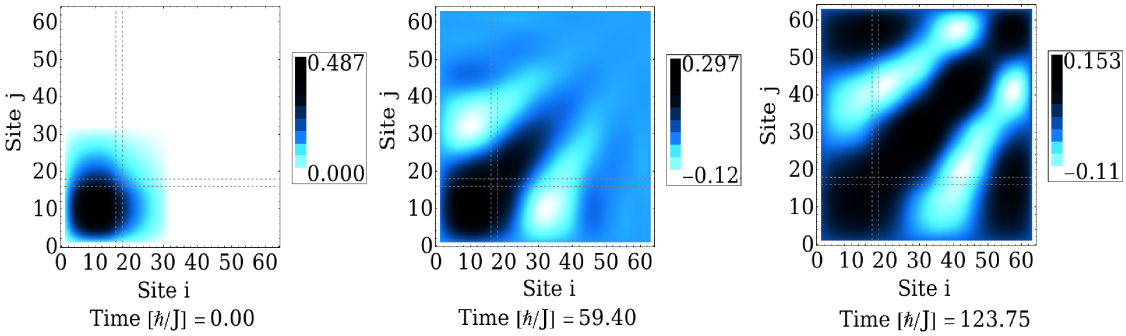

Figure 7.7: *The Single-Particle Density Matrix.* Time evolution of the single-particle density matrix shows how off-diagonal long-range order develops during MQT. Dashed lines indicate the position of the barrier. This example shows the single-particle density matrix at three different time slices for $N = 6$, $U = -0.066$, $J = 1$, and $w = 2$.

correlations in the system, is the density-density correlation function,

$$g^{(2)}(n_i, n_j) = \langle n_i n_j \rangle - \langle n_i \rangle \langle n_j \rangle, \tag{7.10}$$

where n_i (n_j) is the particle number at the i^{th} (j^{th}) site. The $g^{(2)}$ correlation is the expectation value of simultaneously measuring particles at sites i and j. It can be used in experiments as another signature of our many-body findings, as $g^{(2)}$ is extractable from noise measurements [96] and is zero in mean field theory. As customary, we subtract off the large diagonal matrix elements of $g^{(2)}$ to view the underlying off-diagonal structure. $g^{(2)}$ should always be symmetric with respect to the diagonal, since there is no preference to the labeling of i and j. In Fig. 7.8(a)-(c) we show $g^{(2)}$ for $N = 40$, $NU/J = -0.015$, and $w = 2$, dividing up the system to observe correlations between the three physical regions: trapped, under the barrier, and escaped. We initially observe near-zero correlations everywhere except near the soliton peak. At $t_{\text{esc}}^{\text{MB}}$, $g^{(2)}$ shows many negatively-correlated regions ($g^{(2)} < 0$) which are broken up by the potential barrier. In Fig. 7.8(d) for a large N comparison of $N = 20$ we also show rapidly growing quantum depletion for a large interacting system with $U = 0.025$, $J = 1$ and $w = 2$. This growth in D emphasizes the many-body nature of the escape

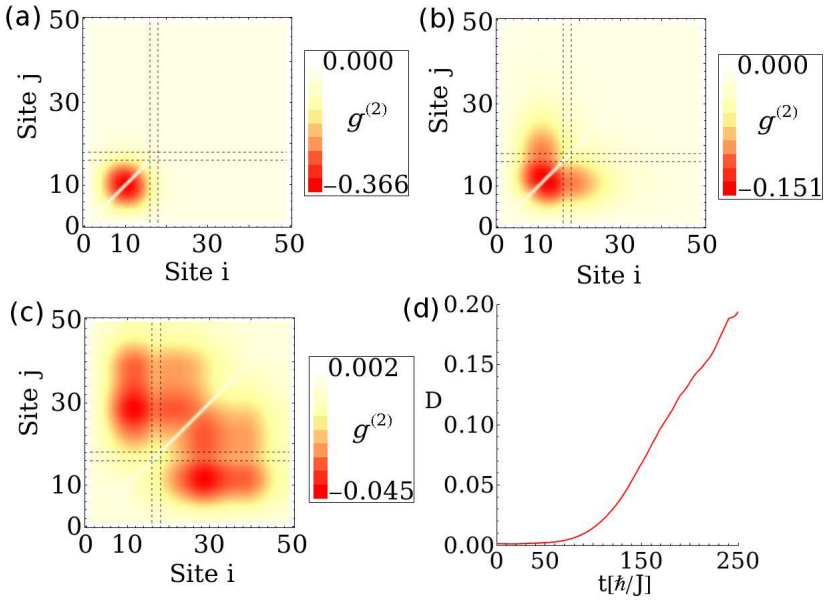

Figure 7.8: *Time-dependence of Density-density Correlations.* (a)-(c) $g^{(2)}$ shows correlations between trapped and escaped particles. The barrier, indicated by dashed lines, breaks up negatively-correlated regions (red); shown are time slices at $t = 0, 62, 125$. (d) Quantum depletion also grows rapidly.

process.

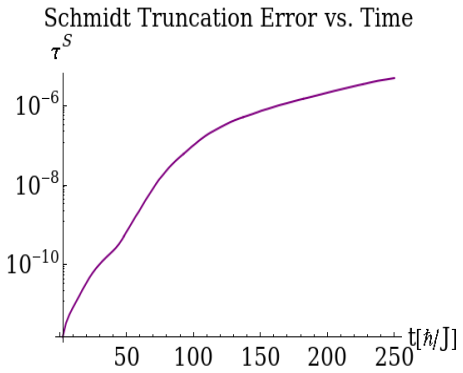

Figure 7.9: *Schmidt Truncation Error.* For $\chi = 55$, the Schmidt truncation error remains below a very acceptable order of 10^{-6} for the duration of the tunneling process. The relevant parameters for this plot are: $N = 6$, $U = -0.066$, $J = 1$, and $w = 2$.

When using BHH simulations, it is important to be aware that each individual quantum observable has its own distinct dependence on χ. All of the plots in this section were performed with a large value of $\chi = 55$, however, usually only a mini-

mum of $\chi = 15$ is required. A detailed analysis of the convergence of each quantum observable with χ is performed in Appendix A. For the convergence of BHH simulations it is also important to be aware of the Schmidt truncation error, which, for the simulations discussed in this section, is plotted in Fig. 7.9, and is discussed in additional detail in Appendix A.

7.5 Dependence of Quantum Measures On Interaction Strength

Plotting the dependence of several quantum observables versus the interaction strength reveals several important results. In Fig. 7.10(a) we plot the average number at the peak of the soliton. There are points in time when the number density exhibits steep exponential decay, and others during which it is nearly constant, similar to the density bursts found by Dekel *et al.* [74]; thus their predictions are correct even in the many-body regime. The first burst is independent of U. The initial flat horizontal region, at $t \simeq 25$, originates from initially left moving particles that are reflected off the leftmost infinite boundary and return back to the barrier. All subsequent deviations from exponential decay appear to be dependent on U.

In the escape time, $t_{\rm esc}^{\rm MB}$, we find exponential scaling dominates for stronger interactions, as shown in Fig. 7.10(d). The dependence is exponential for two reasons: the many-body wavefunction tends to have large number fluctuations at the soliton peak, keeping particles away from the barrier; and the averaged density creates an effective potential which increases the effective barrier size, as in mean field theory. Escape times depend exponentially on barrier area even in JWKB.

To characterize the quantum nature of MQT, in Fig. 7.10(b) we plot the fluctuations in the number of particles behind the barrier, f_l, where l is taken at the outer edge of the barrier. Once MQT commences, the maximum value of f_l in time increases with $|U|$ because number densities just outside the barrier have more influence to "pull" additional particles through the barrier, and vice versa. For example, fitting an s-shaped curve $f_l = a/[b + c\exp(-kt)]$ to Fig. 7.10(b), with a, b, c, k fit

parameters, we find $\max(f_l) = a/(b+c) = x|U| + y$. For early times, less than $t = 50$ in Fig. 7.10(b), f_l increases faster for smaller values of $|U|$ because the initial soliton is wider, but interactions take over shortly thereafter.

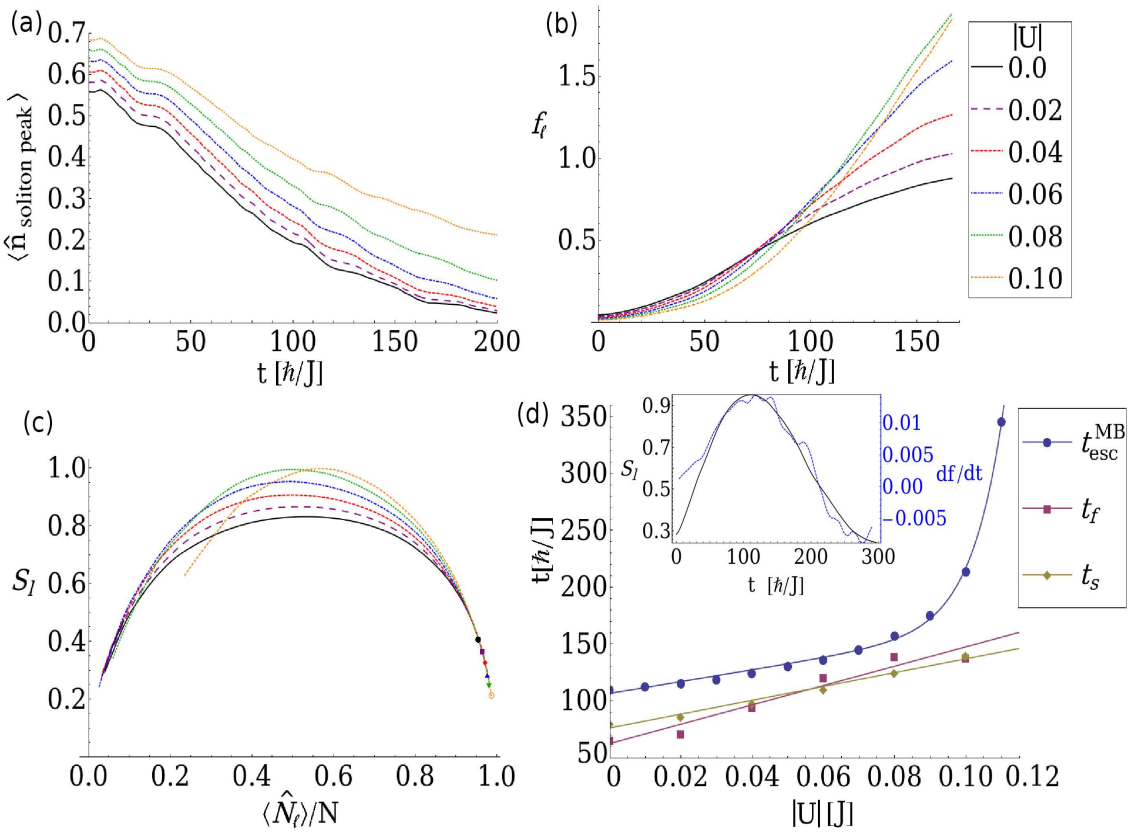

Figure 7.10: *Quantum Measures Vs. Interaction Strength* (a) Average number at the peak of the soliton shows bursts of particles [74]. (b) Fluctuations in the number of trapped particles increases with $|U|$. (c) Universal curve for the entropy of entanglement vs. the average number of trapped particles. (d) Exponential vs. linear increase in escape vs. many body times as a function of interactions. (Inset) Block entropy and df_l/dt closely follow each other, here for $|U| = 0.06$. The key applies to panels (a)-(c) and all plots treat $N = 6$.

Song *et al.* [97] have shown that in 1D conformal systems for which there is a conserved quantity, such as particle number, the variance of the fluctuations in that quantity between two subsystems A, B scales with the von Neumann entanglement entropy between A, B. Of particular interest to MQT is the von Neumann block entropy characterizing entanglement between the remaining particles and the escaped particles, S_l. The key features of S_l are illustrated in a universal curve in Fig. 7.10(c):

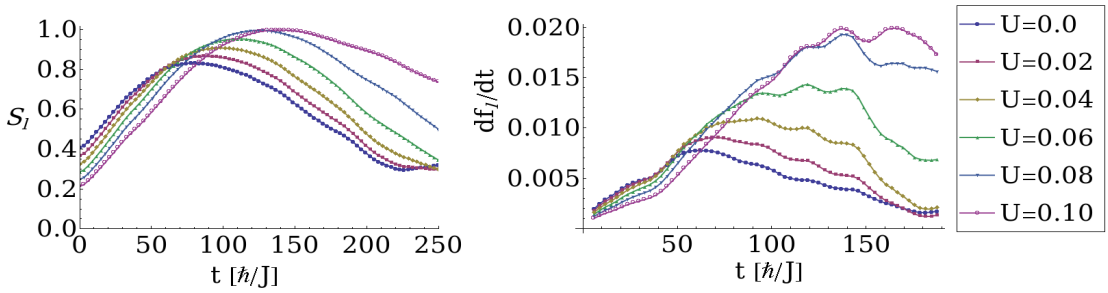

Figure 7.11: *Block entropy and the slope of number fluctuations* The block entropy S_l (left) and the slope of the number fluctuations behind the barrier df_l/dt(right) are plotted vs. time. The Block entropy and df_l/dt closely follow each other but do not scale precisely due to density bursts. All plots treat $N = 6$.

on the lower right side tunneling has not yet commenced; S_l maximizes part way through the tunneling process in the center of the curve; and S_l then decreases again to the left as the particles finish tunneling out. We cannot follow N_l/N all the way to zero in every case due to reflections off the far boundary. As MQT commences, particles tunnel out from behind the barrier, and the curves, which indicate different values of U, begin to split apart. The splitting of the curves begins around $\langle N_l \rangle/N = .95$, a value which can be used to characterize the onset of MQT. Note the starting point of each curve, which is indicated by a marker, is different because the tail of the initial bright soliton extends into the barrier depending on the value of U.

Defining t_s as the time at which S_l is maximized and t_f as the time at which the slope of the number fluctuations, df_l/dt, is maximized, we find t_s and t_f both increase linearly with U, in a dynamical extension of the static predictions of Ref. [97], as shown in Fig. 7.10(d). This behavior is in contrast to $t_{\rm esc}^{\rm MB}$ which increases exponentially with $|U|$. Moreover, S_l and df_l/dt follow the same general trends in time, as shown in the inset of Fig. 7.10(d). The two do not scale precisely, as df_l/dt is distorted by the density bursts illustrated in Fig. 7.10(a). In Fig. 7.11 we plot, for the same values as in Fig. 7.10(d), S_l and df_l/dt versus time to show the qualitative relationship between the two for various interaction strengths.

Chapter 8

CONCLUSION

We have presented a study of the quantum tunneling dynamics of many-body entangled bright solitons composed of ultracold bosonic gases in one-dimensional optical lattices. Bright solitons in cold atom systems have been realized for a wide range of experiments [26, 27, 51] and are the central focus of many promising applications such as atom lasers, soliton interferometers, and precision measurements. Past studies of bright solitons in BECs have leaned on mean field approaches, starting from the Gross-Pitaevskii equation or the DNLS, however, these methods are only valid if quantum fluctuations in the system are negligible. It is known that solitons in BECs are critically susceptible to quantum fluctuations, for example, recent studies have shown that quantum fluctuations restrict the lifetime of dark solitons by causing them to fill in [76, 77].

In this thesis we have presented, to our knowledge, the first exact quantum many-body simulations of bright solitons in BECs via time-evolving block decimation. Specifically, we have applied the method to the BHH to study the macroscopic quantum tunneling of bright solitons in BECs. We have predicted the escape time for a bright soliton, that is, the time in which the average number of atoms remaining behind the barrier drops to 1/e of its initial value. Using both BHH and DNLS simulations, we have modeled how the interaction strength, U, the number of particles N, and the barrier dimensions affect the escape time.

We found strong deviations from mean field predictions, and quantitatively demonstrated the parameter regimes in which the DNLS fails to predict the correct escape time for MQT, and to what extent. Generally, the DNLS grossly under predicts t_{esc} when $N|U|/J$ is sufficiently large, even for $N = 40$. With a well width of 16 lattice sites, we showed the mean field limit is only relevant for 70 or more

particles, when the filling $\nu \gg 1$. This is an important step in defining boundaries and benchmarks by which one can judge the legitimacy of applying mean field theory to these systems.

Clearly, for strongly interacting systems, quantum fluctuations will substantially alter the dynamics of macroscopic quantum tunneling, rendering mean field theory inadequate. However, as we have shown, it is especially remarkable that a weakly interacting system with a low filling factor cannot be modeled accurately with mean field theory if the number of particles is sufficiently large. For example, for a very weakly interacting system with $U = -0.015J$ and $N = 20$, we have a value of $NU/J = 0.3$; in this case, mean field theory will under predict the escape time by over 10 percent. When the ratio NU/J increases, the difference between the calculated escape time for mean field, $t_{\rm esc}^{\rm MF}$, and the BHH, $t_{\rm esc}^{\rm MB}$, increases exponentially in the plateau region of $N = 20$ to 40 particles.

In addition, we have demonstrated several clear-cut advantages in adopting a full quantum many-body treatment. TEBD has allowed us to characterize the quantum dynamics of MQT with a full set of quantum observables that are unaccessible to mean field approaches. Such observables can be used to deepen our understanding, and provide new interpretations of the many-body character of MQT. Several notable findings came out of this analysis. The average number of particles at the site of the soliton peak, shows time intervals when the number density exhibits steep exponential decay, and others during which the number density is nearly constant, a behavior similar to the density bursts found in reference [74]. Furthermore, by plotting the block entropy versus the average number of particles behind the barrier, we discovered a universal curve which can be used to characterize the onset of MQT.

The escape time was shown to increase exponentially with interactions while block entropy and the slope of number fluctuations maximized at a time which scaled linearly; entropy generally followed closely the slope of number fluctuations, suggesting a dynamical extension of the static concepts of Song *et al.* [97]. This suggests that many body effects in macroscopic quantum tunneling can be observed via num-

ber fluctuations. We found that once MQT commences, the maximum value of the fluctuations in the number of particles to the left of the barrier, f_l, increases as a function of U. This is because number densities just outside the barrier have more influence to "pull" additional particles through the barrier, and vice versa.

Finally, using density-density correlation functions $g^{(2)}$ we have been able to view how a potential barrier alters nonlocal correlations during MQT. It can be used in experiments as another signature of our many-body findings, as $g^{(2)}$ is extractable from noise measurements [96] and is zero in mean field theory. Our study provides several other experimental signatures via the average particle number, number fluctuations, and the increased escape time.

8.1 Outlook and Open Questions

There are many possible future directions for this work and ways to improve on this study. It would be interesting to apply instanton methods to this problem, which would provide a useful comparison to the mean field and TEBD simulations. Instanton methods may be able to capture other many-body features that the DNLS does not, and could perhaps yield different predictions of the escape time than the DNLS. Instanton calculations could therefore be used in conjunction with TEBD, to more clearly distinguish between the semiclassical and quantum many-body aspects of MQT. Improvements could be made to the TEBD code so as to include absorbing boundary conditions, which would allow one to examine a broader range of parameters without restricting one's view to a time frame determined by reflections, which occur off of the system boundaries.

In addition, it would also be worthwhile to investigate finite temperature effects with TEBD. The inclusion of both quantum and thermal fluctuations into the TEBD code would allow the simulations to more closely resemble actual experiments, enabling one to make direct comparisons between experiment and theory. In addition, it may be fruitful to examine the role of finite size effects on MQT in BECs. In this

thesis we have focused on rather large systems, but it would be interesting to examine how many-body solitons behave when restricted to only a few lattice sites. The spatial granularity imposed on a system by the optical lattice geometry could alter the escape time of bright solitons from behind a potential barrier. Also, one could perform the study presented here using non-rectangular potential barriers, such as smoothly varying or trapezoidal type geometries.

Finally, other characteristic aspects of bright solitons could modeled with TEBD, for example, one could study how quantum fluctuations affect the dynamics of collisions of two bright solitons. Experimental applications, such as soliton interferometry could be modeled using TEBD. Using periodic optical lattices, one could examine the quantum many-body aspects of gap solitons in BECs.

REFERENCES

[1] Interview of L. Rosenfeld by C. Weiner at Copenhagen. Niels Bohr Library and Archives, American Institute of Physics, College Park, MD USA, September 3, 1986. http://www.aip.org/history/ohilist/4848.html.

[2] Y. F. Li, T. Kaneko, and R. Hatakeyama. Formation of quantum dots in single stranded dna-wrapped single-walled carbon nanotubes. *Applied Physics Letters*, 96(2):023104, 2010.

[3] Sidney Coleman. Fate of the false vacuum: Semiclassical theory. *Phys. Rev. D*, 15(10):2929–2936, May 1977.

[4] Curtis G. Callan and Sidney Coleman. Fate of the false vacuum. ii. first quantum corrections. *Phys. Rev. D*, 16(6):1762–1768, Sep 1977.

[5] D. M. Ostrovsky, G. W. Carter, and E. V. Shuryak. Forced tunneling and turning state explosion in pure yang-mills theory. *Phys. Rev. D*, 66(3):036004, Aug 2002.

[6] Dmitry Solenov and Dmitry Mozyrsky. Metastable states and macroscopic quantum tunneling in a cold-atom josephson ring. *Phys. Rev. Lett.*, 104(15):150405, Apr 2010.

[7] Masahito Ueda and Anthony J. Leggett. Macroscopic quantum tunneling of a bose-einstein condensate with attractive interaction. *Phys. Rev. Lett.*, 80(8):1576–1579, Feb 1998.

[8] I Zapata, F. Sols, and A. J. Leggett. Josephson effect between trapped Bose-Einstein condensates. *Phys. Rev. A*, 57:R28–R31, 1998.

[9] Michael Albiez, Rudolf Gati, Jonas Folling, Stefan Hunsmann, Matteo Cristiani, and Markus K. Oberthaler. Direct observation of tunneling and nonlinear self-trapping in a single bosonic Josephson junction. *Phys. Rev. Lett.*, 95:010402, 2005.

[10] L. D. Carr, D. Dounas-Frazer, and M. Garcia-March. Quantum entangled dark solitons formed by ultracold atoms in optical lattices. *Euro. Phys. Lett.*, 90(1):10005, 2010.

[11] Alexej I. Streltsov, Ofir E. Alon, and Lorenz S. Cederbaum. Scattering of an attractive Bose-einstein condensate from a barrier: Formation of quantum superposition states. *Phys. Rev. A*, 80:043616, 2009.

[12] M. H. Anderson, J. R. Ensher, M. R. Matthews, C. E. Wieman, and E. A. Cornell. Observation of bose-einstein condensation in a dilute atomic vapor. *Science*, 269(5221):198–201, 1995.

[13] K. B. Davis, M. O. Mewes, M. R. Andrews, N. J. van Druten, D. S. Durfee, D. M. Kurn, and W. Ketterle. Bose-einstein condensation in a gas of sodium atoms. *Phys. Rev. Lett.*, 75(22):3969–3973, Nov 1995.

[14] C. C. Bradley, C. A. Sackett, J. J. Tollett, and R. G. Hulet. Evidence of bose-einstein condensation in an atomic gas with attractive interactions. *Phys. Rev. Lett.*, 75(9):1687–1690, Aug 1995.

[15] C. C. Bradley, C. A. Sackett, and R. G. Hulet. Bose-einstein condensation of lithium: Observation of limited condensate number. *Phys. Rev. Lett.*, 78(6):985–989, Feb 1997.

[16] Steven Chu. Nobel lecture: The manipulation of neutral particles. *Rev. Mod. Phys.*, 70(3):685–706, Jul 1998.

[17] Claude N. Cohen-Tannoudji. Nobel lecture: Manipulating atoms with photons. *Rev. Mod. Phys.*, 70(3):707–719, Jul 1998.

[18] William D. Phillips. Nobel lecture: Laser cooling and trapping of neutral atoms. *Rev. Mod. Phys.*, 70(3):721–741, Jul 1998.

[19] L.Landau and E.Lifschitz. *Statistical Physics, Part 2*. Pergamon Press, Oxford, UK, 1980.

[20] S.Stringari L.Pitaevskii. *Bose-Einstein Condensation*. Clarendon Press, Oxford, 2003.

[21] A.J.Legget. *Quantum Liquids: Bose Condensation and Cooper Pairing in Condensed-Matter Systems*. Oxford University Press, USA, 2006.

[22] L.Landau and E.Lifschitz. *Quantum Mechanics, Nonrelativistic Theory*. Pergamon Press, Oxford, UK, 1977.

[23] A.A.Abrikosov, L.P.Gorkov, and I.E.Dzyaloshinski. *Methods of Quantum Field Theory in Statistical Physics*. Dover, 1975.

[24] Alexander L. Fetter. Theory of a dilute low-temperature trapped bose condensate. 1998.

[25] S. E. Pollack, D. Dries, M. Junker, Y. P. Chen, T. A. Corcovilos, and R. G. Hulet. Extreme tunability of interactions in a ^7li bose-einstein condensate. *Phys. Rev. Lett.*, 102(9):090402, Mar 2009.

[26] L. Khaykovich, F. Schreck, G. Ferrari, T. Bourdel, J. Cubizolles, L. D. Carr, Y. Castin1, and C. Salomon. Formation of a matter-wave bright soliton. *Science*, 296(5571):1290–1293, May 2002.

[27] Kevin E. Strecker, Guthrie B. Partridge, Andrew G. Truscott, and Randall G. Hulet. Formation and propagation of matter-wave soliton trains. *Nature*, 417(2):150–153, May 2002.

[28] J. M. Vogels, C. C. Tsai, R. S. Freeland, S. J. J. M. F. Kokkelmans, B. J. Verhaar, and D. J. Heinzen. Prediction of feshbach resonances in collisions of ultracold rubidium atoms. *Phys. Rev. A*, 56(2):R1067–R1070, Aug 1997.

[29] S. Inouye, M. R. Andrews, J. Stenger, H.-J. Miesner, D. M. Stamper-Kurn, and W. Ketterle. Observation of feshbach resonances in a bose-einstein condensate. *Nature*, 392(151), 1998.

[30] Eric Cornell. Very cold indeed: The nanokelvin physics of bose-einstein condensation. *J. Res. Natl. Inst. Stand. Technol.*, 101(4), July 1996.

[31] Franco Dalfovo, Stefano Giorgini, Lev P. Pitaevskii, and Sandro Stringari. Theory of bose-einstein condensation in trapped gases. *Rev. Mod. Phys.*, 71(3):463–512, Apr 1999.

[32] L. D. Carr, Charles W. Clark, and W. P. Reinhardt. Stationary solutions of the one-dimensional nonlinear schrödinger equation. i. case of repulsive nonlinearity. *Phys. Rev. A*, 62(6):063610, Nov 2000.

[33] L. D. Carr, Charles W. Clark, and W. P. Reinhardt. Stationary solutions of the one-dimensional nonlinear schrödinger equation. ii. case of attractive nonlinearity. *Phys. Rev. A*, 62(6):063611, Nov 2000.

[34] Maciej Lewenstein, Anna Sanpera, Veronica Ahufinger, Bogdan Damski, Aditi Sen De, and Ujjwal Sen. Ultracold atomic gases in optical lattices: mimicking condensed matter physics and beyond. *Advances in Physics*, 56(2):135, 2006.

[35] A.J. Daley. *Manipulation and Simulation of Cold Atoms in Optical Lattices*. PhD thesis, University of Innsbruck, 2005.

[36] I.Bloch. Ultracold quantum gases in optical lattices. *Nature*, 1(14):23–30, Oct 2005.

[37] Markus Greiner, Immanuel Bloch, Olaf Mandel, Theodor W. Hänsch, and Tilman Esslinger. Exploring phase coherence in a 2d lattice of bose-einstein condensates. *Phys. Rev. Lett.*, 87(16):160405, Oct 2001.

[38] J. Hecker Denschlag, J. E. Simsarian, H. Häffner, C. McKenzie, A. Browaeys, D. Cho, K. Helmerson, S. L. Rolston, and W. D. Phillips. A bose-einstein condensate in an optical lattice. *Journal of Physics B: Atomic, Molecular and Optical Physics*, 35(14):3095, 2002.

[39] F. Ferlaino, P. Maddaloni, S. Burger, F. S. Cataliotti, C. Fort, M. Modugno, and M. Inguscio. Dynamics of a Bose-Einstein condensate at finite temperature in an atom-optical coherence filter. *Phys. Rev. A*, 66(1), Jul 2002.

[40] O. Morsch, J. H. Müller, M. Cristiani, D. Ciampini, and E. Arimondo. Bloch oscillations and mean-field effects of bose-einstein condensates in 1d optical lattices. *Phys. Rev. Lett.*, 87(14):140402, Sep 2001.

[41] B. P. Anderson and M. A. Kasevich. Macroscopic quantum interference from atomic tunnel arrays. *Science*, 282(5394):1686–1689, 1998.

[42] O. Morsch, M. Cristiani, J. H. Müller, D. Ciampini, and E. Arimondo. Free expansion of a bose-einstein condensate in a one-dimensional optical lattice. *Phys. Rev. A*, 66(2):021601, Aug 2002.

[43] A. M. Rey. *Ultracold bosonic atoms in optical lattices*. PhD thesis, University of Maryland, 2004.

[44] Ana Maria Rey, Guido Pupillo, Charles W. Clark, and Carl J. Williams. Ultracold atoms confined in an optical lattice plus parabolic potential: A closed-form approach. *Phys. Rev. A*, 72(3):033616, Sep 2005.

[45] J. S. Russell. Report on waves. *Fourteenth meeting of the British Association for the Advancement of Science*, 1844.

[46] N. J. Zabusky and M. D. Kruskal. Interaction of "solitons" in a collisionless plasma and the recurrence of initial states. *Phys. Rev. Lett.*, 15(6):240–243, Aug 1965.

[47] Norman J. Zabusky. Solitons and bound states of the time-independent schrödinger equation. *Phys. Rev.*, 168(1):124–128, Apr 1968.

[48] A. Hasegawa. *Optical Solitons in Fibers*. Springer-Verlag, New York, NY, 1990.

[49] P. G. Drazin and R. S. Johnson. *Solitons: an Introduction*. Cambridge Univ. Press, Cambridge, 1989.

[50] G. P. Agrawal. *Nonlinear Fiber Optics 2nd ed.* Academic Press, San Diego, 1995.

[51] Simon L. Cornish, Sarah T. Thompson, and Carl E. Wieman. Formation of bright matter-wave solitons during the collapse of attractive bose-einstein condensates. *Phys. Rev. Lett.*, 96(17):170401, May 2006.

[52] J. Denschlag, J. E. Simsarian, D. L. Feder, Charles W. Clark, L. A. Collins, J. Cubizolles, L. Deng, E. W. Hagley, K. Helmerson, W. P. Reinhardt, S. L. Rolston, B. I. Schneider, and W. D. Phillips. Generating solitons by phase engineering of a bose-einstein condensate. *Science*, 287(5450):97–101, January 2000.

[53] S. Burger, K. Bongs, S. Dettmer, W. Ertmer, K. Sengstock, A. Sanpera, G. V. Shlyapnikov, and M. Lewenstein. Dark solitons in bose-einstein condensates. *Phys. Rev. Lett.*, 83(25):5198–5201, Dec 1999.

[54] B. Eiermann, Th. Anker, M. Albiez, M. Taglieber, P. Treutlein, K.-P. Marzlin, and M. K. Oberthaler. Bright bose-einstein gap solitons of atoms with repulsive interaction. *Phys. Rev. Lett.*, 92(23):230401, Jun 2004.

[55] Christoph Becker, Simon Stellmer, Parvis Soltan-Panhi, Soren Dorscher, Mathis Baumert, Eva-Maria Richter, Jochen Kronjager, Kai Bongs, and Klaus Sengstock. Oscillations and interactions of dark and dark-bright solitons in bose-einstein condensates. *Nature*, 4:496–501, June 2008.

[56] Jacek Dziarmaga and Krzysztof Sacha. Bose-einstein-condensate heating by atomic losses. *Phys. Rev. A*, 68(4):043607, Oct 2003.

[57] G. Wentzel. Eine Verallgemeinerung der Quantenbedingungen für die Zwecke der Wellenmechanik. *Zeitschrift fur Physik*, 38:518–529, June 1926.

[58] H. A. Kramers. Wellenmechanik und halbzahlige Quantisierung. *Zeitschrift fur Physik*, 39:828–840, October 1926.

[59] L. Brillouin. La mecanique ondulatoire de schrodinger; une methode generale de resolution par approximations sucessives. *Comptes Rendus*, 183, Jul 1926.

[60] Harold Jeffreys. On certain approximate solutions of linear differential equations of the second order. *London Math. Soc., Proc.*, 23:428–436, 1923.

[61] Eugen Merzbacher. *Quantum Mechanics*. Wiley, 3rd edition, 1998.

[62] L. D. Carr, M. J. Holland, and B. A. Malomed. Macroscopic quantum tunnelling of bose-einstein condensates in a finite potential well. *J. Phys. B: At. Mol. Opt. Phys.*, 38(3217):3217–3231, Sept 2005.

[63] B. Sakita. *Quantum Theory of Many-Variable Systems and Fields*. World Scientific, Singapore, 1985.

[64] Ippei Danshita and Anatoli Polkovnikov. Accurate numerical verification of the instanton method for macroscopic quantum tunneling: Dynamics of phase slips. *Phys. Rev. B*, 82(9):094304, Sep 2010.

[65] M.R. Andrews, C.G. Townsend, H. J. Miesner, D.S. Durfee, D.M. Kurn, and W. Ketterle. Observation of interference between two bose condensates. *Science*, 275:637–641, Jan 1997.

[66] B. P. Anderson and M. A. Kasevich. Macroscopic quantum interference from atomic tunnel arrays. *Science*, 282:1686–1689, Nov 1998.

[67] Immanuel Bloch, Theodor W. Hänsch, and Tilman Esslinger. Atom laser with a cw output coupler. *Phys. Rev. Lett.*, 82(15):3008–3011, Apr 1999.

[68] L. D. Carr and J. Brand. Pulsed atomic soliton laser. *Phys. Rev. A*, 70(3):033607, Sep 2004.

[69] M. R. Andrews, C. G. Townsend, H.-J. Miesner, D. S. Durfee, D. M. Kurn, and W. Ketterle. Observation of interference between two bose condensates. *Science*, 275(5300):637–641, 1997.

[70] G. Roati, E. de Mirandes, F. Ferlaino, H. Ott, G. Modugno, and M. Inguscio. Atom interferometry with trapped fermi gases. *Phys. Rev. Lett.*, 92(23):230402, Jun 2004.

[71] M. Fattori, C. D'Errico, G. Roati, M. Zaccanti, M. Jona-Lasinio, M. Modugno, M. Inguscio, and G. Modugno. Atom interferometry with a weakly interacting bose-einstein condensate. *Phys. Rev. Lett.*, 100(8):080405, Feb 2008.

[72] Wolfgang Ketterle. Experimental studies of bose-einstein condensation. *Physics Today*, 52(12):30–35, 1999.

[73] N. Veretenov, Yu. Rozhdestvenskya, N. Rosanov, V. Smirnov, and S. Fedorov. Interferometric precision measurements with bose-einstein condensate solitons formed by an optical lattice. *Eur. Phys. J. D*, 42:455–460, 2007.

[74] G. Dekel, V. Farberovich, V. Fleurov, and A. Soffer. Dynamics of macroscopic tunneling in elongated bose-einstein condensates. *Phys. Rev. A*, 81(6):063638, Jun 2010.

[75] W. H. Press, B. P. Flannery, S. A. Teukolsky, and W. T. Vetterling. *Numerical Recipes In C: The Art of Scientific Computing.* Cambridge University Press, Cambridge, 1988.

[76] R. V. Mishmash and L. D. Carr. Quantum entangled dark solitons formed by ultracold atoms in optical lattices. *Phys. Rev. Lett.*, 103(14):140403, Sep 2009.

[77] R. V. Mishmash, I. Danshita, Charles W. Clark, and L. D. Carr. Quantum many-body dynamics of dark solitons in optical lattices. *Phys. Rev. A*, 80(5):053612, Nov 2009.

[78] B. Jackson, N. P. Proukakis, and C. F. Barenghi. Dark-soliton dynamics in bose-einstein condensates at finite temperature. *Phys. Rev. A*, 75(5):051601, May 2007.

[79] S. Stellmer, C. Becker, P. Soltan-Panahi, E.-M. Richter, S. Dörscher, M. Baumert, J. Kronjäger, K. Bongs, and K. Sengstock. Collisions of dark solitons in elongated bose-einstein condensates. *Phys. Rev. Lett.*, 101(12):120406, Sep 2008.

[80] A. Weller, J. P. Ronzheimer, C. Gross, J. Esteve, M. K. Oberthaler, D. J. Frantzeskakis, G. Theocharis, and P. G. Kevrekidis. Experimental observation of oscillating and interacting matter wave dark solitons. *Phys. Rev. Lett.*, 101(13):130401, Sep 2008.

[81] Th. Busch and J. R. Anglin. Motion of dark solitons in trapped bose-einstein condensates. *Phys. Rev. Lett.*, 84(11):2298–2301, Mar 2000.

[82] S. P. Cockburn, H. E. Nistazakis, T. P. Horikis, P. G. Kevrekidis, N. P. Proukakis, and D. J. Frantzeskakis. Matter-wave dark solitons: Stochastic versus analytical results. *Phys. Rev. Lett.*, 104(17):174101, Apr 2010.

[83] Michael A. Nielsen and Isaac L. Chuang. *Quantum Computation and Quantum Information*. Cambridge University Press, 1 edition, Oct 2000.

[84] A. Einstein, B. Podolsky, and N. Rosen. Can quantum-mechanical description of physical reality be considered complete? *Phys. Rev.*, 47(10):777–780, May 1935.

[85] J. S. Bell. On the einstein-podolsky-rosen paradox. *Physics*, 1:195–200, 1964.

[86] Stuart J. Freedman and John F. Clauser. Experimental test of local hidden-variable theories. *Phys. Rev. Lett.*, 28(14):938–941, Apr 1972.

[87] E. Schrodinger. Discussion of probability relations between separated systems. *Mathematical Proceedings of the Cambridge Philosophical Society*, 31(4):555–563, 1935.

[88] M. Lewenstein and B. Malomed. Entanglement generation by collisions of quantum solitons in the born approximation. *New J. Phys.*, 11(113014), November 2009.

[89] Guifré Vidal. Efficient classical simulation of slightly entangled quantum computations. *Phys. Rev. Lett.*, 91(14):147902, Oct 2003.

[90] Guifrie Vidal. Efficient simulation of one-dimensional quantum many-body systems. *Phys. Rev. Lett.*, 93(4):040502, Jul 2004.

[91] Erhard Schmidt. Zur theorie der linearen und nichtlinearen integralgleichungen. i teil. entwicklung willkurlichen funktionen nach system vorgeschriebener. *Mathematische Annalen*, 63:433–476, 1907.

[92] M. B. Hastings. An area law for one-dimensional quantum systems. *Journal of Statistical Mechanics: Theory and Experiment*, 2007(08):P08024, 2007.

[93] Etienne Forest and Ronald D. Ruth. Fourth-order symplectic integration. *Physica D: Nonlinear Phenomena*, 43(1):105–117, 1990.

[94] T. Wenger T. Kinoshita and D. S. Weiss. A quantum newton's cradle. *Nature*, 440:900–903, 2006.

[95] D. Muth, B. Schmidt, and M. Fleischhauer. Fermionization dynamics of a strongly interacting 1D Bose gas after an interaction quench. *New J. Phys.*, 12:083065, 2010.

[96] Ehud Altman, Eugene Demler, and Mikhail D. Lukin. Probing many-body states of ultracold atoms via noise correlations. *Phys. Rev. A*, 70(1):013603, Jul 2004.

[97] H. Francis Song, Stephan Rachel, and Karyn Le Hur. General relation between entanglement and fluctuations in one dimension. *Phys. Rev. B*, 82(1):012405, Jul 2010.

APPENDIX A

CONVERGENCE STUDIES

This appendix concerns the sources of error with the TEBD method. We will examine two primary aspects of error which ultimately determine the accuracy of a given TEBD simulation. First, we will consider the crucial effect of χ, the number of basis states saved for every two-site operation in TEBD, on convergence. Each physical observable, such as the quantum depletion or the average local impurity, may behave differently with χ, so we will examine each individually. In the second section of this appendix we will discuss the other errors inherent to the algorithm, for example the accumulated errors accrued during real and imaginary time evolution from Suzuki-Trotter step, and due to the truncation of the Hilbert space to a local dimension d.

A.1 The Effects of χ on Convergence

As previously stated, the TEBD algorithm rests on the premise that an exponentially large Hilbert space for a many-body system can be accurately represented after a truncation, such that only the χ largest singular values are retained. When we perform a SVD on a matrix $\tilde{\Theta}$, of dimensions $(\chi d) \times (\chi d)$, and choose keep only the χ largest singular values $\tilde{\lambda}_i$, we effectively discard the smallest $\chi(d-1)$ eigenvalues. Generally for lowly entangled systems, the number of eigenvalues required to yield a good representation of the many-body state is small, thus allowing for highly-efficient computation times. It is in this sense that we say that TEBD is best suited for the study of lowly entangled systems. The surest way to test for convergence is to make a relative comparison between simulations at a given value of χ versus simulations with larger values of χ, for each output observable. Such an analysis will allow one to determine the minimum value of χ required to adequately perform simulations to

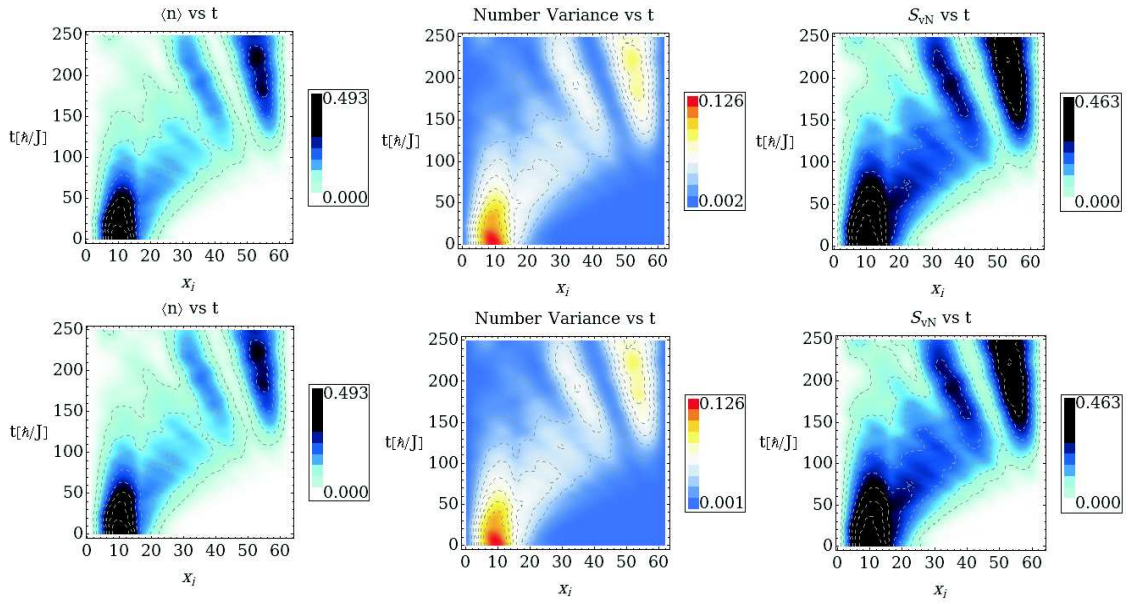

Figure A.1: *Dynamics At Different* χ. No noticeable differences are detected in the average number, the number variance, and the von Neumann entropy between simulations with $\chi = 15$ (Top) and $\chi = 55$ (Bottom). The simulations are for a system with $L = 63$, $N = 6$, $NU/J = 0.25$, $w = 2$.

a desired level of accuracy. Generally, for our purposes, converged physically sensible results are obtained for χ as low as 25. At $\chi = 15$ the overall real time dynamics are unchanged in comparison to simulations with $\chi = 55$. This is shown in Figure A.1 where no noticeable difference can be seen in the average number, the number variance, and the von Neumann entropy.

To demonstrate convergence we plot the time dependence of each quantum measure and observable with respect to χ. In Fig. A.2 we plot the hardest many-body measures to converge, quantum depletion and the block entropy, for $\chi = 15, 25, 35, 45, 55$. At $\chi = 25$ have an error smaller than 10^{-4} for $N = 6$, and were checked up through $\chi = 55$; due to small U and effective system size, much lower χ is required than usual in TEBD. Additionally we plot the relative error in each observable for each value of χ in comparison to that for $\chi = 55$. At $\chi = 15$ the observable with the largest discrepancy is the quantum depletion, which can reach errors of order 10^{-3}. In general, the convergence of the quantum depletion will be lower than other

observables because it is calculated using the nonlocal observables $\left\langle \hat{b}_j^\dagger \hat{b}_i \right\rangle$ which are elements of the single-particle density matrix. However, for $\chi = 25$, the relative error drops to an order of 10^{-5}. In general, faster convergences with respect to χ occurs for observables that are more local. For example, the relative error for observables like the average local impurity is small.

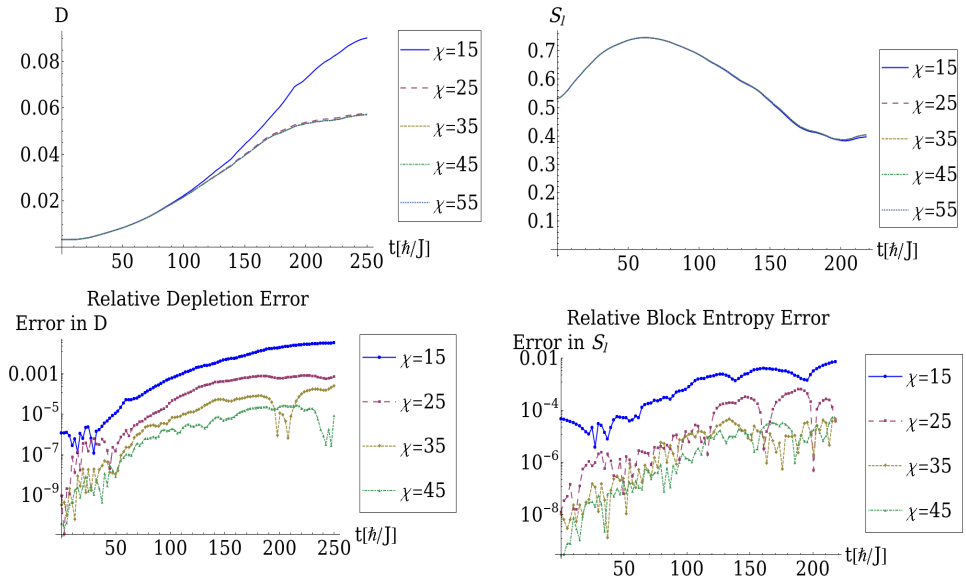

Figure A.2: *Quantum Depletion and Block Entropy vs.* χ. (top): With larger values of χ the quantum depletion and the block entropy, are converged during all times in the simulations. (bottom): We plot the relative error in each observable, for each value of χ in relation to the previous simulation. This example shows a system of $L = 63$, $N = 6$, $NU/J = 0.25$, $w = 2$.

Another useful check on the algorithm is to examine the ability of the code to maintain conserved quantities inherent to the Hamiltonian of interest, such as the total average number and the total average energy. We have checked the relative error in these quantities at the final time step in comparison to at the initial step. The errors in the total average number is $\leq 1\%$ and decreases with increasing values of χ. The error in the total average energy similarly is $\leq 1\%$, however does not generally correlate strongly with the value of χ.

The local Schmidt truncation error τ_l^S arises form the discarded eigenvalues of the reduced density matrix. The *total Schmidt truncation error*, τ^S, is the total sum

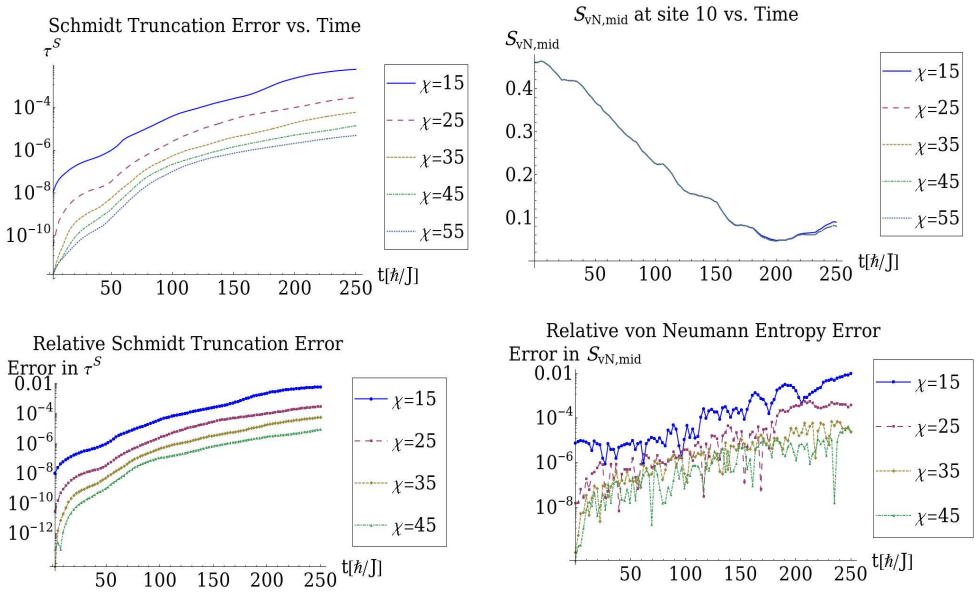

Figure A.3: *Schmidt error and von Neumann entropy vs.* χ (left): With larger values of χ the Schmidt error is reduced in the simulations. (right): The von Neumann entropy is converged to 10^{-5} for $\chi = 25$. These are simulations for a system with $L = 63$, $N = 6$, $NU/J = 0.25$, $w = 2$.

of the τ_l^S errors for each site l. Recall that the Schmidt coefficients are normalized in the fashion, $\sum_{\alpha_l}^{\chi_S} \left(\lambda_{\alpha_l}^{[l+1]}\right)^2 = 1$. Using this relation we define the total Schmidt truncation error as,

$$\tau_l^S \equiv 1 - \sum_{\alpha_l}^{\chi} \left(\lambda_{\alpha_l}^{[l+1]}\right)^2. \tag{A.1}$$

The total Schmidt truncation error is critically dependent on χ, but in principle, for sufficiently large χ the total Schmidt error will tend to zero. In this sense, we describe TEBD as a quasi-exact method. Over the course of the time-evolution of a system, the total Schmidt truncation errors accumulate, thus it is important to bear in mind the length of any given simulation. The total Schmidt truncation error plotted versus time and χ is shown in Fig. A.3. We plot the relative Schmidt truncation error for for different values of χ in Fig. A.3.

When we use the Suzuki-Trotter expansion to numerically approximate the exponential time propagator, for a fourth-order Suzuki-Trotter method we incur errors of order $O(\delta t^6)$ per time step. After 5000 time steps, of length $\delta t = 0.1\hbar/J$, the

error accumulates to $O(10^{-3})$. We have tested the validity of using a time step of $\delta t = 0.1\hbar/J$ by verifying the simulations remain unchanged for $\delta t = 0.01\hbar/J$, and $\delta t = 0.005\hbar/J$.